Investigating Process-Microstructure-Property Relationships and Degradation in Semi-Crystalline Thermoplastic Composites through Multi-Faceted Experiments and Machine Learning Techniques

Mathew Wynn

A dissertation

submitted in partial fulfillment of the

requirements for the degree of

Doctor of Philosophy

University of Washington

2024

Reading Committee:

Navid Zobeiry, Chair

Eleftheria Roumeli

Marco Salviato

Program Authorized to Offer Degree:

Materials Science & Engineering

University of Washington

Abstract

Investigating Process-Microstructure-Property Relationships and Degradation in Semi-Crystalline Thermoplastic Composites through Multi-Faceted Experiments and Machine Learning Techniques

Mathew Wynn

Chair of the Supervisory Committee:

Navid Zobeiry

Department of Materials Science & Engineering

Changes in processing affect the morphology of semicrystalline thermoplastic composites, and, in turn, their performance, including tensile strength, toughness, and high strain-rate sensitive properties such as impact performance. Additionally, thermal degradation or partial oxidation of thermoplastic composites may severely affect the crystal growth process and mechanical properties as well as chemical resistance to common solvents. This also influences the recyclability of the material, as well as available repair-time or time to bring large-scale parts to melt. However, the process-microstructure-property relationships and degradation of thermoplastic composites are not well understood, limiting their applications in industries such as aerospace and defense. In this study, a novel framework of multi-faceted experiments and

Machine Learning (ML) Techniques is developed to address limitations of traditional approaches and accelerate the establishment of these relationships in thermoplastic composites.

The evolution of crystalline morphology in carbon fiber reinforced thermoplastic composites, such as reinforced PEEK, PEKK, and LM-PAEK, is studied in-situ using a polarized microscope equipped with a heating and cooling controlled stage, combined with probabilistic ML analysis using Gaussian Process Regression (GPR). First, ultra-thin films of low volume fraction composites are prepared and processed with various temperature cycles under the microscope. A classification ML model based on the Yolov3 algorithm is developed to determine size and growth rate statistics, while a segmentation model based on the U-Net algorithm is used to segment crystals that have impinged and do not have clear edges.

Next, the size and frequency of transcrystalline and spherulite regions are correlated to temperature history using a combination of traditional theory-based methods for fitting crystallization kinetics, as well as the GPR method. While spherulite growth rate is found to obey the established Lauritzen-Hoffman theory, transcrystalline growth deviates from the theory. This difference is investigated by deconvoluting the underlying mechanisms of growth and impinging of spherulites on transcrystalline regions around fibers.

Degradation effects are investigated using a combination of polarizing light microscopy (PLM), Fourier transform infrared (FTIR) spectroscopy, x-ray scattering, and ML techniques including Principal Component Analysis (PCA) and GPR. While PLM is used for in-situ investigation of the effect of degradation on crystallization, FTIR is used for in-vitro analysis of degradation effects on chemical signature of the material. X-ray scattering is employed to measure nanoscale crystalline structures. ML methods are utilized to investigate and map the underlying correlations in high-dimensional, sparse, and noisy experimental data. Results show a

significant correlation between melt temperature and processing environment with the resulting lamellar thickness and overall degree of crystallinity.

PEEK film, single ply, and 2-ply PEKK prepreg coupons are tensile tested to failure in a Linkam MFS350 at room temperature and 160°C. Additionally, the effect of strain rate on tensile strength is evaluated. Results are used to investigate the effect of polymer degradation (induced by elevated melt temperature, processing in air, and repeated cycling) on tensile strength. The investigation reveals that an increase in strain rate leads to higher tensile strength, whereas undergoing cycles reduces the tensile strength of PEEK film. In the case of 1-ply prepreg, its tensile strength remains largely unaffected by various processing parameters, with the notable exception of test temperature. For 2-ply prepreg, the combined effects of cycling and environmental exposure are significant; specifically, subjecting the 2-ply prepreg to three cycles in an air environment results in a reduction of its tensile strength. The degree of crystallinity in 2-ply samples is characterized using WAXS and DSC and is found to not correlate with melt, cycles, or environment. The fractured surfaces are imaged using SEM. It is determined that the fiber interface may be affected by thermal degradation even when the degree of crystallinity is unaffected.

Laser-assisted automated fiber placement is employed to fabricate wedge peel coupons of thermoplastic composites with different processing parameters, including compaction force, roller head speed, and temperature. Using a combination of wedge peel testing to measure the peel force of prepreg tapes, digital and scanning electron microscopic imaging, image segmentation of fractured surfaces, and probabilistic surrogate machine learning fitting, the effect of processing parameters on mechanical performance and failure is examined. Wedge peel fracture surfaces are photographed and analyzed using Weka image segmentation to identify

regions of bonding and non-bonding. Scanning electron microscopy is used to study the failure mechanism. These results are then used to train surrogate probabilistic machine learning models to analyze the effect of processing parameters on wedge peel failure. It is observed that the bonding surface area increases with processing temperature, resulting in an increase in wedge peel force. However, increasing the compaction force results in greater variability of the bonding and peel force, while roller head speed has a negligible effect for the examined range. It was noted that wedge peel samples with increased variability tend to crack during testing, exhibiting partial resin and fiber pull-out. The combined image analysis, mechanical testing and machine learning approach successfully characterize the wedge peel behavior based on changes in automated fiber placement processing parameters.

A GPR framework was successfully applied to the degradation parameters and correlated with tensile strength. With additional data this framework could be used to achieve a deeper understanding of the mechanics behind thermoplastic degradation in composites.

Table of Contents

List of Figures

List of Tables

1 Introduction

1.1 Background

1.1.1 Thermoplastic Composites

Thermoplastic composites offer excellent mechanical properties including enhanced impact resistance compared to thermoset composites. This, in addition to the promise of shorter processing times and reprocessability, has led to a surge of applications for thermoplastic composites in recent years. Those fabricated with high-performance semi-crystalline thermoplastics such as PEEK (Polyetheretherketone), PEKK (Polyetherketoneketone) and LM-PAEK (Low melt Polyaryletherketone) are of particular interest in aerospace industry. The chemical structures of PEKK and PEEK are provided in Figure 1. Examples include PEEK composite used in the international space station mechanical arm, or brackets of commercial aircrafts.1,2 For such applications, thermoplastic composites are typically consolidated and processed using manufacturing techniques such as automated fiber placement (AFP) followed by autoclave consolidation or compression molding. In these processing methods, parameters such as melt temperature history, dwell time, fiber volume fraction as well as shear deformation history highly affect the crystallinity of the end-part.3–5 Without proper crystallization, these thermoplastics typically tend towards their amorphous properties offering much lower mechanical properties as well as little resistance to chemicals.

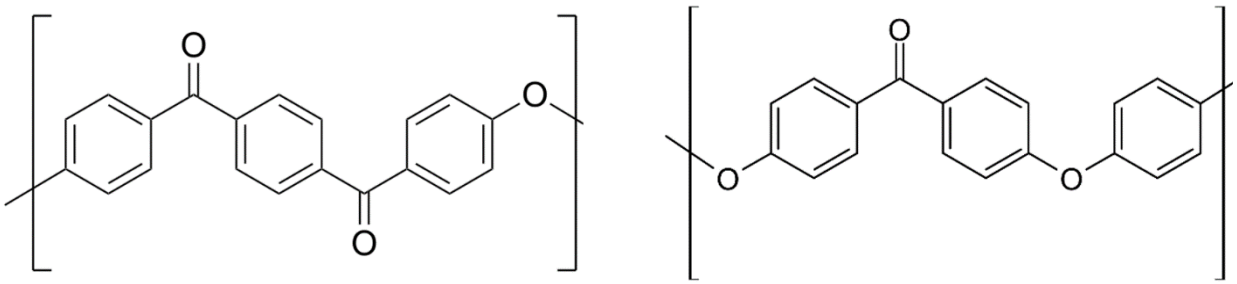

PEKK PEEK

Figure 1. Left: Chemical structure of PEKK. **Right:** Chemical structure of PEEK.

Semi-crystalline thermoplastics will degrade if they are held at or above their melting temperature for an extended period of time. This degradation is worsened by higher melt temperatures and the presence of oxygen. Degraded material has a higher glass transition temperature (T_g), lower crystallinity, and lower melting temperature.[6] This degradation in the thermoplastic matrix affects crystal formation and will change the morphology. These changes likely occur due to random molecular scission and subsequent cross-linking.[7] Specifically, bonds can occur within the polymer chain or between chains.[8] These changes to the polymer reduce recyclability and reworkability, as well as alter its mechanical and thermal properties.

Even with a similar degree of crystallinity, crystal types and crystalline morphology may affect the performance of composite parts.[9,10] The primary structure formed in PEEK is the spherulite with lamellae radiating from a center nucleus with amorphous polymer chains filling the spaces in between.[11] The lamellae are comprised of folded chains that align perpendicular to the growth front. The crystallization process is governed by nucleation and growth where after initial nuclei have formed in the supercooled melt, the crystal goes through the growth process. There have been many attempts in the literature to describe the crystallization growth kinetics.[12] One of the most common models is Lauritzen-Hoffman theory, where growth is governed by a competition between the rate of secondary nucleation and rate of diffusion.[13,14] During secondary

nucleation, nuclei are constantly formed onto the surface of a primary parent crystal. Here, primary nucleation is differentiated as the initial nucleation from melt, and secondary nucleation occurs from the surfaces of primary nuclei. However, molecular-level details of this process is not well understood.[15] On the other hand, diffusion is the transportation process of polymer segments and hence lateral growth along the crystallization front.[12,14,15]

When fibers are present, a second type of crystalline structure can form, known as transcrystallinity.[16] This occurs when crystal lamellae directly nucleate from the fibers and grow primarily perpendicular to them.[17] For high fiber volume fraction composites, transcrystallinity dominates the morphology, while in resin rich areas such as in gaps and overlaps created by AFP processing, spherulites dominate the microstructure due to lack of heterogeneous sites. At the boundary of these regions, the competition between nucleation and growth of these crystals determines the final morphology and hence material performance. Such morphology highly depends on the processing conditions including temperature history. For example, a sufficiently high melting temperature inhibits PEEK's tendency for self-nucleation by removing thermal history, which increases the likelihood to form transcrystallinity in PEEK composites.[18] PEEK also has a tendency for secondary crystallization.[19,20] This occurs when a lower melting temperature crystal structure forms on reheat, typically during annealing after initial crystallization.[21] The growth rate and dimensions of transcrystalline regions are typically similar to spherulites.[22]

Examples of transcrystallinity and spherulites are provided in Figure 2. In Figure 2(a), transcrystallinity is observed on both fibers. One transcrystalline region shows uniform growth perpendicular from the fiber, while the other is predominantly spherulitic in nature, representing an intermediate form. Over time, the spherulitic growths are likely to fill out and resemble the

uniform transcrystalline region shown in Figure 2(a). Circular spherulites of varying sizes are visible in both Figure 2(a) and (b). When spherulites grow and impinge upon each other, growth stops at that interface and the spherulite becomes non-circular. The crystals shown in Figure 2 were stopped mid-growth, and the black region between them represents amorphous polymer that is yet to be crystallized. Typically, for PEEK, the entire surface is covered with crystals unless quenched. In addition, the transcrystalline regions and spherulites shown in Figure 2 are not stacked. This was confirmed through real-time observation during the sample's cooldown.

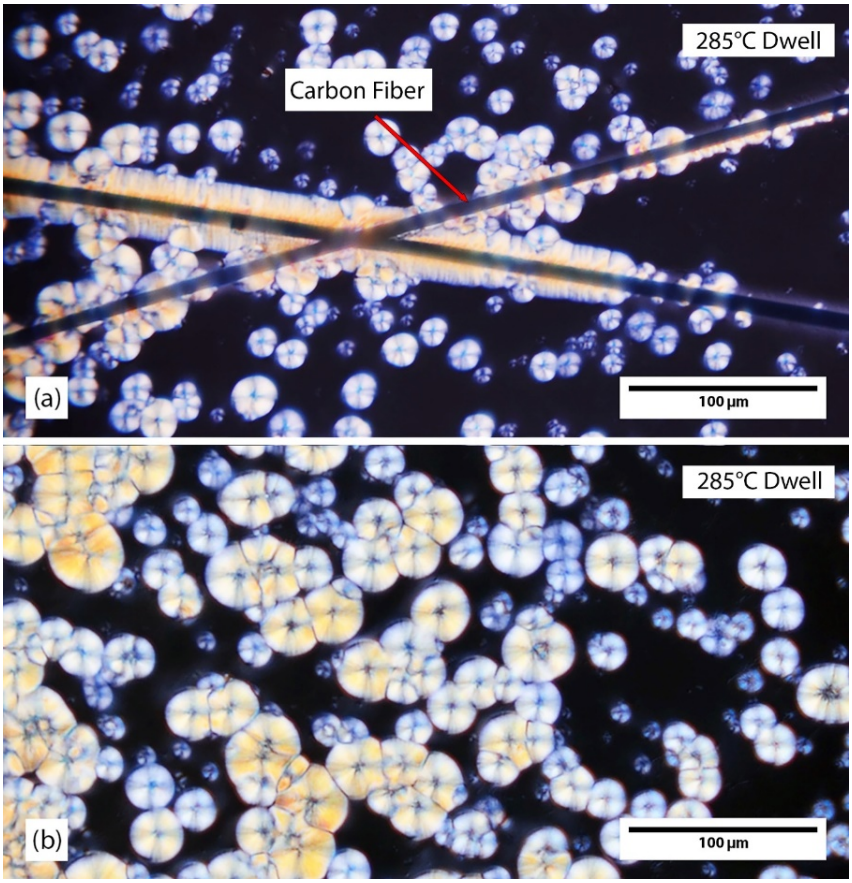

Figure 2. Examples of transcrystallinity and spherulites after a 285°C crystallizing dwell (a) shows a transcrystalline region growing from both fibers, with a spherulitic-type growth occurring on the fiber in the top right. Spherulites are observed in the surrounding material. (b) shows spherulites of varying sizes impinging onto each other and others isolated and circular.

1.1.2 Polarized Light Microscopy

To understand the effects of processing parameters and degradation on microstructure, characterization methods such as differential scanning calorimetry (DSC) , wide-angle x-ray scattering (WAXS), or nuclear magnetic resonance (NMR) can be utilized to measure the degree of crystallinity.[23–25] These methods, however, do not reveal types and gradients of microstructures within the material. For a direct characterization approach, polarized light microscopy (PLM) is often used.[5,11,26] The crystalline portion of the microstructure exhibits birefringence which allows for microstructure characterization through transmission PLM.[27] Regions that go to extinction in a crossed-polarized light are non-crystalline. These are either amorphous polymer, oxidized cross-linked polymer, or fibers. Other microscopic methods are possible, such as etching and scanning electron microscopy (SEM) or atomic force microscopy (AFM).[28,29] SEM is limited to the effectiveness of etchant and surface evaluations, while AFM provides an indirect perspective based on sample compliance with limited scanning area. In addition to difficulties with sample preparation, there also are challenges with data reduction and analysis. Specifically, fitting kinetics models for nucleation, growth, and melting of crystals using visual methods such as microscopy is not trivial. Due to testing and material variabilities, the data from these methods have a high degree of noise and is affected by measurement errors.

To evaluate crystal morphology using the PLM technique, samples thinner than 50μm are preferred. Otherwise crystalline structures may stack, which makes it difficult to distinguish crystal morphology.[30] Such thin samples can be prepared through cumbersome polishing. However, it is quite challenging to reach the required thicknesses while maintaining the original morphology due to heat generation affecting crystallinity, or broken fibers damaging the surface.[27] Alternatively, a microtome can be used, but shearing likely affects the crystals.[31]

1.1.3 Degradation

Thermal and oxidative degradation of polyaryletherketones above melt is well documented in the literature. Patel et al described the degradation mechanisms in detail.[32] Patel et al found PEEK was stable in inert environments up to 400°C for six hours; in air the glass transition temperature and crystallization were significantly affected. Degradation has been shown to cleave chains while forming crosslinks between aryl groups within the polymer chain.[7,33–35] Multiple experimental methods have been used to characterize PEEK degradation: dynamic mechanical analysis (DMA), mechanical testing, rheology, Fourier transform infrared (FTIR), ultraviolet visible spectrophotometry, thermogravimetric analysis, and gel permeation chromatography.[36–40] Another study reported the effect of crosslinking on increasing viscosity and found that air exposure during elevated temperature processing significantly affected compression molding processing of PEEK composites.[41]

Thermal degradation of PEEK has been shown to be a two-step process.[33,42,43] First, polymer chains are randomly broken at ether or carbonyl locations, which creates groups ending in phenols. These phenol-end groups are further cleaved through hydrogen abstraction producing phenol, which eventually volatilizes leaving a carbon char. Other volatile products include benzoquinone, dibenzofuran, and benzene. The creation of volatile products leads to micropores that can initiate cracks, but it has been shown that crystallinity as measured in DSC is affected before the formation of any volatiles as measured in thermogravimetric analysis.[37]

1.1.4 Mechanical Properties

Strength and failure of semi-crystalline thermoplastics are dependent on the size and uniformity of the crystal structures. Specifically, failure will shift from inter-crystalline cracking to spherulite boundary cracking to ductile or semi-brittle failure as size, temperature, and strain

rate change.[44] Inter-crystalline cracking is failure that travels radially from the spherulite nucleus to the spherulite edge, and spherulite boundary cracking is failure along spherulite edges. Examples of theses failures are shown in Figure 3. In general, as strain rate increases, failure shifts away from a ductile or semi-brittle failure, and as temperature increases failure tends toward ductile or semi-brittle failure. Additionally, larger spherulites are less resistant to the effects of strain rate and temperature.[44] The addition of fibers in thermoplastic composites further complicates this process. For example, Figure 3 also illustrates a crack traveling through transcrystallinity and then continuing along carbon fiber.

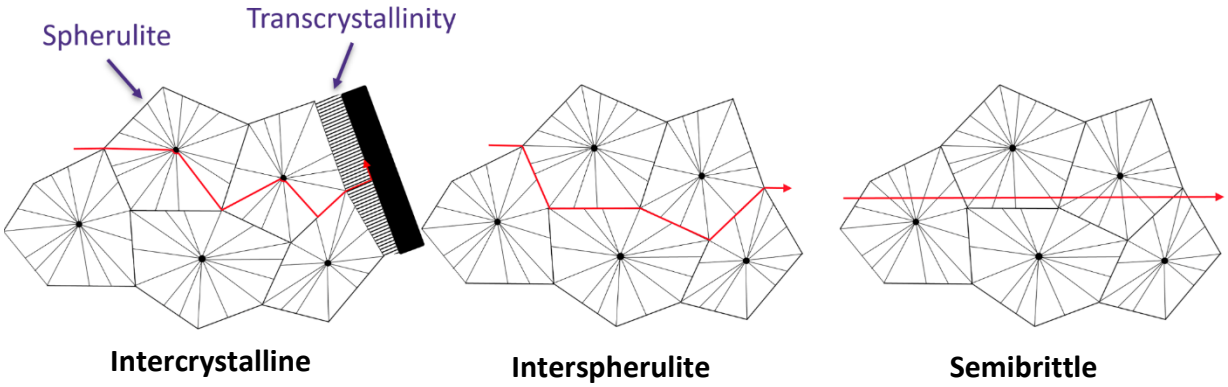

Figure 3. Failure mechanisms in spherulitic and transcrystalline microstructure.[44]

Chu and Shultz found that the failure mode and fracture toughness of PEEK was dependent on spherulite size.[45] Fracture toughness decreased with increased melting temperature, which coincides with increasing spherulite size. In lower molecular weight PEEK, failure was dominated by intra-spherulitic fracture – which Chu and Schultz termed nucleus pull-out. Higher molecular weight PEEK yielded inter-spherulitic fracture where the failure surface was drawn and fingerlike.[45]

As thermo-oxidative degradation occurs in thermoplastic composites, the polymer matrix loses its toughness. In one study, it was found that increasing melt temperature and the time

spent at these temperatures led to cracks forming at lower stresses in a 3-point bend test.[46] This occurrence was an initial crack and not total failure, which indicates brittle behavior over that of typical semi-crystalline thermoplastic composites. This degradation effect on crack formation was accelerated in the presence of oxygen. In another study, PEEK powder sandwiched between APC-2 composite (PEEK/CF) had flexural strength decreased as melt temperature increased from 400°C to 620°C. In this case, there was a decrease in strength and modulus, but the results showed significant variability meaning it is inconclusive. However, thermal degradation was observed to induce the formation of cracks and voids in the matrix. These stress concentrations will invariably reduce strength.[47] Flexural testing on thermally degraded CF/PEEK exhibited no substantial deterioration in bending under different heat treatment conditions. Bending strength remained stable except at 440°C for 10 minutes. In this case, the resistance to thermal degradation may be due to the bending failure being more significantly influenced by fiber reinforcement.[48]

In general, as degradation leads to the cross-linking of polymer chains, mobility will be decreased, and crystallization will be impeded. With reduced crystallinity due to degradation, most mechanical properties such as strength, modulus, and toughness will be negatively affected.

1.1.5 Fourier Transform Infrared Spectroscopy

Changes in the polymer due to degradation can be detected using Fourier transform infrared (FTIR) spectroscopy for both PEEK and PEKK. Typically, FTIR analysis such as this will be performed qualitatively by observing changes from a baseline spectrum.[8]

Pascual et al. used FTIR to analyze changes in functional groups after extended thermal degradation of PEEK samples.[8] Changes around 1650cm^{-1}, along with an intensity decrease at the phenyl band around 1300cm^{-1}, indicated changes near the benzophenone rings. New carbonyl

groups past 1700cm^{-1} mean that dibenzocyclopentanone structures formed, especially in the dark browned edges of the samples where oxidation was more severe. In these cases, the new chemical structures form due to intramolecular bonding, and the darkening is attributed to charring as the rings continue to close. Pascual et al. noted that degradation in the molten and solid states likely experiences different reaction mechanisms during thermal degradation. Changes at 1150 and 800cm^{-1} relate to impacts on diphenylether bonds and affect the intensity in the region between 1300 and 1150cm^{-1} Additionally, these changes impact the aromatic rings and are attributed to intermolecular cross-linking.

1.1.6 X-ray Scattering

Thermoplastics such as PEEK have a microstructure made up of crystalline structures arranged in a lamellar pattern. An illustration of this lamellar structure is shown in Figure 4. Polymer chains fold back and forth to build up these lamellae, which are typically 5-20nm thick and are surrounded by amorphous material.

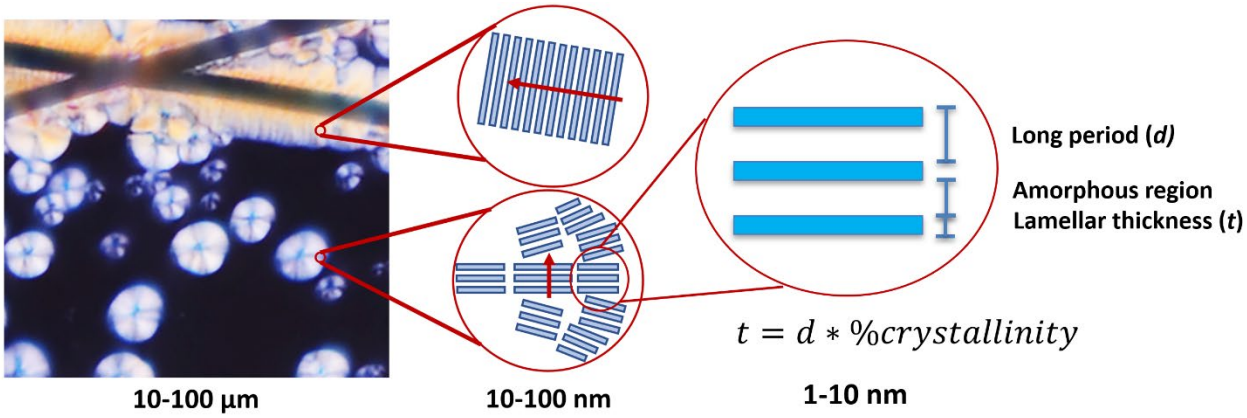

Figure 4. Lamellar structure that comprises spherulites and transcrystallinity.

Small-angle x-ray scattering (SAXS) is a technique used to measure the thickness of these lamellar structures, denoted as *t* in Figure 4.[49] In SAXS, monochromatic x-rays are passed through the sample, which elastically scatters the x-rays and creates a two-dimensional scattering

pattern (see Figure 5). By integrating a slice of this pattern, a one-dimensional scattering curve is generated, providing information on nanoscale structures. An example of a one-dimensional SAXS curve is shown in Figure 6. SAXS is typically performed at scattering angles in the range of 0.1-10°.

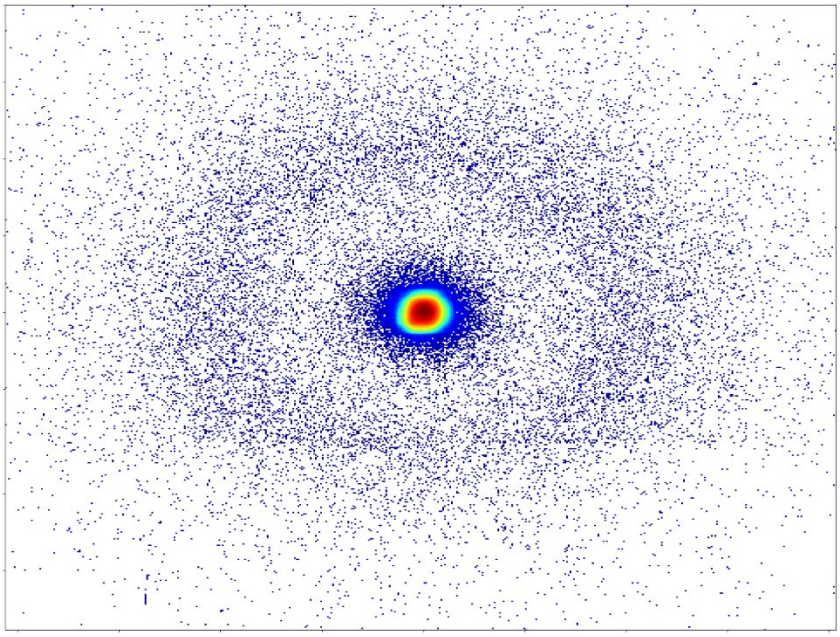

Figure 5. Example two-dimensional scattering pattern after SAXS.[50]

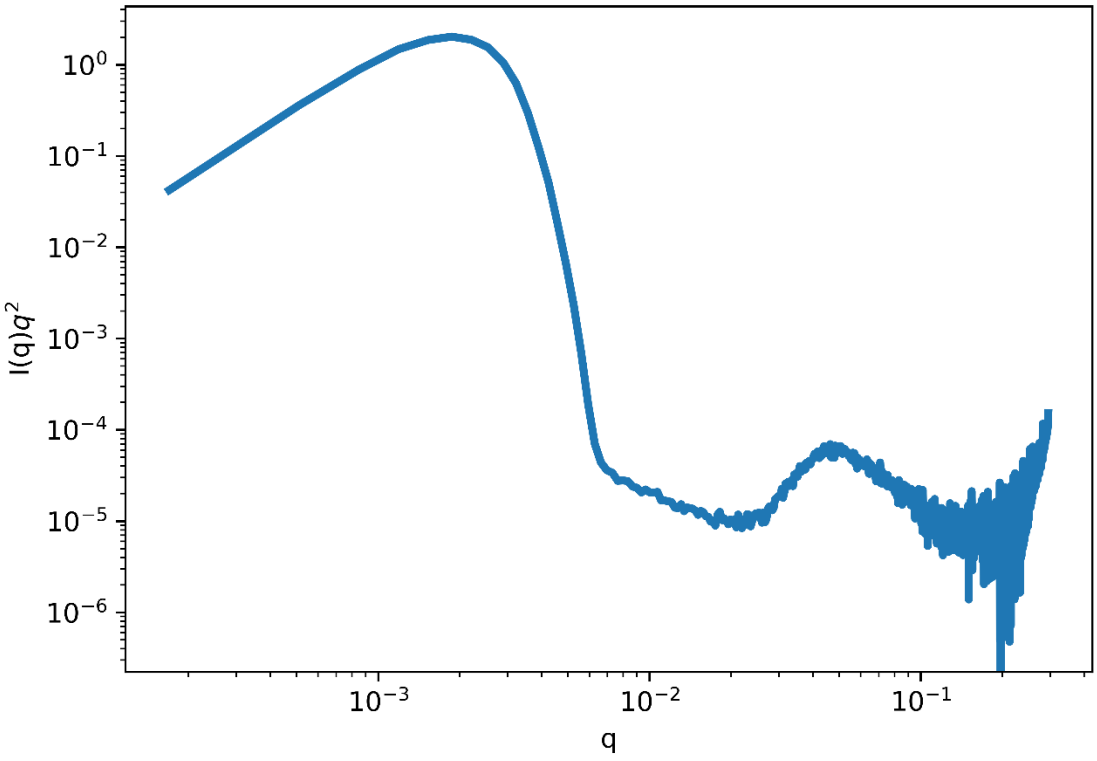

Figure 6. An example of a one-dimensional SAXS curve.

Another technique, wide-angle x-ray scattering (WAXS), can be used to gather information at the angstrom scale by performing scattering at wider angles, typically ranging from 10-55°. An example WAXS curve is provided in Figure 7. WAXS is used to identify Bragg peaks, and the area underneath the curves is related to the degree of crystallinity in the sample.[51,52] The area underneath the curves will be affected by the carbon fiber reinforcement. With unidirectional reinforcement, the fiber angle can be changed with respect to the incident beam to minimize the effect on measuring crystallinity. However, given the complexities involved in data reduction and morphology analysis of semicrystalline composites via SAXS/WAXS methodologies, the role of advanced analytics and statistical techniques becomes more pronounced.

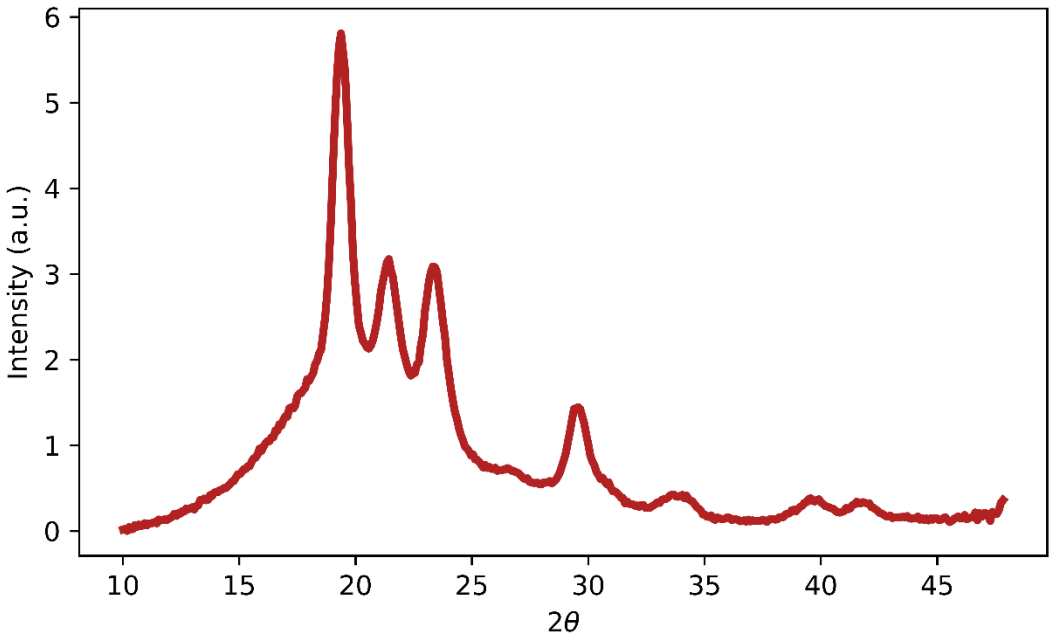

Figure 7. An example of a WAXS curve.

1.1.7 Automated Fiber Placement

Automated fiber placement (AFP) of thermoset composites has been widely used for a decade.[53] However, AFP of thermoplastic composites has not seen the same level of widespread use. Some of the challenges include the lack of tack, high processing temperature and pressure, and the intricacies of the autohesion process and crystallization kinetics, which predominantly influence the mechanical properties of the composite material. A notable form of AFP for thermoplastic composites is laser-assisted, where high-powered lasers are utilized to heat the material as it is laid down and compacted using a semi-compliant roller.[54] An example of a laser-assisted thermoplastic composites AFP is provided in Figure 8.

Figure 8. Example of a laser-assisted thermoplastic composite AFP.

The quality of an AFP lay-up is mainly determined by the degree of intimate contact and the degree of autohesion between plies.[55] Degree of intimate contact is a function of the melt viscosity of the thermoplastic polymer, time, and the compaction force from the roller head.[56–58] Pressure and temperature vary significantly over time at the nip point, which affects polymer flow and therefore the degree of intimate contact. The degree of autohesion involves movement and diffusion of thermoplastic polymer chains across the ply interface to bond, followed by crystallization during cool-down.[59–61] The combination of intimate contact and autohesion is typically used to calculate the degree of bonding.[55,62] A schematic illustrating degree of intimate contact and degree of autohesion is shown in Figure 9.

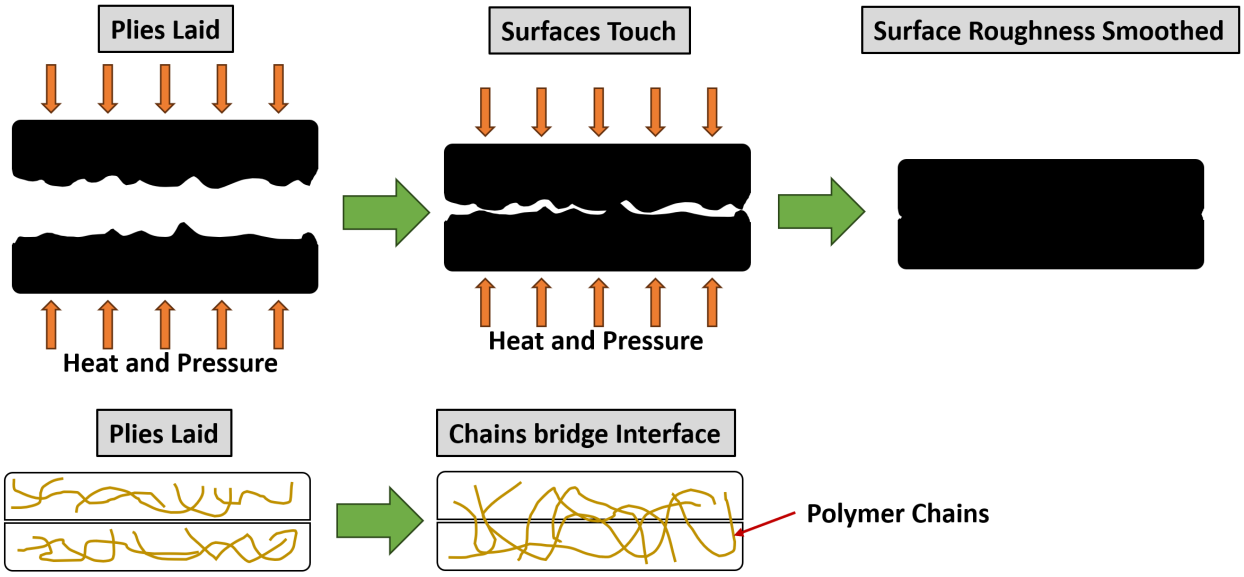

Figure 9. Schematic showing bonding between AFP layers **Top:** shows degree of intimate contact where heat and pressure smooths out the rough surfaces of each ply over time **Bottom**: shows degree of autohesion where with time the polymer chains on each side bridge across the interface.

1.1.8 Machine Learning for Process-Microstructure-Performance Analysis of Composites

In recent years, Machine Learning (ML) models have been successfully utilized for a variety of composites applications including predicting shimming during assembly,[63] detection of defects during automated fiber placement,[64] damage characterization,[65–68] and real-time process simulation.[69,70] ML techniques can potentially accelerate characterization and help establish a process-microstructure-performance relationship in thermoplastic composites. However, ML methods typically require large amounts of data due to the stochastic nature of the problem.[71,72]

1.1.8.1 Gaussian Process Regression

Between all the different ML approaches, probabilistic machine learning techniques such as Gaussian Process Regression (GPR) have received much attention due to their capability of analyzing small datasets that are corrupted by noise and errors.[73] GPR is a non-parametric ML

approach to regression, where it can identify the underlying correlation in data while quantifying uncertainty of predictions.[73] This makes this approach quite suitable for analyzing noisy and high-dimensional small datasets.

GPR is based on the Bayes' Theorem, where the conditional probability of one event dependent on another event can be calculated in an alternative way. This relation is useful when the joint probability is difficult to determine, which is frequently the case. The Bayes' Theorem is as follows:

$$P(A|B) = \frac{P(B|A) * P(A)}{P(B)} \quad (1)$$

where $P(A|B)$ is the posterior probability, $P(A)$ is the prior probability, $P(B|A)$ is likelihood, and $P(B)$ is called evidence.[74] In the case of GPR, Bayes' Theorem gives a probabilistic approach to describe the correlation between data and a proposed model. Essentially, machine learning using this approach allows us to estimate the probability of a model being true given the observed data. This is called a maximum a posteriori estimation, and in applied machine learning is optimized using a maximum likelihood estimation.[74] These models compute a posterior distribution to quantify uncertainty in model estimates, instead of fitting a specific deterministic model to the test data. As new data are introduced, the posterior distribution is updated to improve the accuracy of the predictions. Understanding the computed scatter can assist in subsequent data collection to improve the regression accuracy.

For GPR training, a kernel or covariance matrix, Σ, is selected to describe correlations between datapoints in the observation domain. Given *n* measurements of Y_n for *n* inputs of X_n (i.e. prior), mean and variance functions, $\mu(X)$ and $\sigma^2(X)$, in the desired domain (i.e. posterior) can be calculated as:[75]

$$\mu(X) = \Sigma(X, X_n)\Sigma^{-1}(X_n, X_n)Y_n$$
$$\sigma^2(X) = \Sigma(X, X) - \Sigma(\mathrm{X}, \mathrm{X_n})\Sigma^{-1}(X_n, X_n)\Sigma(X_n, X) \quad (2)$$

The choice of kernel and its parameters significantly affect the performance of GPR, as it describes the interactions between predicted points and observation points. Therefore, it is important to choose a kernel that accurately represents the observed data.

In probabilistic machine learning, Naïve Bayes methods are the most commonly used, typically used with categorical features, whereas GPR is focused on continuous values by modeling features as Gaussian distributions.[76] Bayesian networks are another alternative, providing a graphical model that represents a process as a network of causal influences.[77] Gaussian mixture models, an unsupervised method, are used for clustering data.[78] Hidden Markov models prove useful in sequential data analysis, such as genome sequencing.[79]

Probabilistic machine learning offers advantages over deterministic modelling methods, such as deep neural networks, linear regression or decision trees, which establish a direct relationship between inputs and outputs[80]. Specifically, these machine learning methods usually require significantly less data compared to deterministic models. Probabilistic approaches also provide insights into the uncertainty of a model, unlike deterministic approaches that do not account for uncertainty, which may lead to potential inaccuracies. Moreover, deterministic models assume that all variables can be measured accurately, an assumption that is not always true. Lastly, probabilistic models provide a range of outcomes, allowing for the evaluation of various potential scenarios.

1.1.8.2 Convolutional Neural Networks

Extracting microstructural information using microscopic analysis is time-consuming and requires manually identifying features for data reduction and measuring desired quantities.

Leveraging ML techniques such as computer vision allows for quicker and more repeatable gathering of microscopic data.[81,82] For semi-crystalline thermoplastic composites, for example, it is difficult to identify crystal boundaries once crystals have fully grown into each other. In such a case, image segmentation can be used to identify these boundaries.[83] The convolutional neural network (CNN) has become increasingly popular for microscopic image analysis because of its efficiency in data processing. However, one downside of CNNs is that they are considered a "black-box" model, meaning that practical conclusions cannot be drawn from the model itself. Despite this, CNNs are the typical model used in image-based ML, such as in classifying objects or segmenting images.[81,82] Capsule networks present one alternative to CNNs for image recognition, capturing hierarchical relationships to improve generalization.[84] Another alternative involves the use of autoencoders, which are particularly useful in unsupervised applications by learning efficient data encodings.[85] Generative adversarial networks (GANs) also find application in image recognition, especially in image generation or augmentation.[86] Lastly, transformer models, traditionally associated with natural language processing, have been adapted for image recognition tasks. These models rely solely on an attention mechanism, mirroring the human ability to focus on specific visual elements sequentially.[87]

1.1.8.3 Principal Components Analysis

Principal Components Analysis (PCA) can provide a quantitative method for detecting small changes in test data. This method is commonly used in fields such as chemometrics. For example, PCA has been employed to classify archaeological ceramics through their FTIR spectra.[88] PCA also serves as a fundamental method for dimensionality reduction, particularly when dealing with an overwhelming number of input variables. In statistics, feature selection is another strategy to reduce variables by removing insignificant parameters.[76] Another statistical

method is manifold learning, where a low-dimensional projection of high-dimensional data is created, typically for the purposes of data visualization.[89]

1.2 Motivation

Thermoset composites, such as fiber-reinforced epoxy, are the primary structural composite materials used in aerospace. However, their production requires autoclaves and single-use bagging materials, which are expensive, time consuming, and have a significant impact on waste and the environment. In comparison, thermoplastics do not require long autoclave thermal cycles or freezers for storage, saving on energy and schedule costs. Moreover, thermoplastics can be remelted for recycling purposes, repairs, or rework, making them more sustainable and environmentally friendly. The recyclability of thermoplastics enables sustainable solutions for aerospace, and lower cycle times provides significantly improved production rates.

However, the process-microstructure-performance relationships in semi-crystalline thermoplastic composites are not well understood. For example, while the automated fiber placement (AFP) method is used to fabricate thermoplastic composites, the effects of short exposure to extremely high temperatures during consolidation on the autohesion process, as well as the formation of gaps and overlaps, and its effect on the mechanical performance and fatigue behavior of the material, are not well understood. In addition, the effect of processing and reprocessing on the degradation of thermoplastic composites has not been a research focus in the past. Part of the problem stems from material and process variabilities and uncertainties that affect the outcome. For example, crystallization kinetics are stochastic in nature, and thus, initial material conditions as well as previous process history significantly affect the crystalline morphology of the end-part. Additionally, current established approaches using numerical simulations and/or experimental methods are not equipped to investigate the underlying

correlations in such high-dimensional data domains that are intertwined with uncertainty and noise. While applying machine learning methods may mitigate part of the problems, these methods generally require a large amount of data.

To address the issues mentioned above, in this study, we propose a combined multi-faceted experimental framework incorporating probabilistic ML methods. This framework integrates techniques such as DSC, PLM, SAX/WAXS, FTIR, and mechanical testing to investigate the aspects of process-microstructure-performance and degradation relationships of the material. By incorporating probabilistic ML in the framework, underlying correlations are studied using sparse and noisy data. This understanding, while leveraging machine learning, can be used to optimize the processing of thermoplastic composites in-situ.

2 Methods

A summary of experimental techniques, investigated parameters, and materials used in this study is provided in Table 1. PLM was used to observe the crystal morphology during heating cycles. SAXS was used to characterize the lamellar spacing, and WAXS and DSC were used to measure the degree of crystallinity. Tensile strength was measured to determine how changes in the processing and morphology affected mechanical properties. FTIR was used to detect changes in the polymer related to degradation. Lastly, a wedge peel test was conducted on samples fabricated with AFP to measure the inter-ply bond strength. Three crystallization temperatures were investigated to determine their effect on crystal morphology, and three melt temperatures were evaluated for their effect on polymer degradation. Two test temperatures were used during tensile testing, and two environments were evaluated to study their effect on degradation. Three repeat cycles were evaluated to determine if reprocessing affected polymer degradation. Lastly, three materials were evaluated: PEEK film, PEKK/CF prepreg, and LM PAEK/CF prepreg.

Table 1. Summary of Experiments

Tests	Crystallization Temperature (°C)	Melt Temperature (°C)	Tensile Test Temperature (°C)	Environment	Cycles	Materials
PLM	310	385	20	Nitrogen	1	PEEK Film
SAXS	285	400	160	Oxygen	2	PEKK/CF
WAXS	235	420			3	LM PAEK/CF
Tensile Strength						
FTIR						
DSC						
AFP Wedge Peel						

The machine learning methods used in this study are provided in Table 2. PCA was used to reduce the number of wavenumbers for FTIR analysis. Yolov3 was used to identify crystals in a microscopic image, and U-Net was used to segment crystals from each other. GPR was used to fit probabilistic models and to generate response surfaces for experimental data.

Table 2. Summary of Machine Learning Methods

ML Method	Use
PCA	Dimensionality reduction
Yolov3	Image classification
U-Net	Image segmentation
GPR	Regression, Response surfaces

2.1 In-situ PLM

A method was developed to prepare thin and low volume fraction composite films, such as PEEK resin and carbon fibers, to conduct in-situ PLM using a microscope equipped with a heating stage to study thermoplastic composite crystallinity. A Victrex 75μm thick PEEK film was initially placed between two glass cover slips. A piece of Kapton film coated with silicone-based Frekote 710-NC mold release was laid on top of the PEEK film to prevent bonding to one of the cover slips.[90] 7μm diameter HexTow AS4 carbon fibers were heat cleaned at 350°C for 30

minutes to remove sizing while limiting damage to the fiber.[91] Fibers were pulled from the fabric and placed onto the glass cover slip without polyimide film. The full stack-up is shown in Figure 10.

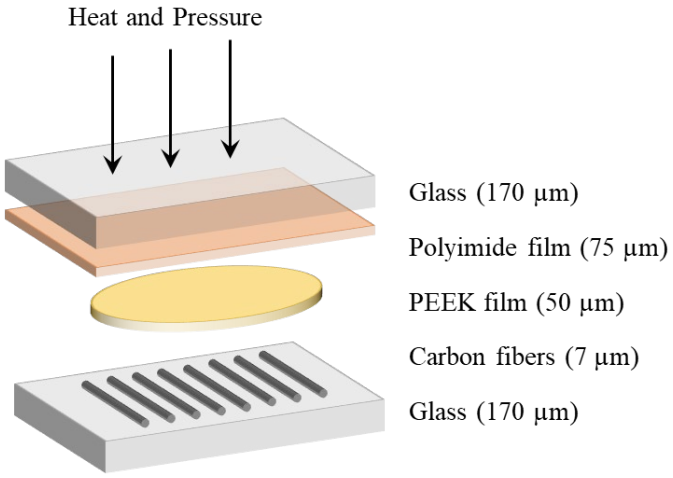

Figure 10. Sample stack-up used to produce thin PEEK samples with heat and pressure.

Samples were placed into a compression fixture in a DMA 850 from TA Instruments, and heat and pressure were applied. The stack-up was heated to 320°C and held for 20 minutes to stabilize, before heating to 400°C for 10 minutes. The heated 0.2mm^2 sample was compressed using 18N of force applied over one minute. The resulting samples were found to be 20±3µm thick using a Bruker DekTak profilometer. The fiber volume was estimated at 11% using image analysis of a micrograph of the compressed sample. The fiber volume was kept low to allow for comparison of resin rich areas to regions around fibers using PLM.

As shown in Figure 11, effects of four temperature cycles during cool-down on crystallinity were studied using in-situ PLM using a Linkam THMS600: a 310°C isothermal dwell, 285°C dwell, 235°C dwell, and a constant cooldown at 85°C/min to room temperature. Each dwell was held until the surface was fully crystallized as observed in the microscope, after which the samples were cooled down at 85°C/min. The resulting dwell for 285°C was 7.1 minutes and for

235°C was 1.2 minutes. The 310°C dwell was stopped after 60 minutes without completely crystallizing the whole surface before cool-down.

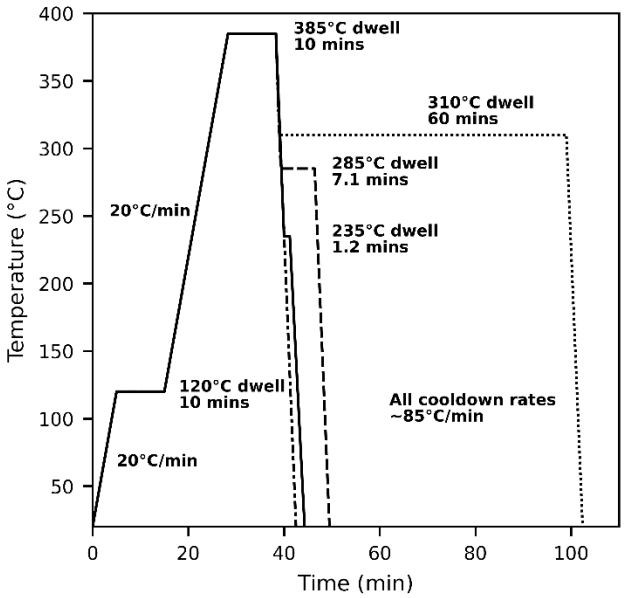

Figure 11. Heat cycle used for each PLM process. Three isothermal dwells at 310°C, 285°C, and 235°C and one constant cooldown at 85°C/min. Dwells were held until full crystallization.

Additional compressed samples were further processed in the Linkam THMS600 to investigate the effectiveness of a CNN to identify crystals. PEEK samples were heated at 20°C/min to 420°C and held for 2 minutes. After this dwell, the sample was cooled to 143°C at 10°C/min. The samples with carbon fiber were heated at 20°C/min to 385°C and held for 10 minutes. The samples were cooled down as fast as possible at 88°C/min to 310°C and held for 110 minutes. The longer hold time in the sample with carbon fiber was used to maximize the chance for the formation of transcrystalline regions.

2.2 FTIR and X-ray Scattering Sample Preparation

For FTIR and x-ray scattering tests, a 25µm PEEK film from Victrex (2000 series Aptiv), and a PEKK-FC/AS4D prepreg from Syensqo were used. Squares of approximately 6 by 6mm in

size were cut from the material. One sample was placed directly onto a microscopic glass slide, and four other samples were placed onto a piece of Kapton film surrounding the first sample. The glass slide, Kapton film, and samples were placed onto the heating block in a Linkam THMS600 hot stage, as shown in Figure 12. The sample placed directly onto the glass provides a representative view of the all the samples and allows for in-situ PLM observation of crystal growth.[26,92] However, this sample cannot be removed because it becomes bonded to the glass. The samples placed onto the Kapton film can be removed and further analyzed.

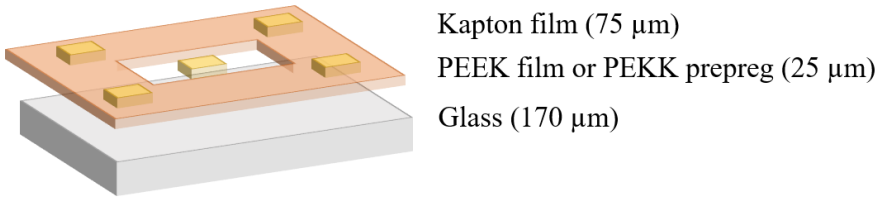

Figure 12. Sample configuration used in THMS600 hot stage.

Samples were heated in the THMS600 hot stage in both air and nitrogen. The samples were heated at a rate of 20°C/min to 120°C and held for 10 minutes to remove moisture, then heated to the melt temperature at a rate of 20°C/min and held for 10 minutes. Three melt temperatures were used for each material. For the PEEK film, 385°C was used as a standard melt temperature, 420°C as an extreme high, and 400°C as a midpoint. The temperature of 420°C is significant as it should ensure the removal of prior crystallization.[37,93] For PEKK prepreg, which has a lower melting temperature, the temperatures of 410°C, 392.5°C, and 375°C were used. After melting, the samples were cooled down at a rate of 140°C/min to 285°C for PEEK and 275°C for PEKK and held for 10 minutes. The samples were then cooled down to 143°C (T_g) at a rate of 65°C/min. The cooldowns were as fast as possible using the THMS600 without active cooling to minimize crystallization during cooldown. The heating cycles are shown in Figure 13.

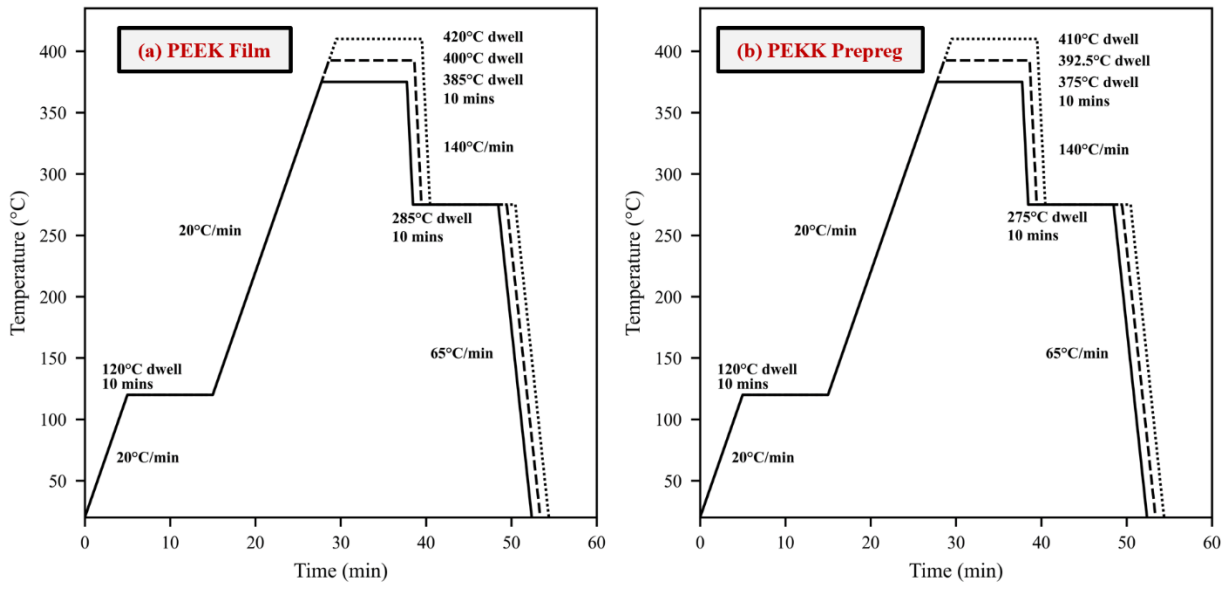

Figure 13. THMS600 heating cycles showing dwells and heating rates. (a) shows the heating cycle for PEEK film (b) shows the heating cycle for PEKK prepreg.

The center sample, as shown in Figure 12, was observed under an Olympus BX61 polarizing light microscope. Videos were recorded during heating, melting, and crystallization.

2.2.1 FTIR

Each sample was reprocessed three times at each melting temperature. After each heating cycle, FTIR spectroscopy was performed using a Bruker Vertex 70 with an attenuated total reflection (ATR) accessory (PIKE GladiATR). Measurements were performed in the range of 1900cm^{-1} to 400cm^{-1} with a spectral resolution of 1cm^{-1} and using 64 scans before Fourier transform. As an example, two normalized FTIR spectra are provided in Figure 14, to compare differences after thermal degradation. Specifically, the peaks at 1650cm^{-1}, the region above 1700cm^{-1}, the peaks at 1300cm^{-1}, the double peaks around 1100cm^{-1}, the peaks at 850cm^{-1}, and the peaks at 770cm^{-1} change before and after polymer degradation. These changes occur in peak height, peak slope, or peak shape, such as the formation of peak shoulders.

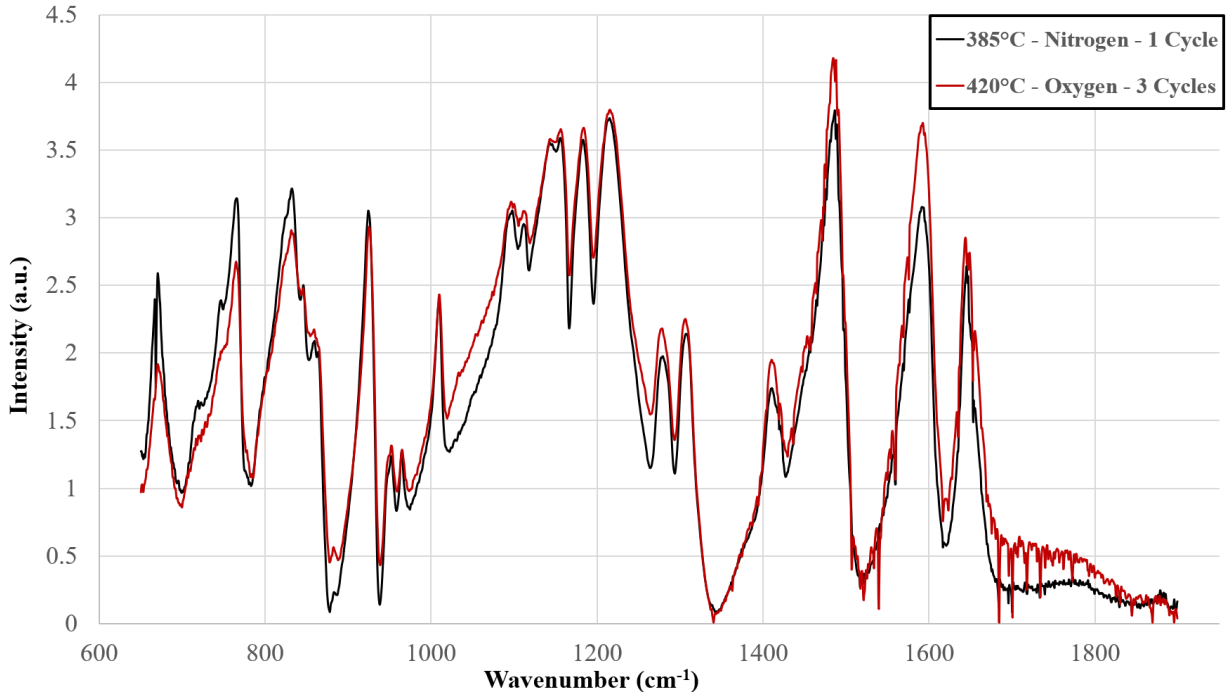

Figure 14. FTIR spectra comparison for PEEK film treated at 385°C in nitrogen and one cycle, and 420°C in oxygen and three cycles.

Principal Components Analysis (PCA) was utilized for dimensionality reduction, sample grouping based on principal components, and identification of the peaks that contributed the most to variance. Gaussian process regression (GPR) was applied to examine any correlations between the PCA results and melt temperature, processing environment (nitrogen and air), and reprocessing cycle count. The principal components were computed from a dataset of 117 FTIR spectra, and both PCA and GPR were performed using the Scikit-learn library in Python.[94]

2.2.2 X-ray Scattering

SAXS and WAXS were performed using a Xenocs Xeuss 3.0 System with a copper x-ray source with wavelength of 1.54Å and a Pilatus 300K detector. All measurements were performed under vacuum at an approximate pressure of 0.1mbar at room temperature. Two-dimensional

scattering patterns were integrated using the Xeuss software to obtain I(q) data. The scattering vector **q** is defined as the difference between the scattered and incident wave vectors and is related to the scattering angle θ as follows:

$$\mathbf{q} = 4\pi \sin \frac{\theta}{\lambda} \tag{3}$$

where λ is the characteristic wavelength of copper at 1.54Å. SAXS was measured in the **q** range of 0.001nm^{-1} to 3.0nm^{-1}, and WAXS was measured in the **q** range 0.03nm^{-1} to 6.8nm^{-1}. SAXS data were Lorentz corrected in a I(**q**)•**q**^{2} vs **q** plot.[95] The Lorentz correction accounts for the assumption that lamellae are infinitely large in two directions.[96]

Additionally, WAXS and SAXS were performed on an untreated piece of Victrex 2000G film, which is designed to be amorphous. The SAXS curve was evaluated to ensure the absence of any peak, indicating no crystalline lamellar structure and likely no crystallinity. The WAXS curve of the untreated 2000G film was compared to other samples as an amorphous standard to calculate the degree of crystallinity.

2.3 Machine Learning for Classification and Segmentation of Microscopy Images

A total of 1,355 microscopy images of crystals were captured using an Olympus BX61 polarizing light microscope with a Sony alpha 6000 camera. Examples of images captured at different time intervals for PEEK samples are shown in Figure 15, where spherulites can be observed nucleating and growing. The size of the spherulites shown in Figure 15 varies, as nucleation occurs at different times. The acquired image data was labeled using the LabelImg software in the YOLO format. Each crystal was labeled by a rectangle including its center coordinates, width, and height.

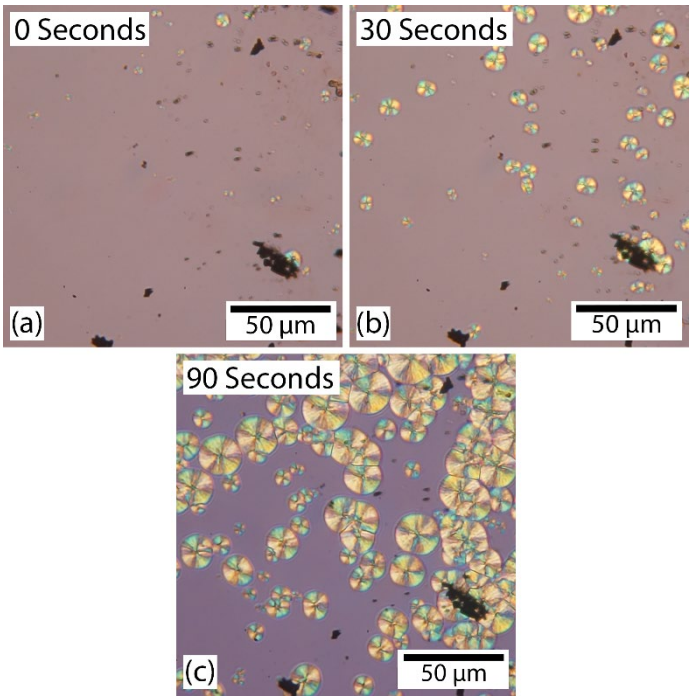

Figure 15. Microscopic image of crystal growth over time (a) growth has just started and is labeled 0 seconds (b) 30 seconds elapsed (c) 90 seconds elapsed.

To train machine learning models, PLM images were modified to create additional data by inverting the colors, rotating, creating monochrome images, adjusting saturation, and flipping. Examples of these image enhancements are shown in Figure 16. With this method, 5,420 images were generated and used to train a CNN. The trained CNN enables automatic detection of crystal growth in microscopic images.

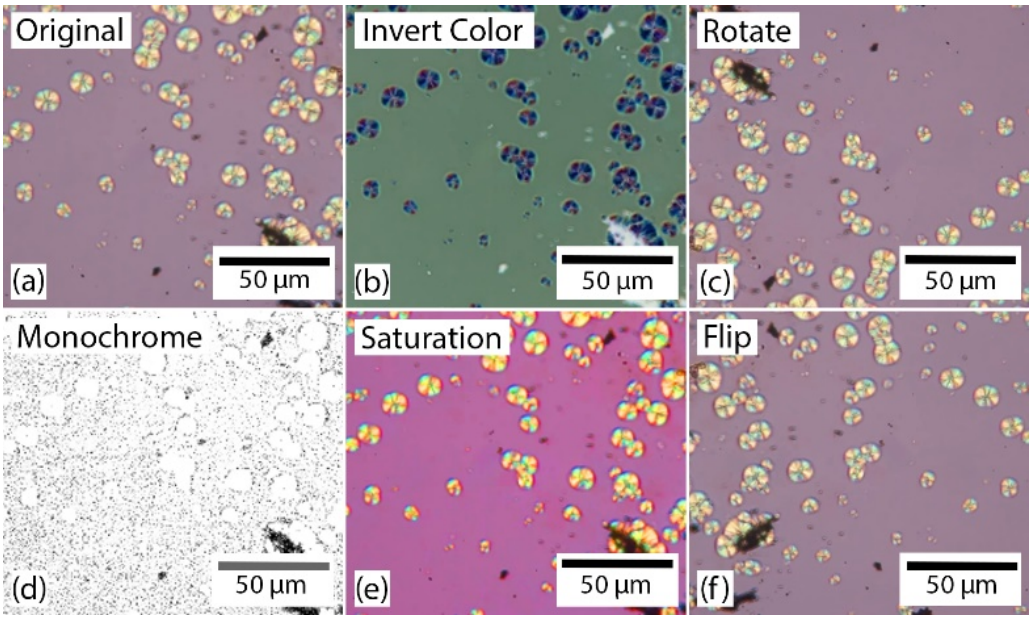

Figure 16. Comparison of the five data enhancement methods with the original microscopy image (a) original (b) color is inverted (c) rotation by 180° (d) black and white monochrome (e) increased saturation (f) mirrored.

Image data is split into 80% training and 20% test datasets. Next, an improved YOLOv3 model and U-Net model are trained on the picture data previously generated. YOLOv3 is used to identify crystals within the microstructure and U-Net is used to segment the image, particularly after crystals impinge when crystal edges are no longer clear. After that, a scale measurement model determines the crystal size in real-time based on pixel quantity (see Figure 17 for an overview). The analysis model consists of feature identification, feature tracking, and counting. For PEEK, the identification model is used to identify the growing crystals and to classify the shape of each crystal based on morphological classification. Next, the feature tracking model is implemented to track every individual crystal's dynamic behavior during in-situ microscopy. An example of crystal segmentation is shown in Figure 18.

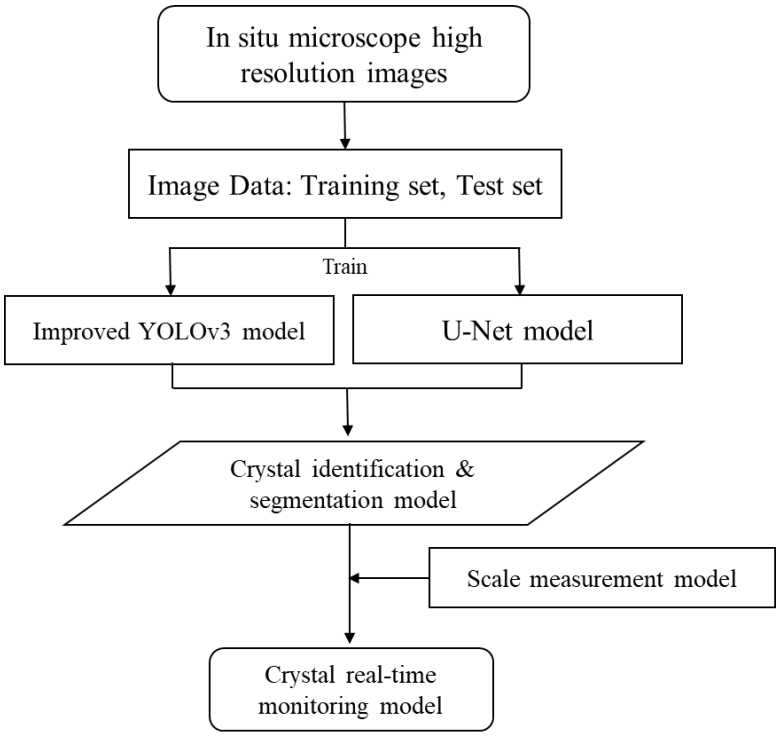

Figure 17. Flow chart of data processing method.

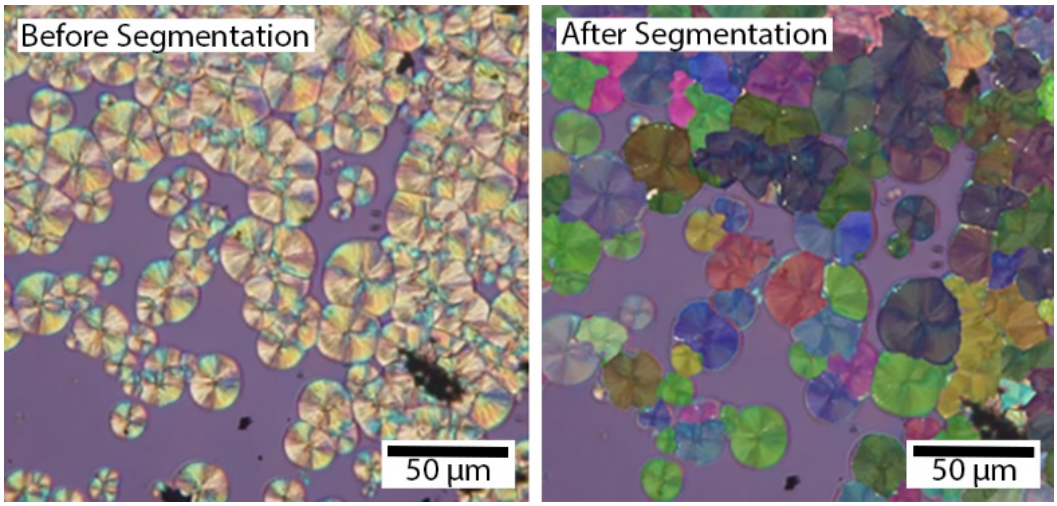

Figure 18. Example of crystal segmentation in PEEK.

To improve accuracy at the initial crystal growth, mosaic data augmentation was implemented. The mosaic process involves selecting four images and placing them at the four corners of a larger canvas. Crystals are then identified, and bounding boxes drawn with the

whole canvas to force the model to train in new contexts and improve the final model. After identifying crystals, the size is calculated by counting pixels in the segmented feature. The scale measurement functions are:

$$C_w = \frac{P_w}{WA} \tag{4}$$

$$C_H = \frac{P_H}{HA} \tag{5}$$

where C_w and C_H are the pixel width and height of the output image, W is the width of the camera pixel (3.88μm), H is the height of the camera pixel (3.88μm), A is the microscope magnification, P_w is the width of the output image, and P_H is the height of the output image. The pixel area of output image is $C_w \times C_H$.

2.4 Mechanical Testing

35mm by 4mm samples were cut from 25μm thick Victrex PEEK film and PEKK-FC/AS4D prepreg from Syensqo. The samples were melted and crystallized under 18N of pressure in a TA Instruments Discovery DMA 850 using a compression fixture. The PEEK samples were heated to 385°C, 400°C, or 420°C and held for 10 minutes, then cooled to 285°C at 85°C/min and held for 10 minutes. The PEKK samples were heat treated at about 10°C lower than the PEEK film. Each sample was treated in nitrogen or air. Additionally, samples were treated once or three times to emulate reprocessing cycles. Afterward, the samples were placed in a Linkam MFS350 hot stage that includes a tensile tester and a 600N load cell. The hot stage was placed under the Olympus polarizing light microscope and videos were taken during tensile testing at room temperature. Samples were tested at different displacement rates to evaluate the effect of strain rate. Testing was done either at room temperature or at 160°C. Testing at 160°C was chosen as it is above the glass transition for both PEKK (159°C) and PEEK (143°C). This set of parameters

were evaluated using an I-optimal design of experiments to screen significant parameters. A summary of the testing is provided in Table 3.

Table 3. Tensile Strength Design of Experiments

Material	Environment	Melt (°C)	Cycles	Displacement Rate (µm/s)	Test Temperature (°C)
1 ply prepreg	Nitrogen	375/385	1	0.1 to 62	20
2 ply prepreg	Air	393/400	3		160
PEEK film		410/420			

The PEEK film samples had pieces of PEKK prepreg taped on both sides to function as stiffening adherends and to shorten the gage area. The intent was to minimize out-of-plane deformation of the film during testing. In addition, a diamond scribe was used to start the cracks on both sides of the samples as schematically shown in Figure 19. Samples tested at 160°C were held for 5 minutes before the test.

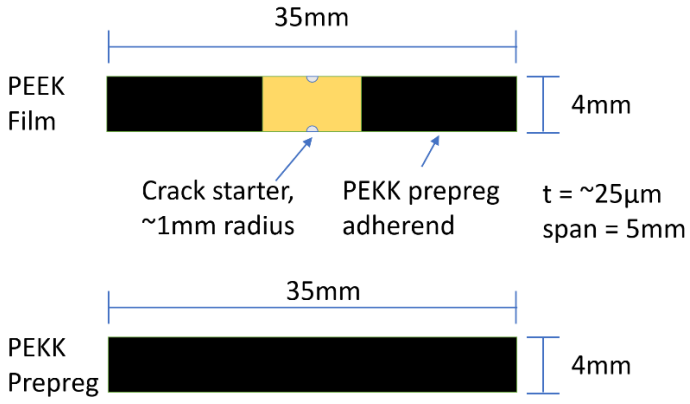

Figure 19. Coupon schematic for tensile coupons for PEEK film and PEKK prepreg.

2.4.1 Differential Scanning Calorimetry

Differential scanning calorimetry (DSC) was performed using a TA Instruments DSC 2500. There were two approaches used: one for film samples and one for prepreg samples. In the case

of prepreg, the samples were extracted from mechanically tested coupons. Resin samples had to be separately fabricated to produce samples with enough mass to generate a large enough signal for DSC analysis.

For the resin samples, 75μm thick PEEK film from Victrex was used. Eight layers of the film were cut into 1.25" diameter circles and stacked. Cirex released Kapton was placed on either side of the film stack, and the sample was compressed in the DMA. The sample was heated to 330°C at a rate of 18°C/min and held for 7 minutes. The sample was then ramped to 400°C at 7°C/min and held for 7 minutes while under 18N of force over one minute. After dwell, the sample was cooled down at 85°C/min to room temperature.

Samples were then melted and crystallized in a Linkam THMS600. The sample discs were placed on Cirex-treated Kapton which was placed onto a 0.17mm thick piece of microscopic glass. Heating occurred at 120°C/min to melt and then cooled 120°C/min to crystallization. A half-fractional factorial was generated where the factors were environment, melting temperature, crystallization temperature, and reprocessing cycles. The factors are presented in Table 4.

Table 4. Half-Fractional Parameter DSC Evaluation

Environment	Melting Temperature (°C)	Crystallization Temperature (°C)	Cycles
Air	385	285	1
Nitrogen	420	310	3

The discs and prepreg samples were cut to fit into the T-zero aluminum pans, to provide a minimum of 5mg mass for each test and ensure a sufficient signal response. The samples were heated from 25°C to 400°C at 10°C/min with nitrogen flowing at 50mL/min. Each sample went through this heat cycle twice to measure initial crystallinity.

The equation for calculating the mass degree of crystallinity in pure resin is given as:

$$X_{mc} = \frac{\Delta H_{melt} - \Delta H_{crystallinity}}{\Delta H_f} \quad (6)$$

The area under exothermic crystallinity peaks observed during heating in the DSC heat flow curves (noted as $\Delta H_{crystallinity}$) was subtracted from the area under the endothermic melting peaks (noted as ΔH_{melt}) to determine the initial crystalline enthalpy of the samples (X_{mc}). This enthalpic value was compared to the theoretical full crystalline enthalpy, which is estimated to be 130 J/g for both PEEK and PEKK (noted as ΔH_f).[11,97]

When determining the degree of crystallinity in prepreg, the value is adjusted for the ratio of fiber mass as follows:

$$X_{mc} = \frac{\Delta H_{melt} - \Delta H_{crystallinity}}{(1 - X_{mr})\Delta H_f} \quad (7)$$

where X_{mr} is the mass fraction of the fiber reinforcement, which is approximately 67% when the fiber volume is assumed to be 60% for both PEEK and PEKK (assuming negligible porosity). Finally, the mass fraction crystallinity can be converted to volume fraction crystallinity using the following relationship:

$$X_{vc} = \frac{X_{mc}\rho_a}{\rho_c - X_{mc}(\rho_c - \rho_a)} \quad (8)$$

where ρ_a is the density of amorphous material (1.26g/cm^3 for PEEK[4], and assumed the same for PEKK), ρ_c is the density of the crystalline material (1.40g/cm^3)[4], and X_{vc} is the volumetric crystallinity.

2.5 Automated Fiber Placement

The material selected for this study was Toray Cetex TC1225 low melt polyaryletherketone (LM-PAEK), reinforced with unidirectional (UD) T1100G intermediate modulus carbon fibers.

LM-PAEK has a glass transition of 147ºC and melt temperature of 305ºC.[98] The substrate panels were fabricated using 12-inch wide tape in a hot press, and the tows for AFP were ¼-inch in width.

2.5.1 Substrate panel fabrication

Two sheets of Airtech Thermalimide RCBS film were used as the material interface during hot press consolidation, with surfaces treated with three coats of Sicomin Cirex 041 WB release agent. The substrate panels were 0.6m by 0.6m (24 by 24in.) and were fabricated from the 0.3m (12in.) wide roll of TC1225 LM-PAEK. Before the hot press consolidation, layers were tacked together at the seams using a soldering iron.

The substrate panel was then placed into a Wabash 45 metric ton heated platen press. Half inch thick 6061 aluminum plates were used to alleviate temperature gradients on the heated platens. For direct temperature monitoring, a National Instruments data logger was used. A K-type thermocouple was placed under the substrate panel in between the Thermalimide film and the aluminum plate. The thermocouple's tip extended about 1 inch beyond the panel's edge.

The press cycle started with a clamp force of 1.8 metric tons to initialize the cycle and allow both platens to reach 38ºC. The temperature was then ramped to 310ºC and held for 10 minutes to ensure uniform heating. Subsequently, the platens were heated to 338ºC, with the compaction force increasing to 18 metric tons over a span of 5 minutes. Once the temperature reached between 330ºC and 340ºC, the compaction force was reduced to 1.8 tons. Simultaneously, the air cooling was turned on cooling the panel at an approximate rate of 1ºC/min. Upon reaching 147ºC, water cooling took over to room temperature. The substrate panels were then solvent cleaned before subsequent AFP processing.

2.5.2 Automated fiber placement

The AFP machine utilized for the process was an Electroimpact-enhanced KUKA KR1000 L750 Titan. The AFP head operated with an 8-spool configuration and a Variable Spot Size Laser (VSSL) heating method. Machine programming was performed using the VERICUT composite programming (VCP) software. The deposition surface was a hard mounted aluminum vacuum table. The substrate panels were secured to the vacuum table by creating a Thermalimide film border around the panel and sealing the gap with tape. This ensured that the substrate panel remained stationary and flat during the tape deposition. A picture of the substrate panel secured to the vacuum table is provided in Figure 20.

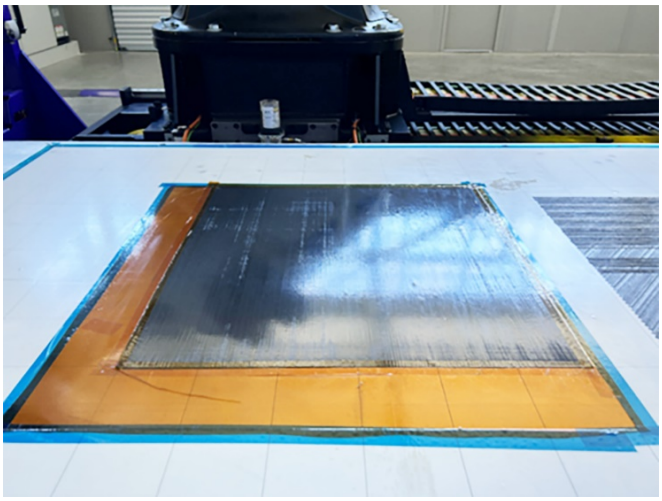

Figure 20. An example of how each substrate panel was secured. The orange film taped around the panel is Thermalimide film. The blue tape is securing the Thermalimide film to a lower temperature resistant white Mylar film.

A factorial test design was employed to cover a suitable range of processing parameters. This design assessed three speeds, two compaction forces, and five temperatures. A list of these values is provided in Table 5. In total, three panels were fabricated to complete a full factorial distribution of the processing parameters.

Table 5. Distribution of AFP Processing Parameters

Roller Head Force (N)	Deposition Speed (m/min)	Target Temperature (ºC)
667	7.6	330
1112	12.7	355
	20.3	380
		405
		430

The selected temperature range was based on the manufacturer's recommended 380ºC for optimal processing. These are target temperatures, with the actual temperature controlled by a curve scaler in the machine's software. The scalar values were set based on initial AFP deposition tests. An FLIR camera on the AFP head monitored temperature in real-time, capturing the highest and lowest values during deposition. It also allowed for an estimation of temperature variation as tape was laid down. An important point to note is that while IR temperature measurements provide valuable data, they may not fully capture the thermal gradient within the material due to surface emissivity variations and potential reflections.

2.5.3 Fabrication and testing details

Substrate panels were made of two UD plies [0,0], with additional tapes deposited on top with the same [0,0] orientation. The panels were designed to encompass ten head passes. In each pass, three strips of material were laid down along the length of the panel. Each strip contained two coupons. The panel was then separated in half perpendicular to the deposition pass to create six test samples deposited within the same head pass and processing conditions as depicted schematically in Figure 21. Each pass was repeated, laying down a second layer using the same processing settings. Thus, a single panel held 60 test samples. Three panels were fabricated, amounting to 180 test samples.

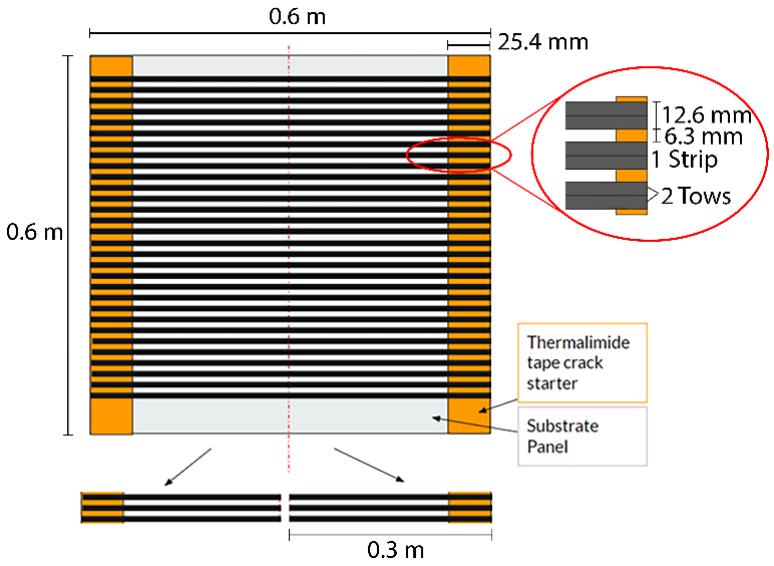

Figure 21. A schematic illustration of tow deposition onto the substrate panels.

The test width of each sample was approximately 12.7mm wide (0.5 inches) or two tows. The coupons were 0.3m in length (12 inches) with the crack starter placed 25.4mm (1 inch) into the sample. Coupons were mounted in a wedge peel test fixture.[99] A picture of the testing setup is shown in Figure 22. The wedge peel tests were conducted using an Instron 5585H load frame, equipped with a 2.5kN load cell and fine-tooth tensile grips. The load cell was recalibrated after every six tests (one set of processing conditions). The extension was measured from the load frame cross head displacement and was reset before each test. The tests were conducted at a constant displacement rate of 1mm/s to pull the wedge peel sample upward through the stationary test fixture while measuring the peel force.

Test data was filtered to eliminate the first 20mm of extension to remove the initial sample slacking as well as any initial force spike from the first separation.

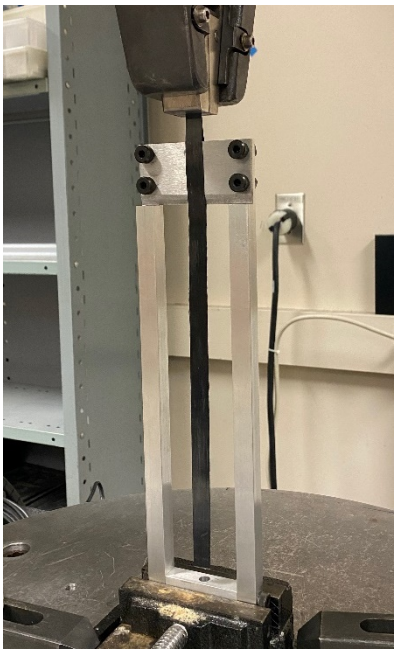

Figure 22. The machined wedge peel fixture.[99]

2.6 Scanning Electron Microscopy

A Phenom ProX SEM with a 15kV beam was used to capture images of failure surfaces and to analyze the associated failure modes. Samples were coated in gold using a gold sputterer before imaging.

3 Results

3.1 Crystallization in Polarized Light Microscopy

A comparison of the final microstructures in all four cycles is shown in Figure 23. Data for spherulite and transcrystalline growth rates are summarized in Table 6. To calculate growth rate, spherulite diameter and double the transcrystallinity length normal to the fiber surface are measured at each frame. The 285°C and 310°C isothermal dwells, shown in Figure 23(a) and (b), produced the largest spherulites and transcrystalline regions. The 235°C dwell and 85°C/min cooldown as shown in Figure 23(c) and (d) produced small spherulites that did not have clear edges in PLM. This may be due to the limitation of the light microscopy technique. There was

slight transcrystalline growth at 235°C, and more consistent transcrystalline growth after an 85°C/min cooldown. To fully resolve the smaller transcrystalline regions in Figure 23(c) and (d), carbon fibers were put out of focus, making them look smaller than Figure 23(a) and (b). All samples had a large amount of variation in growth rate data as listed under Table 6.

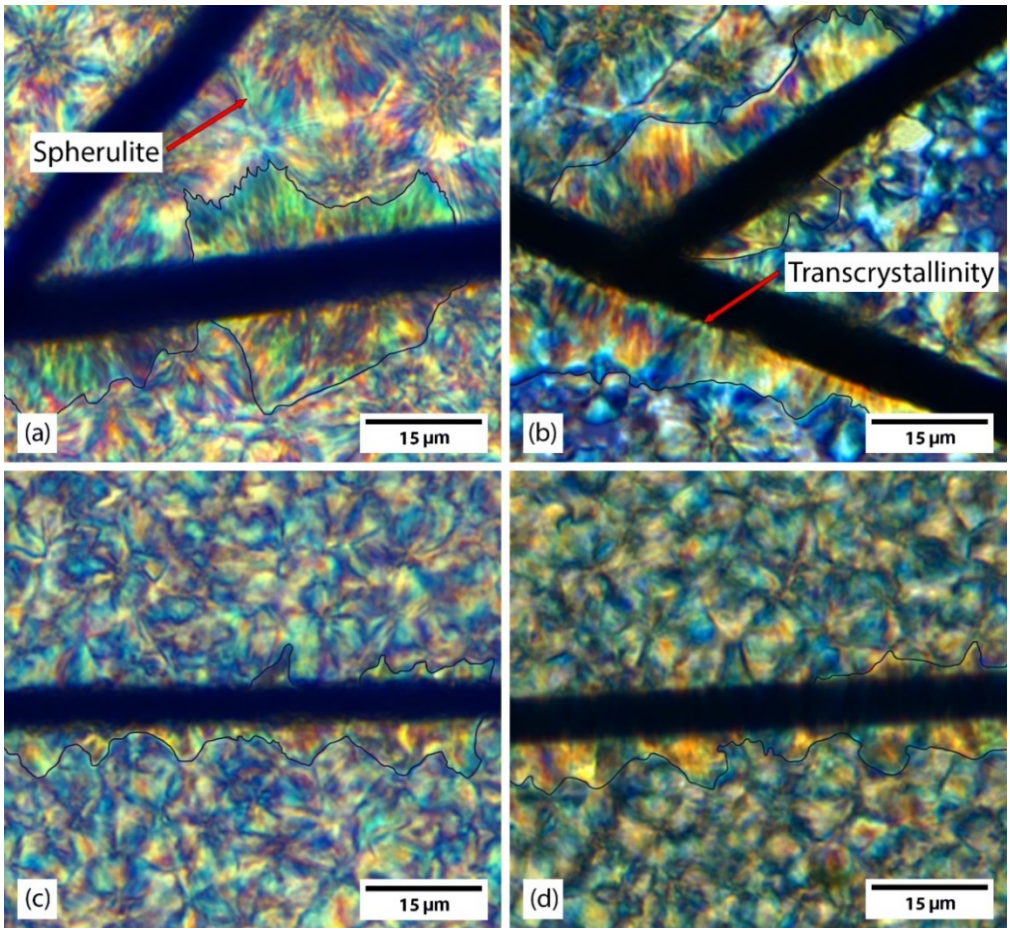

Figure 23. Morphology changes in each process. (a) a 285°C isothermal dwell produces larger transcrystalline regions and large spherulites. (b) the 310°C dwell produces the largest spherulites and transcrystalline regions. (c) a 235°C dwell produces minor transcrystalline growth and small spherulites that do not resolve in PLM. (d) an 85°C/min cooldown shows minimal transcrystalline growth and spherulites do not resolve.

Table 6. Growth Rate Data for Spherulites and Transcrystallinity Regions

Heating Cycle	Spherulite (μm/min)		Transcrystallinity (μm/min)	
	Average	Standard Deviation	Average	Standard Deviation
310°C	1.0	0.2	0.4	0.2
285°C	8.1	2.1	10.1	7.4
235°C	40.0	12.2	37.8	13.5
85°C/min	41.7	19.0	32.5	12.6

3.2 Growth Rate Analysis

As mentioned earlier, growth rates were measured from in-situ microscopy videos for both spherulites and transcrystalline regions. Measurements of growth rates, G, are shown in Figure 24 as a function of temperature, T, and crystal size, D. Mean and standard deviation data are provided in Table 6. From these results, it can be observed that the growth rate was fastest in samples with high undercooling, specifically the 235°C and 85°C/min cycle samples. These samples had the largest variation in growth rate as well. Based on mean data, transcrystallinity typically grew slower than spherulites. This may be attributed to the growth of nearby spherulites slowing down transcrystallinity growth. There is some error in identifying the edges of spherulites and transcrystalline regions. As the crystalline feature approaches the pixel size, it becomes increasingly difficult to accurately find the edges. To minimize the measurement errors, care was taken to only measure spherulites and transcrystalline regions where no impinging had occurred and were clearly separated from others. There were 3.76 pixels/μm in our microscopy images. While the smallest measured spherulite had a diameter of about 3.7μm, the largest was about 21.4μm. However, most measured features were between 5 to 15μm. Based on this, and assuming ±2 pixels error in measurements, the average estimated error for all measurements was about 6%.

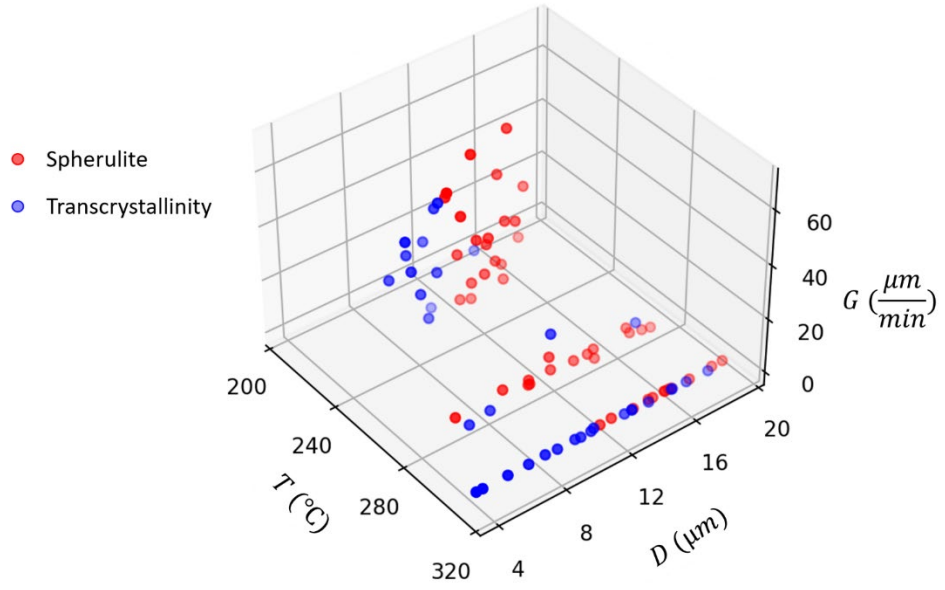

Figure 24. Growth rate data (G) measured from microscopy videos at different temperatures (T) and for different crystal sizes (D).

In the first step, spherulite and transcrystalline growth rate data were fit to the Lauritzen-Hoffman equation below:[13,14]

$$G = G_0 \exp\left[\frac{-U^*}{R(T_c - T_\infty)}\right] \exp\left[\frac{-K_g^G}{T_c \Delta T f}\right] \quad (9)$$

where the first exponential term describes the contribution of the diffusion process to growth, and the second exponential term is associated with secondary nucleation. Here, G is the growth rate, G_0 is a growth rate constant, U^* is the activation energy for diffusion across melt and crystal boundary (2800J/mol)[100], R is the universal gas constant, T_∞ is 30°C less than glass transition temperature, T_g (143°C for PEEK), T_c is the isothermal crystallization dwell temperature, K_g^G is a parameter that is proportional to the energy barrier for secondary nucleation, $\Delta T = T_m^0 - T_c$ is the equilibrium melting temperature (380.5°C)[100], and f is a correction factor equal to $2T_c/(T_m^0 + T_c)$. The logarithmic transformation of Equation 9 results in the following relationship:

$$\ln(G) + \frac{U^*}{R(T_c - T_\infty)} = \ln(G_0) - \frac{K_g^G}{T_c \Delta T f} \quad (10)$$

where the left side expression is linearly correlated to $1/(T_c \Delta T f)$. Based on measured growth rates, initially a linear fit was found for spherulite growth following Equation 10, however, transcrystallinity deviated from the Lauritzen-Hoffman equation and showed a nonlinear correlation. To better understand these underlying correlations for different crystal types, GPR regression was used. To take advantage of existing theory, a transformed dataset based on Lauritzen-Hoffman equation was used for GPR training with dimensions of:

$$X = \left(\frac{1}{T_c \Delta T f}, D\right) \text{ and } Y = \ln(G) + \frac{U^*}{R(T_c - T_\infty)} \quad (11)$$

GPR training was performed using the scikit-learn library in Python.[94] Data was split into 80% training data and 20% validation data. For spherulite growth, following Lauritzen-Hoffman theory, a combination of linear white noise kernels was initially selected:

$$\Sigma(x_i, x_j) = c * \left[\sigma_0^2 + x_i \cdot x_j\right] + \sigma_e^2 I_n \quad (12)$$

where c is a constant, σ_0^2 is a constant controlling the inhomogeneity of the linear kernel, σ_e^2 is the variance of noise, and I_n is the identify matrix. In this study, default values of σ_0^2 and σ_e^2 equal to unity were used. Based on this linear correlation, the trained GPR model showed an accuracy of 96% for the validation data. A fitted mean response surface from the GPR model is shown in Figure 25. For transcrystallinity, initially a kernel similar to Equation 12 was selected. However, this only showed an accuracy of 88% for the validation set. After this first trial, a second kernel was selected as a combination of the squared of the linear kernel and white noise kernel:

$$\Sigma(x_i, x_j) = c * \left[\sigma_0^2 + x_i \cdot x_j\right]^2 + \sigma_e^2 I_n \quad (13)$$

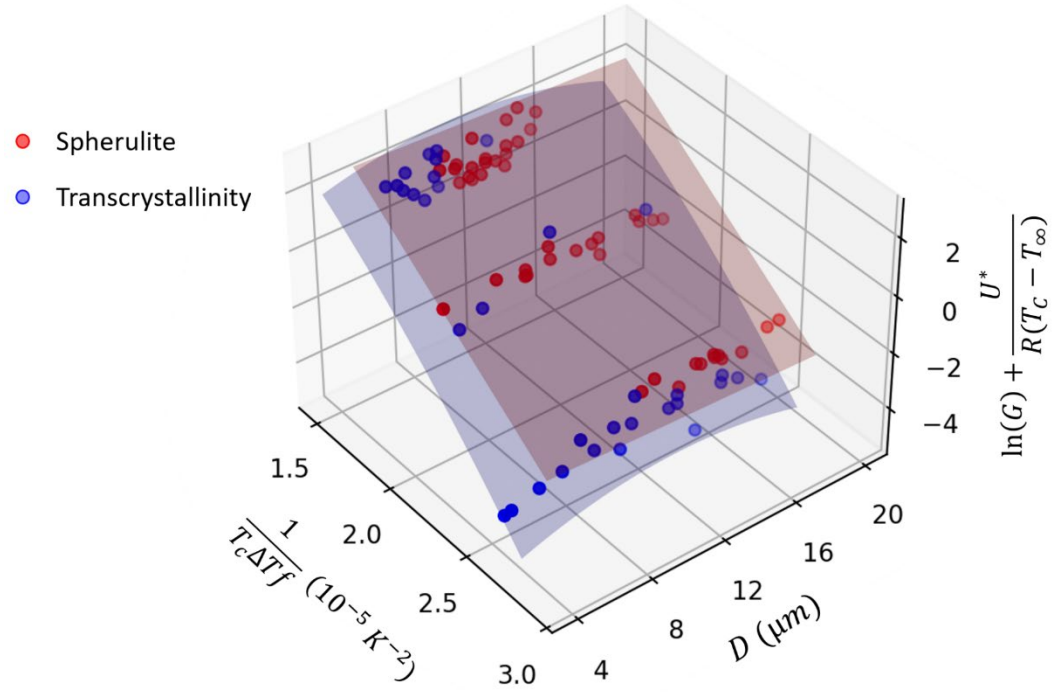

Figure 25. Fit GPR models to spherulite and transcrystallinity growth rate data in the transformed Lauritzen-Hoffman domain (Equation 10).

Upon training, GPR showed an accuracy of 98% to predict the validation dataset. The fit mean response surface for transcrystallinity growth is shown in Figure 25. This figure clearly shows that while spherulite growth follows a linear correlation as predicted by Lauritzen-Hoffman Equation 10, transcrystallinity shows a nonlinear correlation. From these GPR models, energy barriers for secondary nucleation in Lauritzen-Hoffman equation (K_g^G) can be estimated equal to 4.7 ($10^5 K^2$) for spherulites and 5.5 ($10^5 K^2$) for transcrystallinity. From these estimated values (also confirmed in Figure 25), it can be observed that growth rates are in general faster for spherulites compared to transcrystalline regions.

3.3 Classification and Segmentation

As a first step, spherulites were the focus of initial classification and segmentation study. An example of YOLOv3 identifying crystals with green boundary boxes is shown in Figure 26. As crystals nucleate and grow, more boxes are drawn and expand with the crystals. Figure 26(a) shows the first identifiable nucleated crystals. Figure 26(b) and (c) show growth after 30 and 90 seconds, respectively.

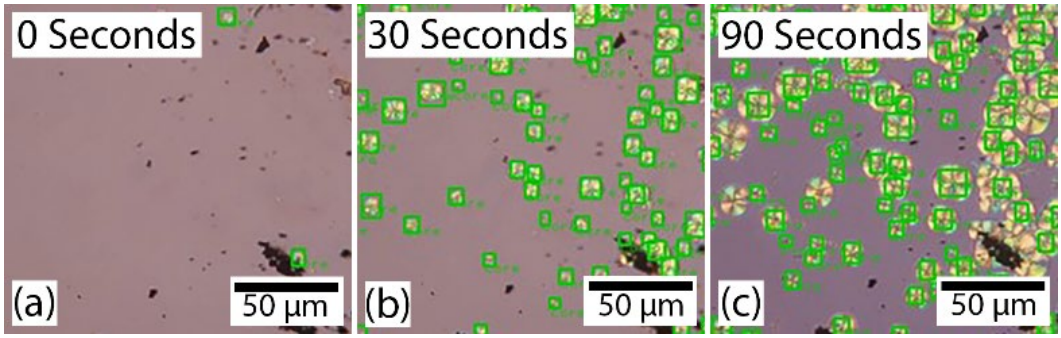

Figure 26. Crystal recognition over time. Green boxes are shown over growing crystals.

The U-Net model is used to segment spherulites and transcrystallinity in a sample with fibers. The segmentation result is shown in Figure 27. The transcrystalline regions are shown in red, and the fully separated spherulites in green. The black regions include carbon fiber and amorphous regions. The model successfully separates the spherulites, transcrystallinity, amorphous regions, and carbon fibers. The transcrystalline regions can be seen clustered around the carbon fibers, while the spherulites gather between fibers nucleating from the amorphous regions.

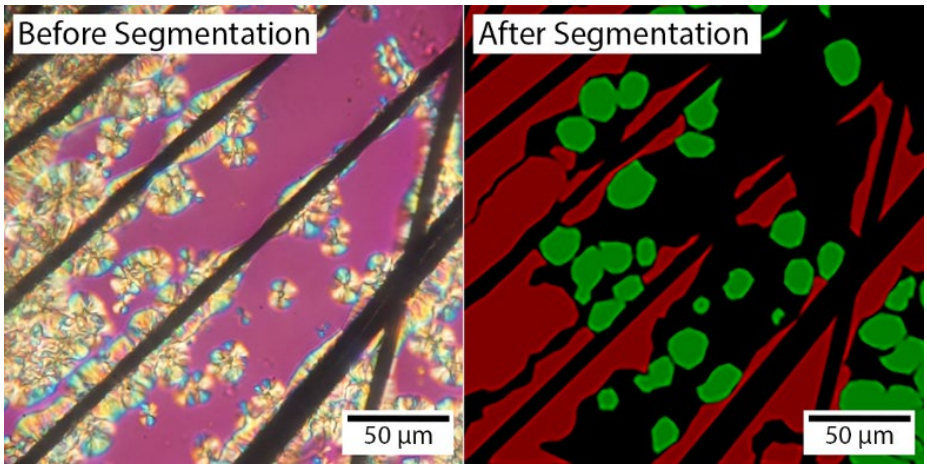

Figure 27. Crystal segmentation with carbon fiber. Left is original and right is segmented. Green is spherulites, red is transcrystalline regions growing from fibers, and black includes amorphous regions and carbon fibers.

From measurements of the spherulite sizes, three phases of crystal growth can be observed in Figure 28. The first phase spans from 0s to 30s, characterized by slower growth. The second phase from 30s to 60s shows rapid growth, followed by the last phase after 60s, where the size has plateaued. These phases are consistent with nucleation and growth theory.[101] During the initial phase, nucleation has not yet occurred, and is a random event that is influenced by the formation of nearby nuclei. Nucleation is infrequent when no nuclei are present. However, as nuclei begin to form, they influence the formation of further nuclei, leading to an increase in the rate of formation. In the next phase of growth, both nucleation and growth occur rapidly. After the formation of nuclei, growth is driven by thermal energy and the availability of amorphous molten polymer. In this phase, although thermal energy is decreasing, its effect is minimal. The availability of unordered polymer chains that can be used to increase the growth is significant. As the crystals grow closer to each other, growth slows down due to the decreasing pathways for moving polymer chains.[101] Eventually, these crystals impinge and stop visible growth altogether.

Crystal structures continue to grow beyond this point, but further crystal growth cannot be observed through in-situ microscopy.

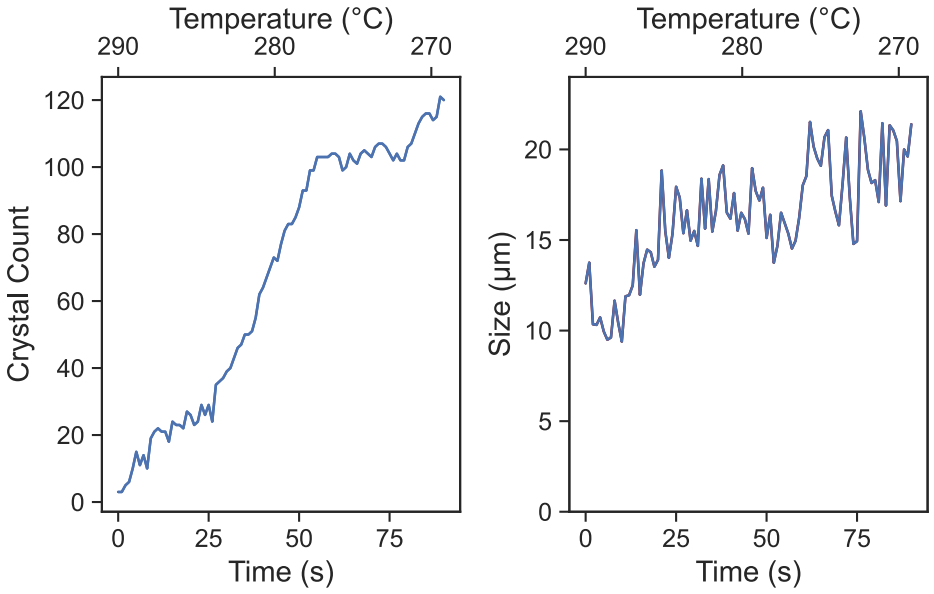

Figure 28. Crystal count and size over time and temperature. **Left:** shows the number of crystals with respect to temperature. **Right:** shows the change in average size with changing temperature.

Another feature in Figure 28 is the existence of jitter or noise. Normally, crystals only grow larger and do not shrink or disappear after their generation. However, in some instances the number of crystals decreases in Figure 28, for example from 29 to 24 crystals at 25s. This is likely due to the amount of training data, and improvements are expected with future iterations and additional training data. Additionally, at the later stages of crystal growth, crystals impinge into each other, and boundaries become indistinct making it difficult for the algorithm to identify and count the crystals across the micrograph. Crystals also stack and merge with further processing, becoming less visually discernible. As a result, the model may lose track of them.

Given the amount of noise in data, Gaussian process regression (GPR) was used to interpolate and fit the crystal size distribution during processing.[92,102] The fitted crystal

distribution surface is shown in Figure 29. The x-axis and y-axis represent time and crystal size, and the z-axis represents the distribution probability of different crystal sizes. As time increases, crystal size stabilizes around an average size of approximately 25µm. At the start of nucleation, all observed crystals are small, and the number of crystals is limited, which leads to a large peak in probability at early times and small sizes. This is represented by the initial spike in probability, which is smoothed out as time increases. The bumpiness in the GPR model is an artifact due to noise and amount of training data available.

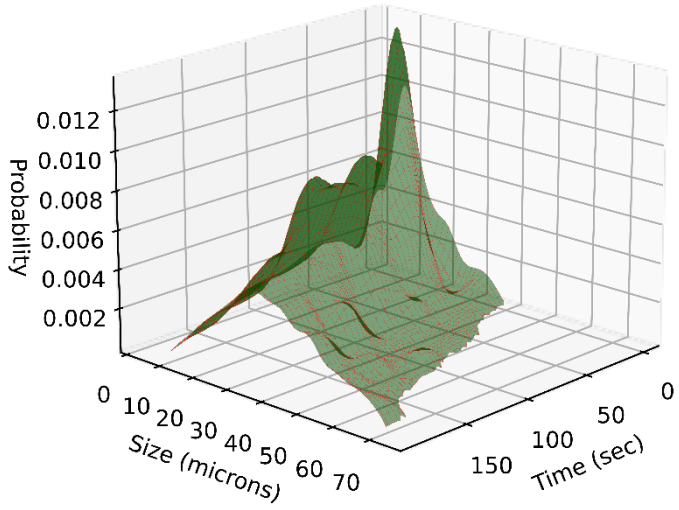

Figure 29. The distribution function of crystal average size with respect to time.

3.4 Polymer Degradation

3.4.1 Polarized Light Microscopy

The PLM technique is a through-transmission method, which means that carbon fibers block light, making it impossible to observe the PEKK prepreg samples using PLM. In most PEEK film samples, the growth rate was too fast to be reliably captured on video. End-state example micrographs are presented in Figure 30 for a PEEK film processed at 420°C in nitrogen. After one cycle, as shown in Figure 30(a), spherulites are 20-30µm in diameter. Figure 30(b) shows that the crystals are about twice the size, at 45-60µm, after another 420°C cycle. One more cycle,

as shown in Figure 30(c), reveals a few small crystals at 4-8µm surrounded by amorphous material. In general, repeated cycles and higher melt temperatures lead to larger crystals. As the polymer degrades, less material is available for nucleation, which lowers the nucleation rate. A lower nucleation rate will create larger crystals as the crystals that do nucleate will have more space to grow before impingement.[37] In the case of Figure 30(c), growth was slow enough that after 10 minutes, impingement had not occurred, and upon cooldown, the rest of the molten polymer remained amorphous. Given enough time, the sample in Figure 30(c) would likely have produced spherulites larger than those observed in Figure 30(b).

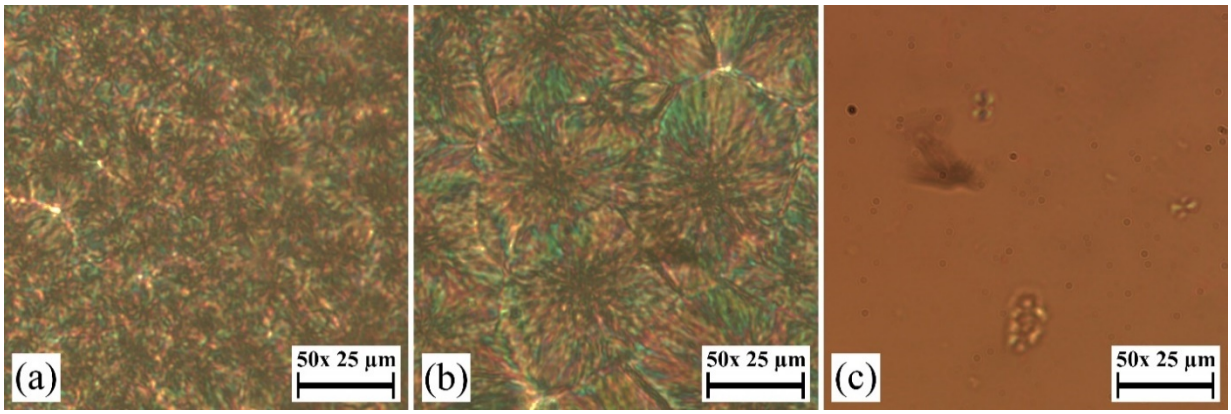

Figure 30. Micrographs of a PEEK film after thermal cycling at 420°C in nitrogen. (a) shows 20-30µm spherulites after one cycle (b) two cycles yields 45-60µm crystals (c) three cycles leads to incomplete growth and 4-8µm spherulites.

3.4.2 Principal Components Analysis

To simplify analysis, PCA was performed on the FTIR spectra data, reducing the data from 2500 dimensions to four principal components. Only the 1900cm^{-1} to 650cm^{-1} range was evaluated since the 650cm^{-}1 to 400cm^{-}1 range is noisy and does not contribute to identifying functional groups involved in degradation. Data was normalized before PCA. The first four principal components explained 90.1 % of the variance for the combined dataset. The first and

second principal components are plotted in a score plot for both materials as shown in Figure 31. Two distinct groupings can be identified between the PEEK film and PEKK prepreg. This is likely due to differences in the polymer chains and the presence of carbon fiber in the PEKK prepreg.

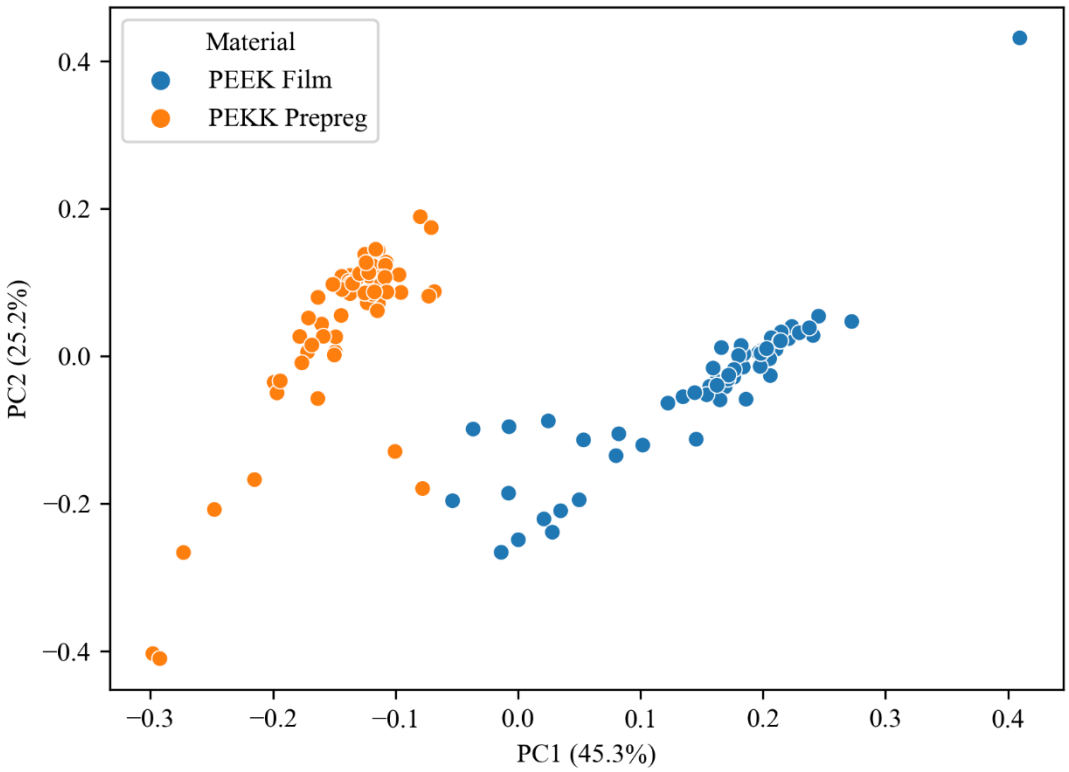

Figure 31. Score plot showing both the PEEK film and PEKK prepreg indicating a significant difference between the materials.

Since the materials are clearly separated into distinct groups, and the differences can be explained without involving degradation, PCA was repeated for each material separately. Table 7 shows the contributions to variance for the first four components for each material. PEKK has a much higher contribution from the first component, whereas the first three components in PEEK contribute significantly.

Table 7. Variance Explained by Principal Components for PEEK Film and PEKK Prepreg

Material	PC1 (%)	PC2 (%)	PC3 (%)	PC4 (%)
PEEK Film	42.3	31	15.6	3.8
PEKK Prepreg	67.3	13.3	5.5	3.2

Score plots were generated for both PEEK film and PEKK prepreg based on the first two components, and comparisons were made between melt temperatures, cycles, and environment. Some clustering was observed for the 400°C melt temperature in PEEK, but otherwise, no clear clustering was identified.

To identify the peaks that contribute the most to variance, the normalized FTIR spectra were processed in Origin software, and a 2nd derivative was calculated for all data.[88] PCA was performed on these 2nd derivative values and the peaks associated with the principal components were identified. In PCA, an important metric for assessing the impact of a variable is the loading, which measures the covariance between the original variables and the unit-scaled components. The larger the loading value, the greater the impact on the calculated principal components.[103] PCA loading values greater than 0.05 are identified in Table 8. The functional groups identified are similar to those that have been found in previous thermal degradation work on PEEK.[8] Peaks in the 1700cm^{-1} to 1733cm^{-1} range that contributed to variance are likely due to intramolecular bonding and the formation of dibenzocyclopentanones. Peaks at 1684cm^{-1} and 1650cm^{-1} are related to ketone stretching near the benzenes. 1635cm^{-1} is likely due to C=C stretching at the benzophenone, and 667cm^{-1} and 668cm^{-1} due to C=C bending. Changes in these FTIR peaks suggest that degradation involves intramolecular bonding.[8] Intermolecular bonding and cross-linking were not identified. Pascual et al. identified these peaks under considerably higher

thermal energy and near charred PEEK samples.[8] Cross-linking may not be detectable in FTIR in PEEK except in extremely high-temperature exposures.

Table 8. Wavenumbers and Functional Groups Identified by PCA

Wavenumber (cm^{-1})	Functional Group
1700-1733	Formation of dibenzocyclopentanones
1684, 1650	Ketone stretching around benzenes
1635	C=C stretching at benzophenone
667-668	C=C stretching, bending

3.4.3 X-ray Scattering

The collected WAXS data from the samples was compared to an amorphous standard. The area under the amorphous curve and the crystalline curve were determined by integration, and the degree of crystallinity was calculated as follows:[104]

$$Degree\ of\ Crystallinity = \frac{A_{crystal} - A_{amorphous}}{A_{crystal}}\ x\ 100\% \tag{14}$$

where $A_{crystal}$ is the area under the crystalline curve and $A_{amorphous}$ is the area under the amorphous curve. See Figure 32 for an example.

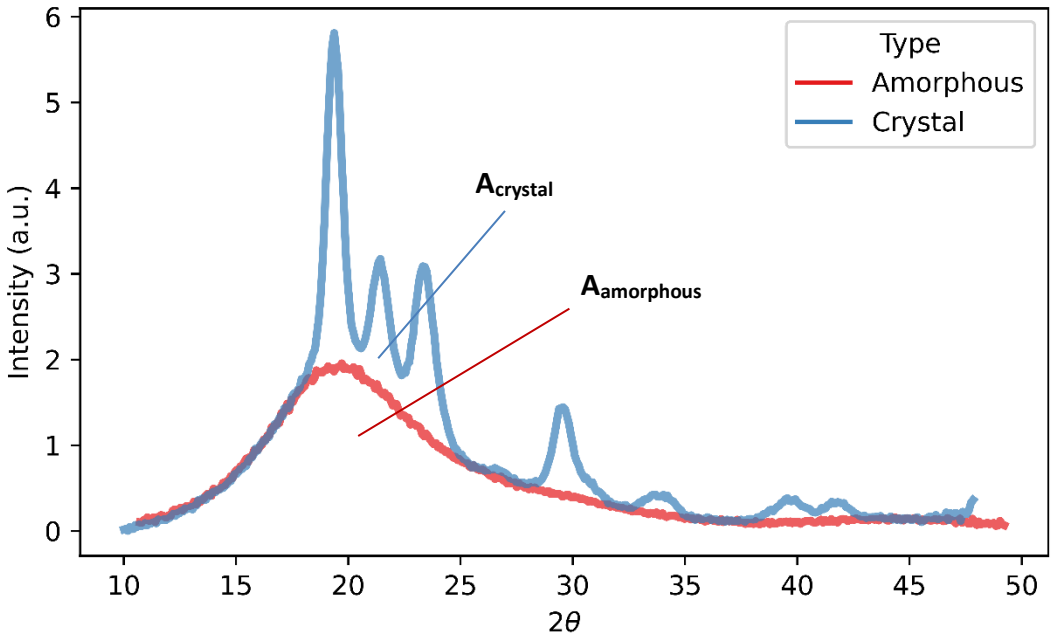

Figure 32. Example WAXS data with amorphous halo.

The **q** value for the major peak observed in the SAXS curves was converted to 2θ using Equation 3, and then the long period (d) was calculated using Bragg's Law:[105]

$$d = \frac{n\lambda}{2\sin\theta} \tag{15}$$

where n is the diffraction order equal to one, λ is the characteristic wavelength of copper at 0.154nm, and θ is the angle of incidence. Using the major peak to determine the long period is appropriate as a rough measure and is particularly useful when the correlation function does not work well. In this case, the correlation function is not useful in the fiber reinforced samples as the carbon fibers affect the result and the function is not accurate.[24] The PEEK film was fit to the correlation function using SasView where the correlation function is the Fourier transform of the Lorentz corrected SAXS data.[49] To perform the Fourier transformation, the data was extrapolated to low and high **q** values. Low **q** values were extrapolated using a Guinier approximation, and

high **q** values were extrapolated using Porod's law.[106] The correlation function was used to extract the long period spacing of the lamellar structure.

The lamellar thickness was obtained by multiplying the degree of crystallinity by the long period.[107] X-ray scattering data is provided in Table 9, showing that the lamellar thickness and degree of crystallinity decrease with an increase in melt temperature, cycle count, and processing in air instead of an inert nitrogen atmosphere. The long period is approximately the same across processing conditions. The observed lamellar thicknesses are consistent with previous results reported for PEEK, where thicknesses ranged from 2-6nm.[11,108,109]

Table 9. PEEK Film X-ray Scattering Data

Melt Temperature (°C)	Environment	Cycles	Degree of Crystallinity (%)	Long Period, Peak (nm)	Long Period, Correlation Function (nm)	Lamellar Thickness (nm)
385	Nitrogen	1	41.9	15.0	10.5	6.27
385	Nitrogen	3	37.6	14.9	11.6	5.59
385	Oxygen	1	37.3	14.7	9.8	5.49
385	Oxygen	1	36.2	14.6	10.3	5.29
385	Oxygen	3	39.0	14.6	10.6	5.70
420	Nitrogen	1	33.1	14.2	9.4	4.69
420	Nitrogen	3	30.8	15.5	12.0	4.77
420	Oxygen	3	30.1	14.1	9.8	4.23
400	Nitrogen	1	39.7	15.2	10.0	6.05
400	Nitrogen	3	36.2	14.1	10.7	5.09
400	Oxygen	1	39.5	14.6	9.9	5.78
400	Oxygen	3	38.5	14.2	11.6	5.45

Table 10 shows data collected for the PEKK prepreg samples. The long period measured in SAXS was approximately the same as the PEEK samples. One noticeable difference is in degree of crystallinity, where the crystallinity was significantly lower in the PEKK prepreg. Additionally, the degree of crystallinity in PEKK changed much less, ranging from 23% to 26%,

in contrast to the PEEK film, which ranged from 30% to 41%. Consequently, the lamellar thickness in PEKK was also lower than in PEEK, and the range of change was smaller.

Table 10. PEKK Prepreg X-ray Scattering Data

Melt Temperature (°C)	Environment	Cycles	Degree of Crystallinity (%)	Long period (nm)	Lamellar Thickness (nm)
375	Nitrogen	1	23.18	14.29	3.31
375	Nitrogen	3	25.45	14.63	3.72
375	Oxygen	1	26.37	15.48	4.08
410	Nitrogen	1	25.98	14.86	3.86
410	Nitrogen	3	25.37	14.86	3.77
410	Oxygen	1	27.07	14.31	3.87
410	Oxygen	3	25.89	14.98	3.88
392.5	Nitrogen	1	26.39	14.29	3.77
392.5	Nitrogen	3	26.07	14.40	3.75
392.5	Oxygen	1	26.71	14.51	3.88
392.5	Oxygen	3	26.09	14.07	3.67

3.4.4 Gaussian Process Regression

Data was split into 80% training data and 20% validation data. For the kernel, the dot-product kernel was cubed and combined with the radial basis function (RBF) and white noise kernel:

$$\Sigma(x_i, x_j) = c * \left[\sigma_0^2 + x_i \bullet x_j\right]^3 + c * \exp\left(-\frac{d(x_i, x_j)^2}{2l^2}\right) + \sigma_e^2 I_n \quad (16)$$

where c is a constant, σ_0^2 is the inhomogeneity of the kernel, $d(x_i,x_j)$ is the Euclidean distance, l is the length scale of the kernel, σ_e^2 is the variance of noise, and I_n is the identity matrix. The length scale l was set to 1, and the default value of unity was used for both σ_0^2 and σ_e^2.

Initially, GPR was performed on the normalized FTIR spectra, but the results were unsatisfactory. To improve the accuracy of GPR, an additional fit was performed on the principal components previously identified. The melt temperature, cycle count, and environment were

input variables, and the principal components were response variables. GPR was performed on the PEEK film and PEKK prepreg separately after outliers were removed. After these modifications, the PEEK film GPR model showed a 59.9% accuracy, while the PEKK prepreg model showed 35.0% accuracy. These low accuracies are attributed to the noise present in FTIR data. Additionally, the dataset was subdivided by environment, and surfaces generated based on GPR fit to see the effect of cycles and melt temperature on the first principal component.

In these surfaces, the principal component on the z-axis represents the amount of variation in the underlying FTIR spectra. The GPR surfaces are shown in Figure 33. In Figure 33(a) for the PEEK film that is processed in nitrogen, PC1 decreases as melt temperature increases with an accuracy of 24%. Figure 33(b), PEEK film in oxygen, displays a ridge starting at one cycle and 385°C melt temperature and diagonally crosses to three cycles and 420°C melt temperature and with an accuracy of 61%. Comparing Figure 33(a) and (b), oxygen induces additional variation particularly across cycles. Figure 33(c) shows PEKK prepreg treated in nitrogen, which remains relatively flat across cycles and melt temperatures with an accuracy of 26%. PEKK prepreg in oxygen as shown in Figure 33(d), which exhibits little change across cycles or melt temperature with an accuracy of 21%. Comparing PEEK film in Figure 33(a) and (b) with PEKK prepreg in (c) and (d), the fibers and lower volume of polymer likely reduce any correlation that can be detected using the combined FTIR, PCA, and GPR.

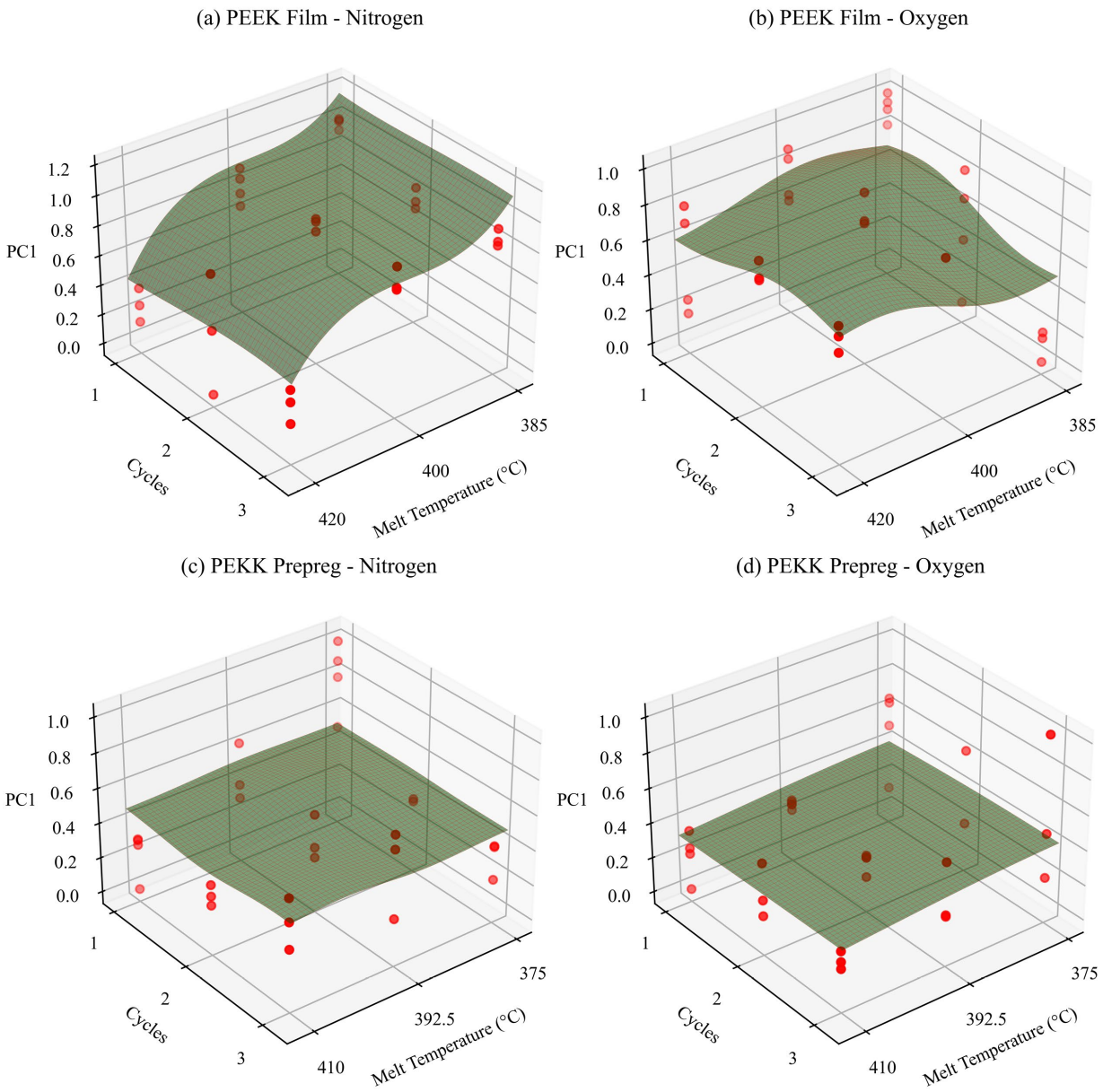

Figure 33. GPR surfaces fit for cycle count, melt temperature, and PC1 (a) shows PEEK film in nitrogen and varies with melt temperature (b) illustrates PEEK film with oxygen and varies in both cycles and melt temperature (c) shows PEKK prepreg in nitrogen and has little variation (d) illustrates PEKK prepreg with oxygen and has little variation.

Next, the x-ray scattering data for PEEK film (Table 9) and PEKK prepreg (Table 10) was analyzed using a similar GPR approach. The resulting GPR curves are displayed in Figure 34,

showing a significant correlation between melt temperature and environment with the resulting lamellar thickness. For PEEK film, an increase in melt temperature results in a rise in the lamellar thickness, whereas processing the sample in air led to a decrease in the lamellar thickness. Melt temperature has the most significant effect, followed by the processing environment (whether it is inert or in air). PEKK prepreg did not have a significant effect with respect to the melt temperature or environment. Cycle count had a minimal effect on lamellar thickness for both materials.

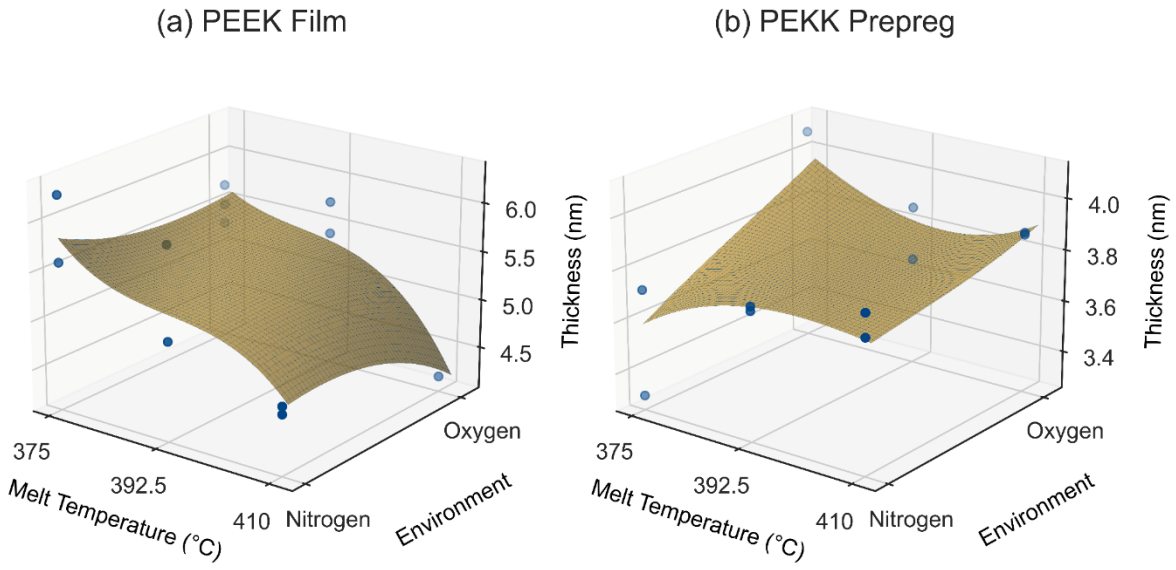

Figure 34. GPR surfaces fit to x-ray scattering data showing melt temperature, environment, and lamellar thickness (a) shows PEEK film (b) shows PEKK prepreg.

Similarly, curves were fit with respect to the long period, and it was found that the long period had no correlation with the processing parameters discussed here. The degree of crystallinity displayed a similar relationship with process parameters as the lamellar thickness.

3.5 Mechanical Testing

The mechanical test data was evaluated using the statistical software JMP to determine the processing parameters that had the largest effect on the resulting mechanical properties.

Parameters in which the p-value was less than 0.05 were considered significant. The significant parameters are presented in Table 11. Significance was estimated using generalized regression using forward selection and validated with the corrected Akaike Information Criterion (AICc).[110] For all materials, the test temperature had a strong effect given that the elevated temperature testing was conducted above the glass transition temperature (T_g) of the thermoplastic materials. For the PEEK film, strain rate and the interaction between strain rate and cycles were significant. This is expected, since strain rate is strongly influenced by viscoelasticity, which becomes dominant above the glass transition temperature. The PEKK prepreg samples did not show a strain rate effect for the range of tested strain rates, potentially due to smaller elongation at break. The PEEK film would stretch about 1000% in the tests above T_g, while The PEKK prepreg samples would fracture around 5% at most. This is a limit of the test fixture and frequency of data sampling of the software. There needs to be enough data points to be confident that the maximum force is recorded. If the strain rate is too fast, then the strength value may not be recorded accurately. As a result, there is a soft limit to the strain rate which was identified to be around $0.002s^{-1}$. This value is well below strain rates that have been identified to illustrate changes in fracture behavior in composites where tests are typically above $1000s^{-1}$.[111,112] The interaction between strain rate and cycles in the PEEK film is likely due to degradation in the polymer. As the PEEK film degrades the polymer chain changes leading to increases in T_g and melt temperature, affecting the viscoelastic response to strain rate changes.

Table 11. Significant Parameters Affecting Mechanical Testing

	PEEK Film	1-Ply PEKK Prepreg	2-Ply PEKK Prepreg
Significant Parameters	Test Temperature Strain Rate Strain Rate * Cycles	Test Temperature	Test Temperature Cycles * Environment

The properties and failure behavior of the PEKK prepreg samples showed differences as the number of plies increased. The 1-ply samples were significantly affected by the test temperature, but not other parameters. This is likely due to the brittle failure response of a single ply composite. In this case, the only correlation was seen when testing was performed above glass transition and compared to room temperature testing. Notably, the difference between low melt temperature and high melt temperature was nearly significant in 1-ply. As the number of plies are increased, due to the slight mismatch of fiber angles between plies, small fiber bridging occurs which affects the failure response of the composite. For example, in the 2-ply samples, the significant parameters included the interaction between cycle repeats and processing environment (i.e., air versus nitrogen). Both cycles and environment are related to degradation in the polymer. The interaction term means that the tensile strength was reduced when the material was processed in air for 3 cycles. In the 2-ply case, cycles and environment were close to significant on their own, further highlighting their impacts on polymer degradation on tensile strength.

The significant parameters were used to fit models using least squares, and the effect of each parameter on tensile strength was determined as shown in Figure 35 for PEEK film. Tensile strength increases with increasing strain rate (shown as displacement rate in Figure 35), while number of cycles only slightly decreases tensile strength. The interaction between strain rate and cycles was not significant and seemed to be dominated by the strain rate effect. An increase in tensile strength with strain rate correlates with the expected viscoelastic response for PEEK. Tensile strength is significantly reduced by testing above the glass transition temperature, and this effect holds for all three materials.

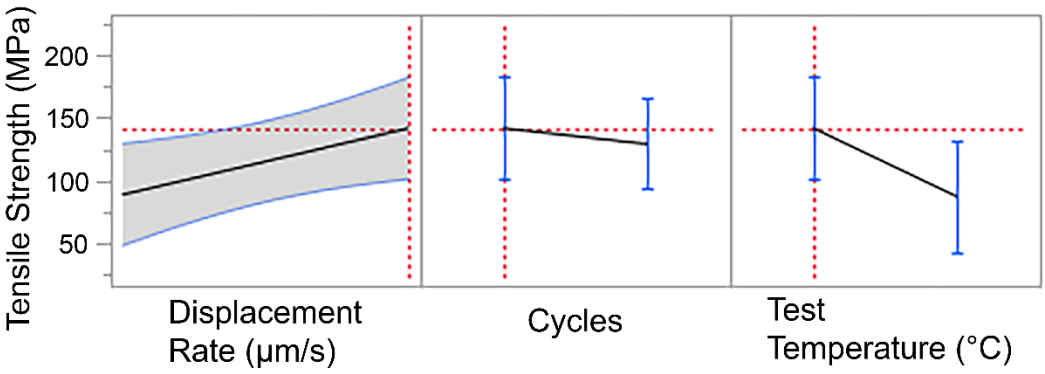

Figure 35. Significant parameter effects on tensile strength for PEEK film.

In Figure 36, 1-ply PEKK prepreg is shown. In this case, only the test temperature was significant, but the melt temperature was close. The melt temperature marginally increased the tensile strength, which may be due to variance since this effect was not seen in the other materials.

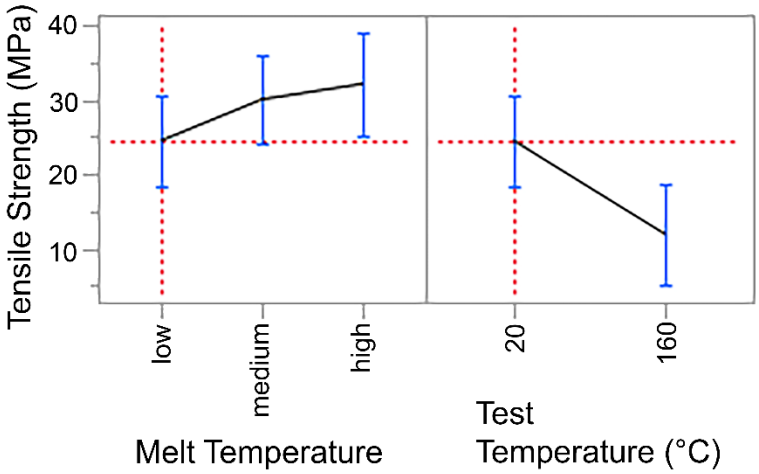

Figure 36. Significant parameter effects on tensile strength for 1-ply PEKK prepreg.

The effect of parameters for the 2-ply PEKK prepreg samples is shown in Figure 37. In this case, the interaction between cycles and environment was substantial, so the effect of each parameter is shown for 1 cycle and 3 cycles. In both situations, tensile strength drops when reprocessing cycles increase from 1 to 3 repeats. At 1 cycle, the environment has a small positive

effect. After 3 cycles, the environment has a large negative impact on the tensile strength. Both cycles and processing in air should increase polymer degradation, and at 2-plies of prepreg the tensile strength is significantly affected by this polymer degradation.

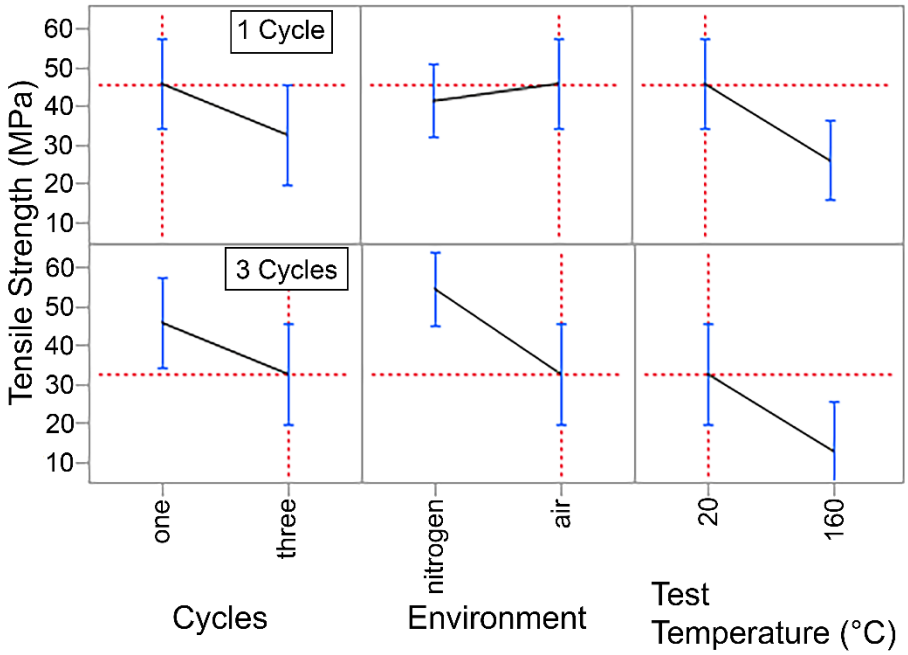

Figure 37. Significant parameter effects on tensile strength for 2-ply PEKK prepreg.

Examples of the failed specimens are shown in Figure 38. A PEKK prepreg failure is shown in Figure 38a., where fibers can be seen bridging between the broken coupon pieces. This fiber bridging after failure was common in the 2-ply samples, whereas the 1-ply samples experienced only brittle failure without fiber bridging. Figure 38b. shows a PEEK film coupon with PEKK prepreg adherends. The film exhibits stretching of the material as well as out-of-plane deformation.

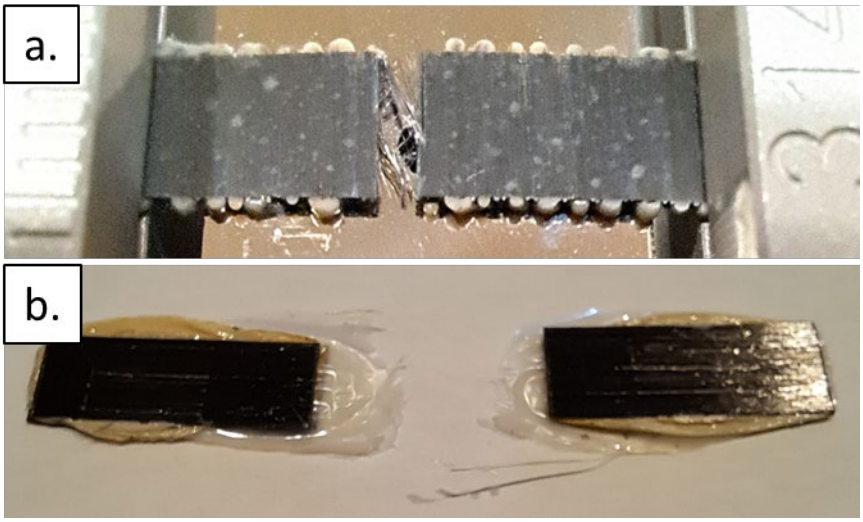

Figure 38. Example failed specimens a. shows PEKK prepreg with fibers bridging the failure b. PEEK film exhibits stretching and out of plane deformation.

An example of failures after tensile testing in PLM is provided in Figure 39. Figure 39(a) shows stretching and alignment of polymer chains that occurred immediately before failure. Figure 39(b) shows a crack that has traveled through the spherulite to the nucleus, changing directions, and continuing out of the spherulite.

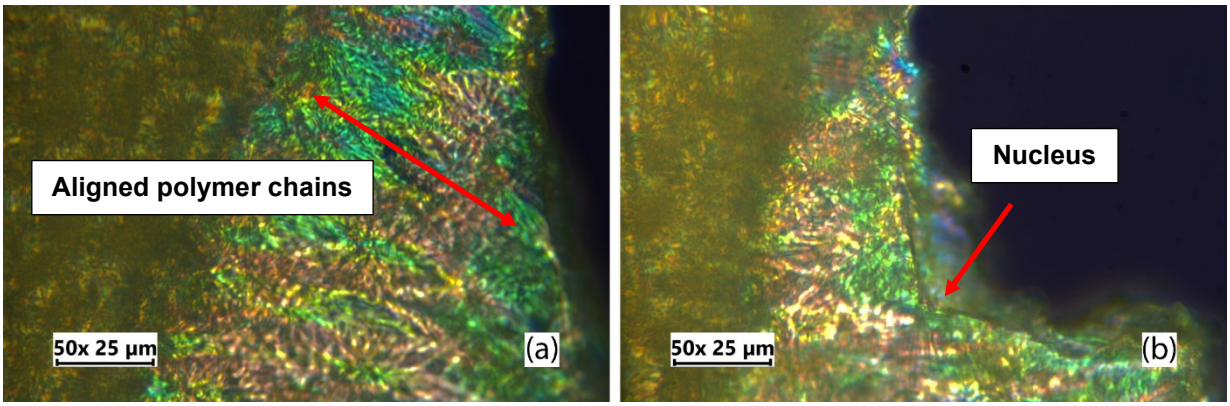

Figure 39. Example fractures in PLM (a) aligning of polymer chains seen near fracture (b) fracture travels to spherulite nucleus.

An example of in-situ PLM is shown in Figure 40. Figure 40(a) shows the crack tip forming at the bottom right of the image. The crack advances in Figure 40(b), with thinning of the material between the crack edges, leading to color changes in PLM. A gap starts to form in Figure 40(c), with final failure shown in Figure 40(d).

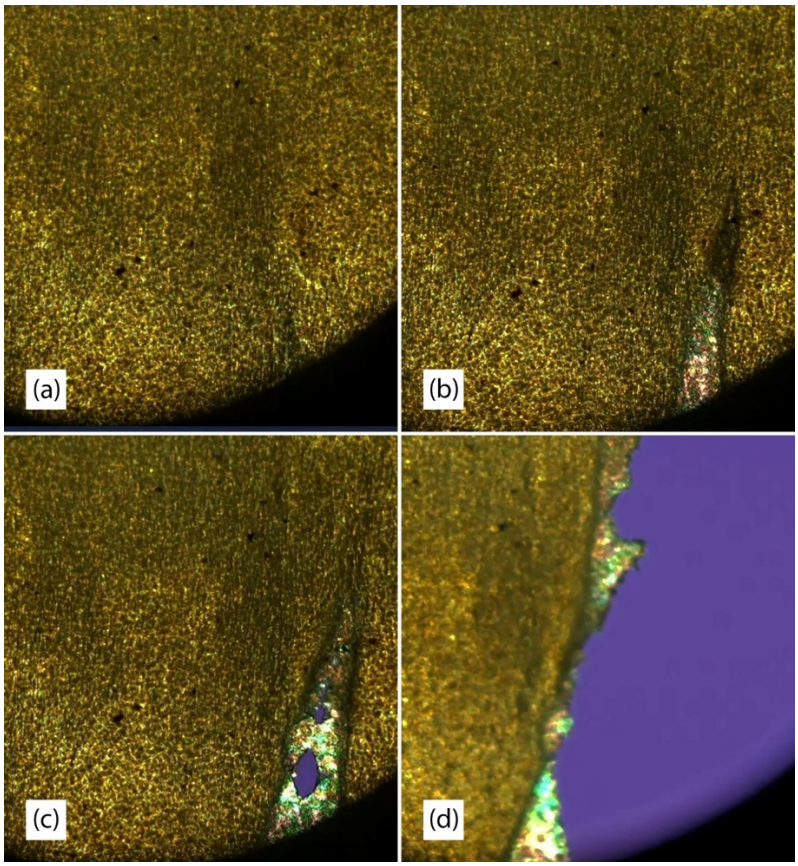

Figure 40. Crack opening before failure. (a) crack tip forms (b) thinning between advancing crack (c) gaps open in crack (d) failure is complete.

A representative set of three samples showing PEEK film and PEKK prepreg in 1 and 2 plies are provided in Figure 41 to illustrate the stress-strain behavior seen across the samples. The stress-strain curves shown are with the same test parameters with “low” degradation, specifically: 1 cycle, 375°C for PEKK and 385°C for PEEK, in nitrogen, tested at room temperature, and 0.1 μm/s displacement rate. Note that the strain values presented in Figure 41

are in log-scale. The 1-ply and 2-ply PEKK prepreg samples had similar stiffnesses with the 1-ply failing around 25MPa and the 2-ply failing at 32MPa. The difference in strength is likely due to greater sensitivity to edge notches in the samples when compared to the 2-ply samples. Both samples exhibited brittle failure. The PEKK prepreg samples failed around 0.8% strain. The PEEK film stretched to about 300% strain before failure at a stress of 43MPa. This value is likely overestimated due to the sample configuration, which had prepreg adherends taped to the PEEK film. The adherends thickness was not used in the stress calculation in this case. Additionally, the width value used to calculate stress in the film does not account for local variations across the sample or local thinning that occurred during the test due to the large amount of stretching. As a comparison, the technical data sheet for Victrex Aptiv film reports 120MPa for tensile strength at room temperature, and Syensqo APC PEKK/CF is reported to be 61MPa for 90° tensile strength.[113,114]

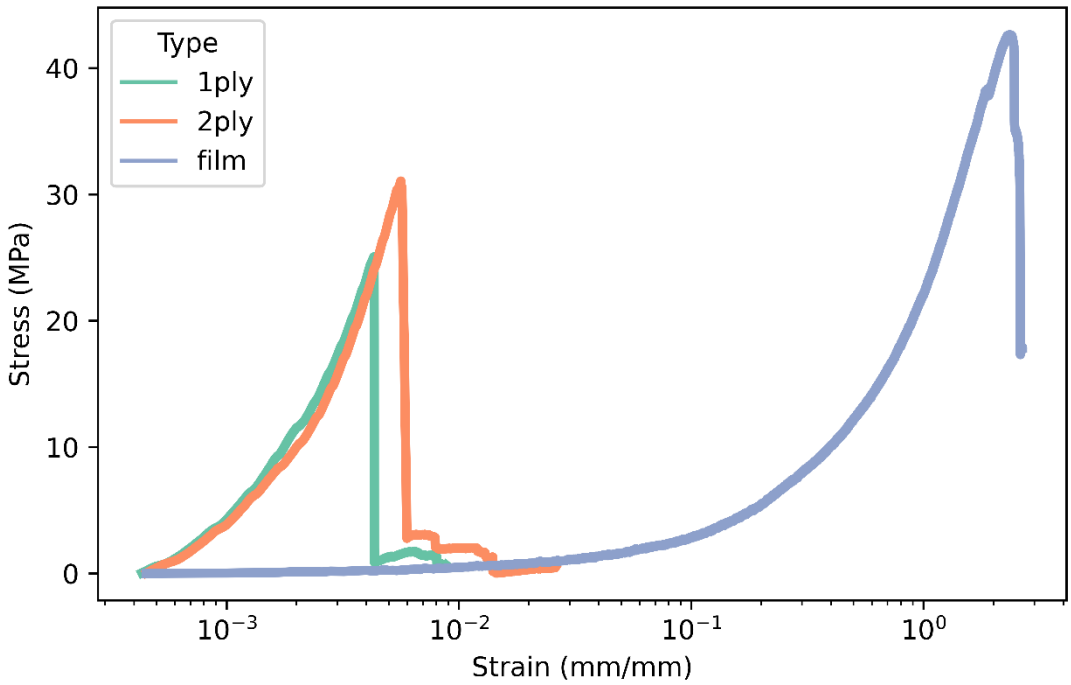

Figure 41. Stress-strain curves of PEEK film and PEKK prepreg with 1 and 2 plies tested at 20°C (strain in log-scale).

3.5.1 Degree of Crystallinity

As the 2-ply tensile coupons showed a correlation with cycle count and environment, they were analyzed using x-ray scattering and DSC to evaluate the spacing between lamellae and their degree of crystallinity, with results presented in Table 12. SAXS yielded findings consistent with previous tests, displaying long period values that remained approximately constant. The degree of crystallinity as measured by WAXS varied between 28% to 37% but did not exhibit a strong correlation with the processing parameters. DSC was also used to determine degree of crystallinity as a confirmation to the WAXS values, revealing a broader range of values from 17% to 49%. Similarly, DSC results showed no clear correlation with the testing parameters.

Table 12. 2-ply Long Period and Degree of Crystallinity

Cycle	Melt (°C)	Environment	Long Period (nm)	%Crystallinity WAXS	%Crystallinity DSC
1	410	Nitrogen	13.3	35.7	20.7
1	375	Nitrogen	13.5	28.2	
3	375	Air	13.3	35.0	49.3
3	392	Nitrogen	13.1	37.5	42.6
1	392	Air	13.3	33.7	26.0
3	410	Nitrogen	13.7	29.6	17.1
1	375	Air	13.2	33.9	25.6

The degree of crystallinity values for the PEEK samples obtained from DSC tests are provided in Table 13. In this case, the crystallinity varied between 11% to 22%. When evaluated using JMP, the processing environment and crystal temperature significantly affected the percent crystallinity. Specifically, exposure to air led to a decrease in the degree of crystallinity, whereas crystallization at 310°C resulted in an increase in crystallinity. Neither melt temperature nor the number of cycles showed a significant effect.

Table 13. PEEK Resin DSC Degree of Crystallinity

Environment	Melt Temperature (°C)	Crystal Temperature (°C)	Cycles	%Crystallinity
Air	385	285	1	11.9
Air	385	310	3	16.0
Air	420	285	3	16.3
Air	420	310	1	17.2
Nitrogen	385	285	3	17.9
Nitrogen	385	310	1	22.0
Nitrogen	420	285	1	18.8
Nitrogen	420	310	3	18.4

The analysis revealed two interactions that affected the percentage of crystallinity, involving the combination of crystallization temperature with melt temperature, and crystallization

temperature with the number of cycles. Specifically, when the crystallization temperature was set at 285°C, undergoing 3 cycles led to an increase in crystallinity, and a melt temperature of 420°C also resulted in increased crystallinity. Conversely, at a crystallization temperature of 310°C, 3 cycles led to a decrease in crystallinity, while a melt temperature of 420°C slightly decreased crystallinity. The parameters influencing percent crystallinity are depicted in Figure 42.

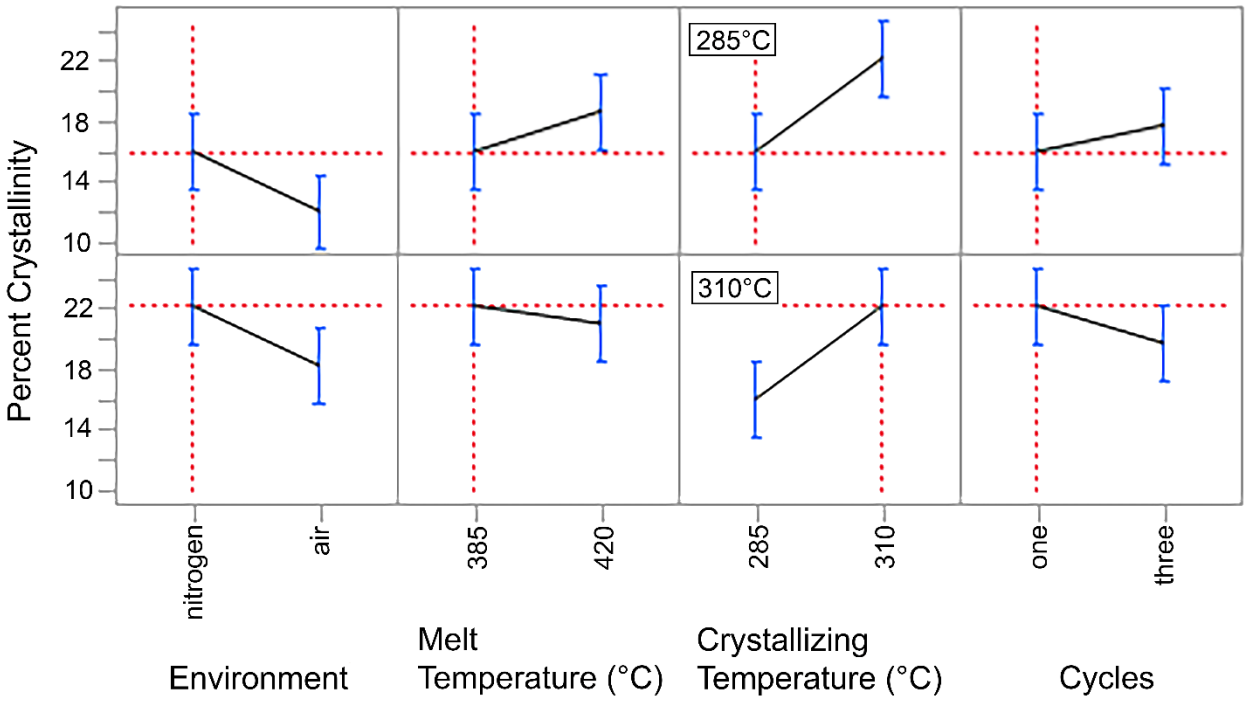

Figure 42. The processing parameters that influence the degree of crystallinity in neat PEEK resin. The top row shows effects at 285°C crystallizing temperature and the bottom row is at 310°C.

3.6 Automated Fiber Placement Application

3.6.1 Wedge peel

Gaussian process regression (GPR) was used to generate surrogate response surfaces and to analyze the effect of process parameters on peel force. In addition, it provides a measure of uncertainty, allowing for estimation of 90% confidence intervals. The radial basis function

(RBF) kernel combined with a white noise kernel was used for training. The mean and 90% confidence intervals for peel force are presented in Figure 43.

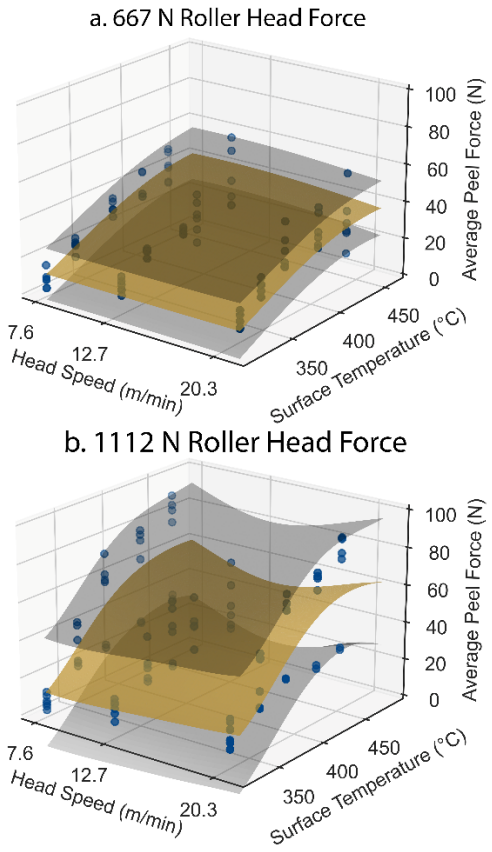

Figure 43. Average peel force response surfaces a. using 667N roller head force b. using 1112N roller head force. The yellow surface is the average result, while the gray surfaces represent the upper and lower bounds of a 90% confidence interval.

Generally, the wedge peel force tends to increase with increasing processing temperature. However, a significantly larger standard deviation was observed at higher temperatures. Additionally, a greater standard deviation for the 1112N compaction force was noted. The average peel force did not show a significant correlation with the selected AFP deposition speeds. One potential factor for this deviation might be fiber nesting, especially due to the parallel fiber orientation between the substrate panel and AFP tows. As the temperature increases

viscosity drops. Consequently, at higher compaction forces there is a likelihood of increased fiber movement including nesting.

At higher variations of peel force, fiber separation was predominantly observed from the substrate, while there was a consistent pattern of fiber buckling and cracking in the AFP tows. Tow cracking seemed to originate at the wedge peel blade. Partial fiber separation is shown for select samples in Figure 44.

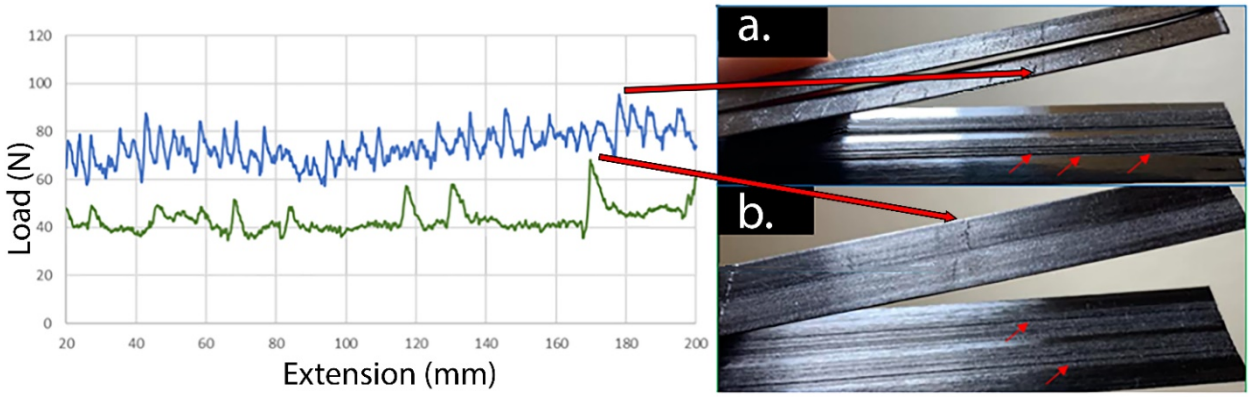

Figure 44. Two examples of variation in sample failure compared to load-extension curves. As fiber pull out and tow cracking are observed during failure, the variation in load increases. a. and b. exhibit partial fiber separation and tow cracking. The large red arrows show tow cracking, and the small arrows show fiber separation.

While fiber separation and higher load variability were more pronounced at higher compaction forces and temperatures, a consistent trend emerged in which the first of three strips within a deposition pass exhibited minimal cracking and fiber separation behavior. This inter-pass variability significantly influenced the observed data spread, as demonstrated in Figure 44, where the peaks in noisy data visually align with sample properties. An example of the inter-pass variability is shown in Figure 45, where changes are shown across six samples from the same pass.

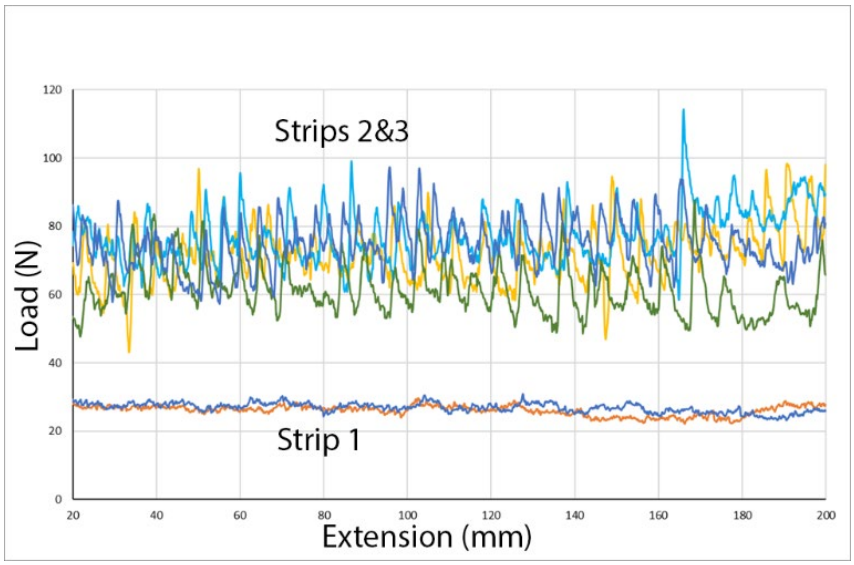

Figure 45. Example wedge peel testing data from a single pass showing all six samples. This is illustrative of the general behavior observed from all testing passes.

One possible source of variation is a temperature gradient across the roller that was noted during real-time FLIR temperature collection, though the behavior of the first strip remained consistent even with rising temperature. The inter-pass load variation was consistent across all panels and roller head speeds and was more pronounced at higher temperatures and compaction forces. The second and third samples in a pass generally had significantly more noise.

Samples with a higher load variation and tow cracking had close contact with the wedge peel blade during testing, potentially due to stronger bonding. Tow cracking likely contributed to the peel force measured from these tests. For samples that exhibited no cracking, a distinct gap was observed in front of the wedge peel blade. This can be seen in Figure 46.

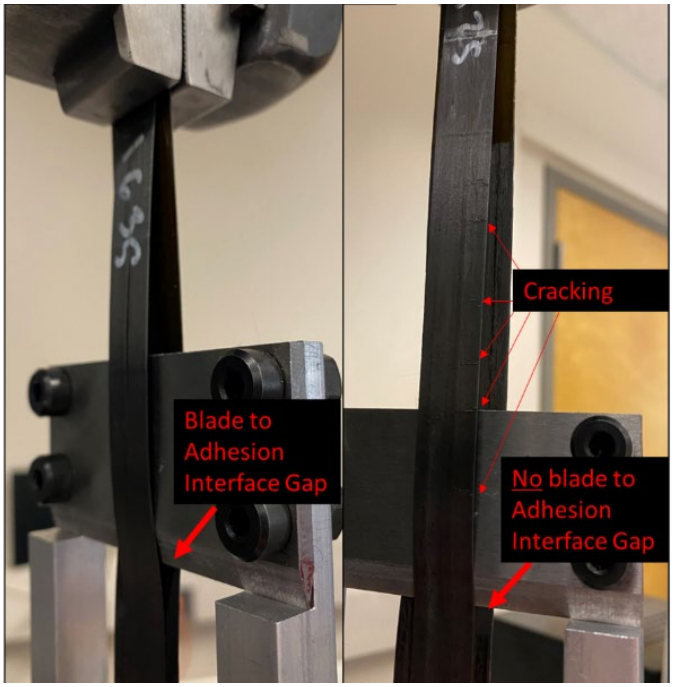

Figure 46. a. Sample with delamination gap ahead of the wedge peel blade. b. Sample with no gap, exhibiting intimate contact with wedge peel blade. Cracking is identified on the sample.

3.6.2 Failure Surface

Two samples were selected from each processing condition, and photographs were taken of their substrate fracture surfaces. The images were processed using trainable Weka segmentation in ImageJ.[115] This process identifies areas of non-bonding (glossy black) and bonding (gray or white). An example of this segmentation is shown in Figure 47, where different roller head speeds are compared at 325°C and 1112N compaction force. In this case, the gray areas are transformed to green post-segmentation. At this temperature and force, the percentage of bonding is highest at 12.7m/min.

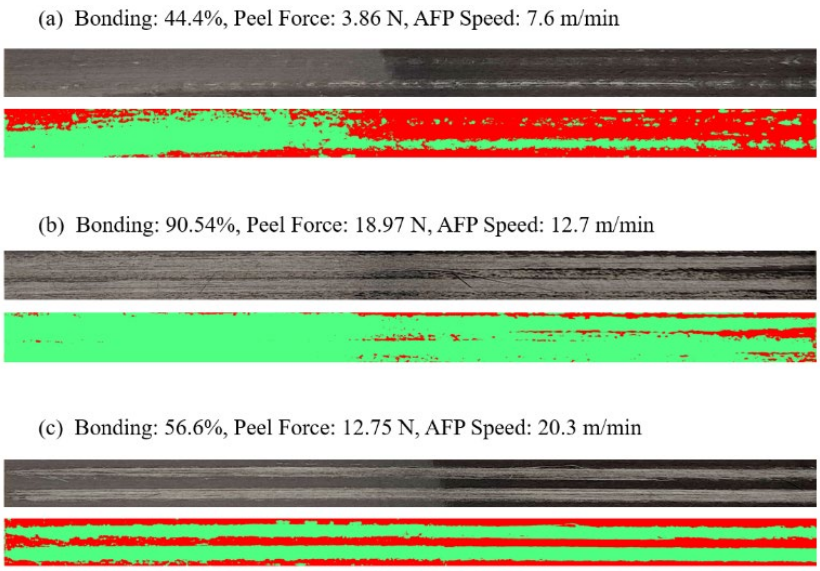

Figure 47. Substrate fracture surfaces compared to Weka Segmentation of bonded and non-bonded areas. Roller head speeds of 7.6, 12.7, and 20.3m/min are compared in this example.

Mean and 90% confidence interval response surfaces were generated for the bonding percentages of fracture surfaces using GPR surrogate modeling. Figure 48a. shows bonding at 667N roller head force, and Figure 48b. at 1112N. Generally, percent bonding increases with processing temperature, mirroring the trend seen in peel force in Figure 43. As temperature rises, viscosity decreases, thereby enhancing both intimate contact and autohesion, which is consistent with the observed increase in bonding. Notably, faster head speed induces a minor reduction in the bonding area. With reduced time, both autohesion and intimate contact decrease, implying that an increase in roller head speed should lead to reduced bonding. Additionally, at lower temperatures and a compaction force of 1112N, the bonding dips at 7.6m/min, peaks at 12.7m/min, and then falls again at 20.3m/min. This distinct parabolic relationship is specific to the percent bonding curve and is not reflected in the force data. As previously noted, the rise in roller head speed should reduce both bonding and force, which explains the dip at 20.3m/min. The reduction at 7.6m/min can be attributed to the fact that LM-PAEK has a melt temperature of

305°C, and the processing occurred around 325°C, where the viscosity remains high. Further, the slower roller head rate may lead to higher viscosity due to shear thinning effects.[116] If viscosity gets excessively high, the degree of intimate contact could be compromised due to increased surface roughness, leading to diminished contact.

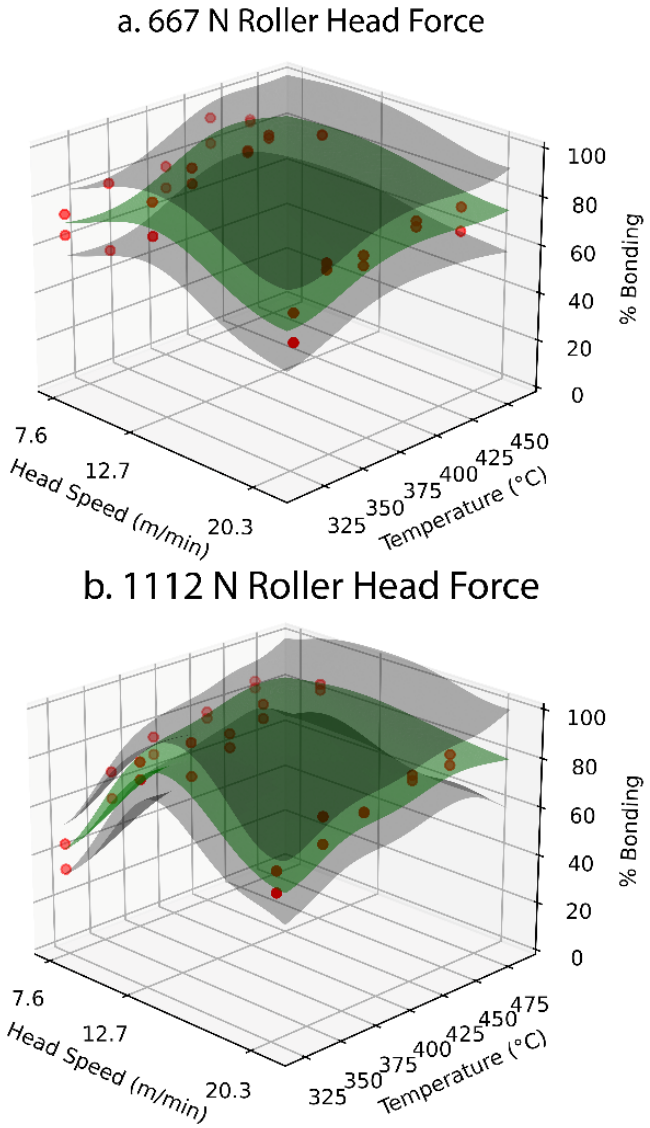

Figure 48. Response surfaces generated for percent bonding of wedge peel failure surfaces. 90% confidence surfaces are shown a. shows 667N compaction force b. 1112N compaction force.

3.6.3 Scanning electron microscopy

The fracture pattern of samples were analyzed using SEM to study the effect of roller head speed, temperature, and compaction force. In addition, the glossy black and gray regions which were used to measure percent bonding were imaged as shown in Figure 49. The micrograph in Figure 49a. shows the area where the sample was bonded exhibiting fiber and resin pull-out as well as exposed fibers. Figure 49b. is flat and uniform with no exposed fibers, suggesting an absence of bonding. This validates the results from image analysis and segmentation based on the gray region of the failed surfaces.

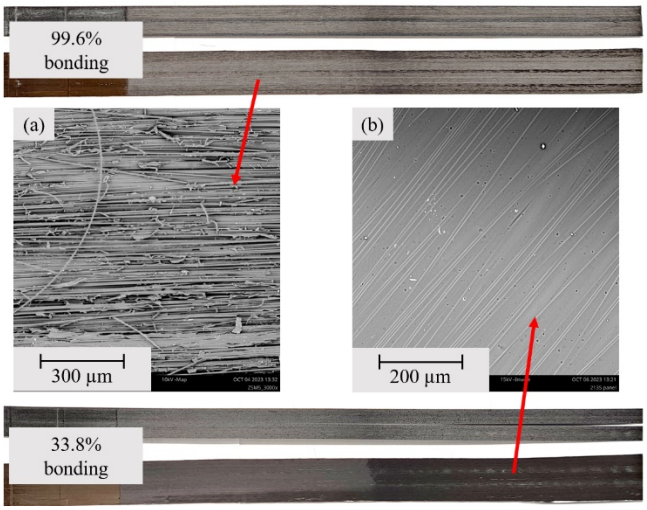

Figure 49. Comparison of bonded area and non-bonded area a. The gray bonded area shows exposed fibers and pulled-out resin and fibers. b. Glossy non-bonded area is flat and undisturbed.

Three samples at low temperature and high roller head force of 1112N were imaged in SEM to better understand the parabolic relationship observed in Figure 48. In these samples, the bonded regions looked similar, with exposed fibers. The main difference was observed in the glossy black regions, where bonding likely did not occur. In this case, the samples with low percent bonding were uniform as previously observed. However, for the sample processed at 12.7m/min, which had a higher bonding percentage, pools of unmelted resin mixed with exposed

fibers were observed. Two roller head speeds are compared in Figure 50 to illustrate the difference. Though segmentation might identify these resin pools as bonded regions, their contribution to the wedge peel force may not be significant.

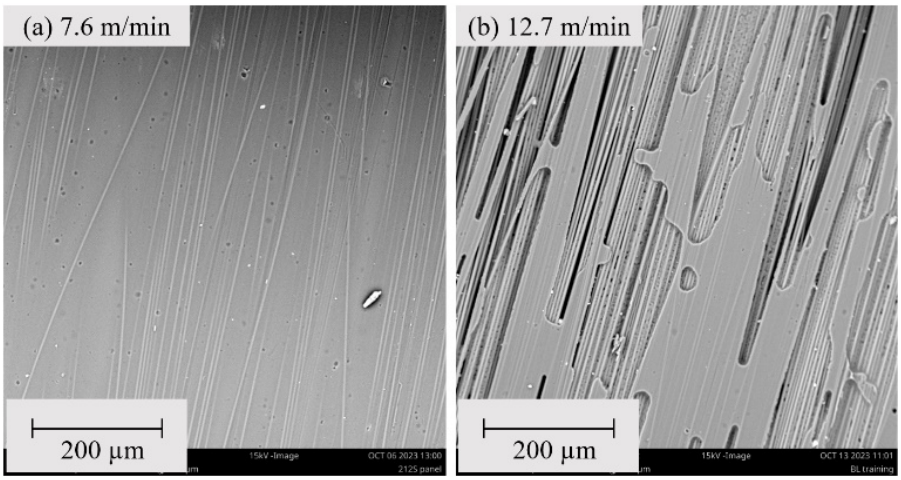

Figure 50. Comparison of 7.6m/min and 12.7m/min roller head speed bonding surfaces a. shows 7.6m/min where the glossy black surface is uniform with some fibers seen near the surface b. 12.7m/min shows exposed fibers along with regions of uniform non-bonded areas.

4 Discussion

4.1 PLM Investigation

The in-situ PLM method enables direct analysis of nucleation, growth, and final crystalline morphology as a function of processing parameters. Additionally, GPR fitting combined with the Lauritzen-Hoffman equation provides insights into the nature of the competing mechanisms during crystallization. The first exponential term in Equation 9 represents diffusion growth as a function of $T_C - T_\infty$, which is similar for both spherulite and transcrystallinity growth. However, the second exponential term represents secondary nucleation as a function of $T_C(T_m^0 - T_C)$, and is different for spherulite and transcrystallinity due to different energy barriers for secondary nucleation as estimated in the previous section. Fitted GPR models were used to calculate and

plot growth rate as a function of temperature in Figure 51 for both spherulites and transcrystallinity regions. This further confirms that compared to spherulites, transcrystallinity has slower growth rates at similar undercooling temperatures.[12,117]

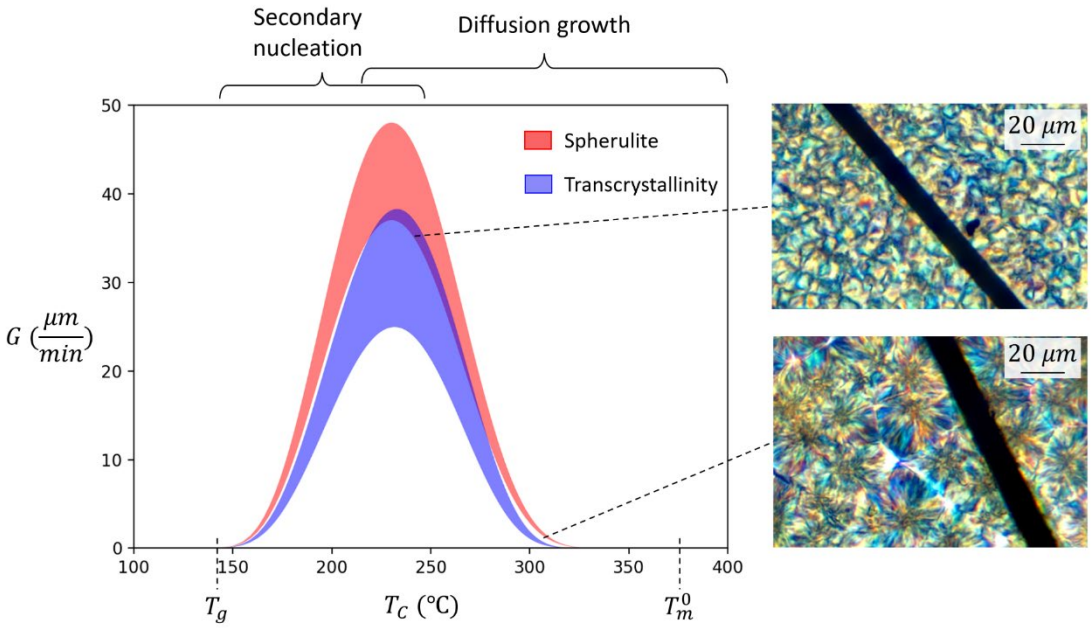

Figure 51. Comparison of growth rate as a function of temperature for spherulitic and transcrystallinity growths. Examples of final morphologies at different temperatures are superposed on the graph.

Another important observation is the bell-shaped curves in Figure 51. While diffusion growth increases closer to T_m, secondary nucleation increases closer to T_g. The combination of these two mechanisms leads to a maximum growth rate somewhere in between the glass transition and melting temperatures, where thermal energy for diffusion is abundant and the drive for secondary nucleation high. In addition, the small undercooling at temperatures close to the melting temperature reduces the quantity of initial nuclei, leading to large spherulites and transcrystallinity regions as demonstrated by PLM results in Figure 23(a) and (b), and also in Figure 51. At temperatures close to the glass transition temperature, small spherulites and

transcrystalline regions are formed with unclear boundaries as shown in Figure 23(c) and Figure 51 due to high drive for initial nucleation but relatively low thermal energy for growth.

With transcrystallinity, a high amount of initial nucleation occurs along the fiber as seen in Figure 2. Most of the transcrystallinity observed in this study was spherulitic in nature, indicating initial nucleation was infrequent along the carbon fiber. The extent of this nucleation can be limited by the growth of neighboring spherulites.[118] Since the transcrystalline region is comprised of the same lamellar structure as spherulites, in theory, its growth rate should follow the Lauritzen-Hoffman equation. In this study, however, nonlinear growth kinetics are observed in GPR fitting (Figure 25), deviating from the Lauritzen-Hoffman equation. Additionally, transcrystalline growth shows correlation to the size of the transcrystalline region (D). Based on Equation 9, size should not affect secondary nucleation. This, however, can be explained based on the competition between spherulite and transcrystallinity growth. As discussed earlier and evident in Figure 51, spherulite growth rate is faster compared to transcrystalline regions. As such, spherulites may hinder the growth of transcrystallinity, depending on their size. This potentially can create nonlinearity in the Lauritzen-Hoffman domain, and hence dependency of growth to the crystal size.

4.2 Segmentation and Classification

The developed ML-based method can be extended to evaluate more complex features in the image data, such as irregular crystal shapes. The determination of eccentricity of these crystal structures may provide insights into the microstructural effects on material properties. Assessing eccentricity should take less effort using YOLOv3 and U-net segmentation, while a similar study done manually would be labor-intensive. This also enables analyzing large amounts of data much faster and in a more consistent manner compared with the manual approach. Additionally,

trained ML models can be used in the future for in-situ microscopy data analysis and process optimization, enabling closed-loop manufacturing.

Note that this study focused on the application of ML method for identifying spherulites and transcrystallinity in PEEK and PEEK composites, but this method can be used to train models on other semi-crystalline thermoplastics with similar growth mechanisms. The use of these methods provides accessibility into complex crystallization kinetics, such as the influence of carbon fiber on the formation of transcrystallinity and spherulites in PEEK. Instead of analyzing micrographs created as snapshots in time, the use of these methods on video encompassing melt to full crystal growth allows for holistic analysis of the entire crystallization process. The models also incorporate all data available in each frame, providing depth to the resulting information not easily available by manual analysis. Lastly, applying these models in real-time allows for studies in which process parameters are changed to assess their effect on crystallization kinetics and therefore material properties of thermoplastic composites.

4.3 Degradation

Crystal growth was observed under the polarizing light microscope, taking only a few seconds for growth to complete at the 385°C and 400°C conditions. However, crystal growth was significantly slowed at 420°C after each thermal cycling. For these same samples, only a marginal amount of change could be detected in the functional groups in FTIR. When processed in x-ray scattering, a significant effect was detected in the degree of crystallinity and lamellar thickness. The long period was found to be approximately the same between samples. Strobl et al. discovered that the distance between lamellae, or the long period, is a function of the crystallization temperature, with increasing crystallizing temperatures allowing for more opportunity for new lamellae to form in between existing lamellae, decreasing the spacing.[119] For

x-ray scattering study, the crystallizing temperature was kept constant at 285°C, so it follows that the spacing is approximately the same between thermal treatments. In addition, the functional groups identified by FTIR had some change indicating cross-linking due to oxidation of the polymer chain, while crystal growth is inhibited as evidenced by PLM and x-ray scattering. The changes in the polymer, even if marginally detected in FTIR, may be sufficient to significantly affect crystal growth rate. In this case, a portion of the polymer is cross-linked and can no longer participate in crystallization. These cross-linked polymers should also reduce the mobility of other polymers, slowing crystal growth. This cross-linking and branching of the polymer chain increases the viscosity of the melt, which further slows crystal growth.[37] Another mechanism of thermal degradation that does not involve cross-linking includes breakdown of the polymer chain into smaller molecular weight chains.[120] Smaller molecules will have less entanglement, which should increase mobility and thus chain folding and crystallization. Another possibility is the presence of self-nuclei, or nuclei that remain after melting. Self-nuclei would make nucleation and growth easier, and would be removed around 400°C and higher.[37] However, at 420°C, no self-nuclei should remain. Some amount of growth slowing can be attributed to the removal of self-nuclei at higher temperatures, but it does not explain the decreasing growth rate with repeated thermal exposures.

The PEKK prepreg yielded modest changes in degree of crystallinity and lamellar thickness with respect to changes in process parameters, especially when compared to the PEEK film. The addition of fibers may protect against the degradation effects seen in the neat PEEK. The fibers provide a large number of heterogeneous nucleation sites. This increased availability of nucleation may overcome thermal and oxidative degradation effects to some extent.

4.4 Mechanical Testing

Neat PEEK resin was influenced by cycles and strain rate during tensile testing. In DSC tests, PEEK samples exhibited significant effects by oxygen in the air, the crystallization temperature, and the interactions between crystallization temperature with both melt temperature and cycles. It is noteworthy that the mechanical testing did not account for crystallization temperature, yet it's probable that tensile strength would be influenced by melt temperature, cycles, and crystallization temperature given the established relationship between crystal formation, mechanical properties, and thermo-oxidative polymer degradation.[8,24,37,121] These findings align with observations from WAXS and FTIR analysis, supporting the conclusion that neat PEEK resin film is susceptible to extended dwells and elevated temperatures that can degrade the polymer matrix and reduce crystallinity. This conclusion also aligned with the literature.[7,32–35,42]

The results from testing 1-ply prepreg samples were inconclusive, showing no significant effects on tensile strength. This may be due to the brittle failure of a single ply with no observed fiber bridging. The tested 1-ply prepreg was imaged in SEM and the chaotic failure is shown in Figure 52. DSC, WAXS, and FTIR all showed no influence from processing parameters.

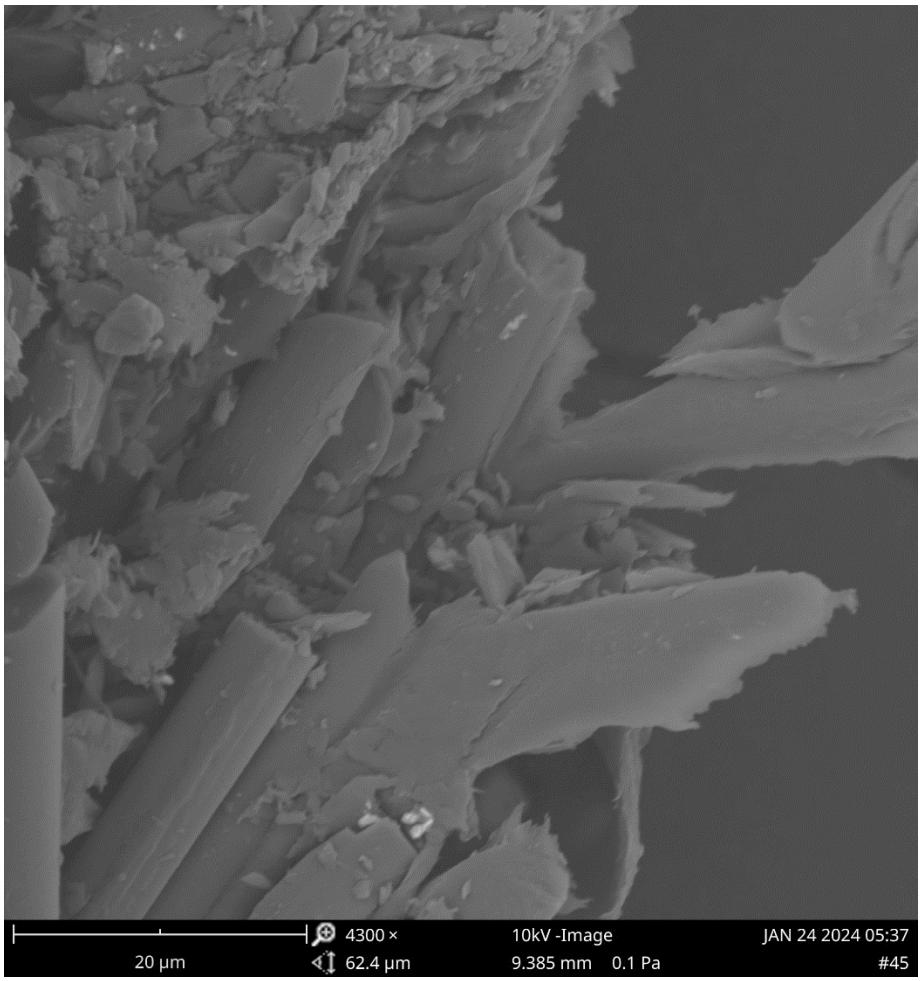

Figure 52. SEM image of 1-ply PEKK prepreg failure.

Samples fabricated with 2-plies were influenced by cycles and oxygen during tensile testing, but this was not reflected in the degree of crystallinity as determined by DSC or WAXS. At these times and temperatures both the 1-ply and 2-ply samples showed no process related influence on crystallinity, but when the number of plies increased to 2-plies the tensile strength was negatively impacted by oxygen in the air and increased melting time. Since the neat resin on its own is established to be affected by thermo-oxidative degradation, the fiber reinforcement may have a protective effect on crystal formation. This is likely due to the sheer amount of heterogeneous nucleation sites provided by the fiber reinforcement. That said, tensile strength of

the 2-ply samples is negatively affected by oxygen and repeated thermal exposure. If the degree of crystallinity is not significantly affected by thermo-oxidative effects, then a reduction in tensile strength is likely due to changes at the interface between the fiber and matrix.

The tested mechanical coupons were examined using SEM. An example of the interfacial failure at the carbon fiber is shown in Figure 53. This shows how the PEKK polymer has stretched away from the carbon fiber and subsequently torn.

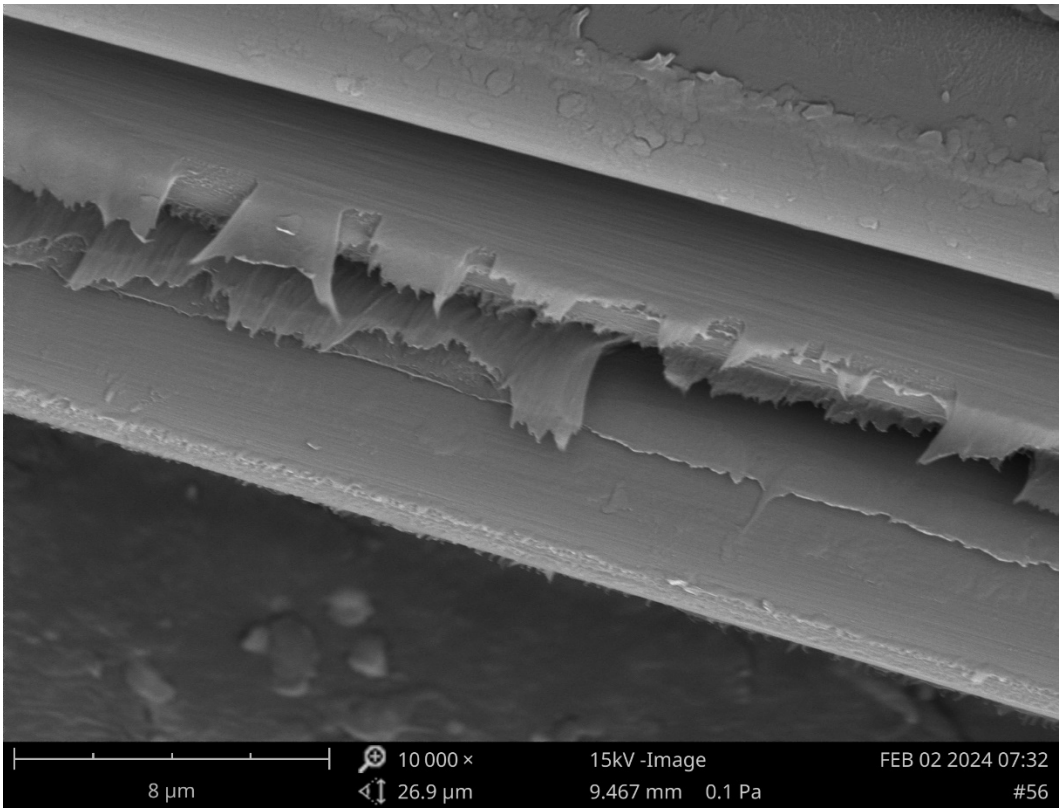

Figure 53. Example of interfacial failure at carbon fiber in SEM.

To assess the differences in fracture surfaces between samples that should have low and high amounts of polymer degradation, samples were imaged using SEM as shown in Figure 54. Figure 54a. is a prepreg coupon melted at 375°C and underwent one cycle, displaying a matrix-dominated failure. Conversely, the failure depicted in Figure 54b, which was processed at 410°C with three cycles, reveals exposed fibers amidst varying amounts of remaining matrix. In this

case, the increase in polymer degradation changed the failure mode from matrix dominated to interfacial failure between the carbon fiber and matrix. Such findings suggest that thermo-oxidative effects could be modifying the interface, thereby changing the failure mode, and leading to reduced tensile strength values despite a comparable degree of crystallinity.

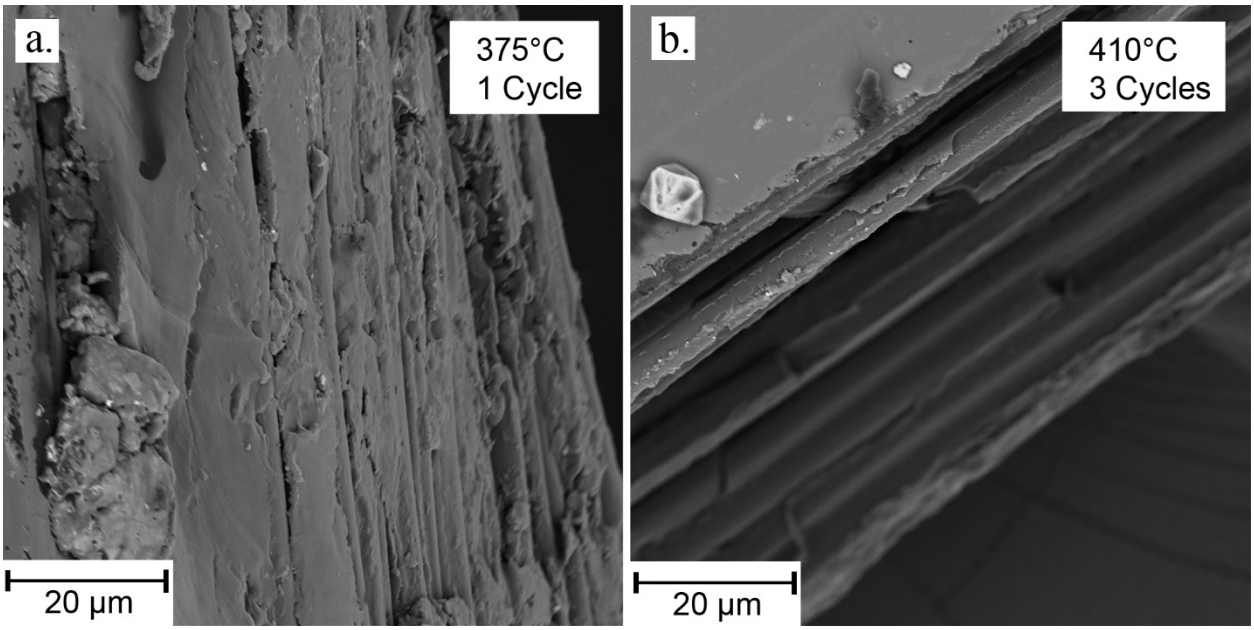

Figure 54. Comparison of fracture surfaces at different amounts of degradation a. shows low degradation where most of the failure occurred within the matrix b. shows high degradation with failure occurring at the interface between fiber and matrix.

4.5 Automated Fiber Placement Application

Bonding during automated fiber placement involves migration of polymer chains during autohesion, as well as the degree of intimate contact. Both mechanisms are influenced by viscosity, which is directly affected by thermo-oxidative degradation. As the polymer chains cross-link, viscosity increases due to decreased mobility. In addition to this, the melting temperature of the polymer increases with increasing degradation, so the thermal processing will change as the polymer continues to degrade.

One objective when fabricating parts using AFP is to create a homogeneous crystalline morphology during cooldown from the melt. If the crystalline structures fail to adequately bridge the interface between plies, a weak point at the interface is created. Therefore, as degradation limits the formation of crystals in the thermoplastic matrix, achieving bridging across the interlaminar layer becomes challenging as polymer degradation advances.

Degree of bonding, as depicted in Figure 48, was defined when fibers were exposed after failure. This exposure is considered a positive event if the crack progresses into the ply rather than advancing through the original interface between the two plies, indicating that the interlaminar layer is monolithic rather than two separate layers. However, exposed fibers might also signify failure at the interface of the fiber, which has been correlated with lower tensile strength properties due to degradation effects.

A high degree of bonding, coupled with lower peel force values at higher temperatures (as seen in Figure 43), could indicate degradation affecting the fiber-to-matrix interface. In this study, this effect was not observed. This indicates that the short processing times even at the higher temperatures may not induce significant degradation at the fiber interface. This approach provides a method for detecting possible issues. Yet, as previously mentioned, the degree of crystallinity may not be enough to detect changes in the mechanical properties of the material.

4.6 GPR Analysis for All Parameters

A Gaussian process regression model was developed using all the parameters and measured characteristics related to degradation. For the PEKK prepreg, as many of the measured quantities were found to be insignificant, a GPR model was not developed. A model was trained for PEEK film using the results from FTIR, WAXS and SAXS, and the process parameters for the mechanical test coupons. These factors were correlated to tensile strength using GPR. Due to the

relatively low amount of data when compared to the number of factors, k-fold cross-validation was used instead of a train-test split, with k-fold set to one.

The kernel was carefully chosen based on the approach given by Duvenaud.[122] Periodic kernels were not used as there is no periodicity in the data. After evaluating the available kernels, adding the radial basis function and the dot product was found to have the best fit to the data:

$$\Sigma(x_i, x_j) = c * \exp\left(-\frac{d(x_i, x_j)^2}{2l^2}\right) + c * \left[\sigma_0^2 + x_i \cdot x_j\right] + \sigma_e^2 I_n \quad (17)$$

where c is a constant, σ_0^2 is a constant controlling the inhomogeneity of the linear kernel, σ_e^2 is the variance of noise, I_n is the identify matrix, l is the length scale, and $d(x_i, x_j)$ is the Euclidean distance. This kernel provided a 99% coefficient of determination. Notably this model is sensitive to the hyperparameters used to fit the data. This is likely due to the relatively low amount of data compared to the number of factors involved. That said, this modelling provides a framework that could be used if additional data was collected.

The successful GPR fit shows that there is a correlation between these factors related to degradation and the subsequent tensile strength of the PEEK film. With further work and additional characterization of the PEKK prepreg, this approach could be used to better understand the mechanisms behind degradation in thermoplastic composites.

5 Conclusions

A combined framework of multifaceted experiments and novel machine learning methods was developed in this study to establish process-microstructure-performance relationships, as well as degradation of semi-crystalline thermoplastics and thermoplastic composites. This included in-situ processing and testing under a PLM, FTIR and X-ray scattering tests, mechanical testing, combined with PCA, CNN and GPR machine learning techniques.

Initially, thin samples were prepared using a compression fixture in a DMA and subsequently processed using a heating and cooling controlled stage under a polarized light microscope. The effect of processing temperature cycle on crystalline type, morphology, and growth rate was studied. The competing effects of secondary nucleation and diffusion for both spherulite and transcrystallinity growth were deconvoluted. It was confirmed that for both spherulites and transcrystallinity, nucleation decreases at temperatures near the melting temperature due to the large thermal energy of the polymer. The use of machine learning methods such as GPR enabled a deeper understanding of crystal kinetics. In this study, PEEK transcrystalline growth with added fibers is shown to have a squared relationship as opposed to the typical linear relationship predicted by Lauritzen-Hoffman theory. Additionally, transcrystalline growth was found to have a small dependence on size, while spherulitic growth had no such dependence.

Crystal nucleation and growth in PEEK and PEEK composite were successfully identified using an improved version of the YOLOv3 algorithm. This allowed for counting and measuring the size of crystals in-situ. The U-net algorithm was used to segment micrograph images of PEEK with and without fiber and successfully separated both spherulites and transcrystallinity. The use of the YOLOv3 and U-net algorithms provides a consistent and fast method to evaluate semi-crystalline microstructure and can help in thermoplastic composite applications where crystallinity is key to load transfer to the fiber and overall composite performance.

PLM showed that nucleation was significantly reduced during repeated cycling, especially at high melting temperatures. This thermal exposure clearly affects subsequent crystal formation, which is likely due to degradation of the polymer matrix. To investigate degradation, a novel PCA-GPR model was developed in this study. This model could successfully identify the effects of degradation on PEEK samples based on FTIR results. However, no significant effect could be

observed for PEKK prepreg. This is most likely due to the presence of carbon fiber in the PEKK prepreg. Comparing the effects of melt temperature, cycle count, and environment showed no obvious clustering, except in the PEEK film when melted at 400°C. The principal components identified by PCA were related to functional groups involved in intramolecular bonding. No functional groups involved in intermolecular bonding or cross-linking were identified. Combined GPR and X-ray scattering showed a decreasing degree of crystallinity and lamellar thickness, but no change in the long period, with increasing thermal exposure. Thermal treatment in air also decreased the degree of crystallinity and lamellar thickness. The PEKK prepreg had less degree of crystallinity and lower lamellar thickness compared with the PEEK film. In addition, the PEKK prepreg did not have a significant change in lamellar thickness or degree of crystallinity with respect to melt temperature, cycling, or environment. The fiber reinforcement in thermoplastic prepreg may limit degradation effects on crystallinity.

The tensile strength of neat PEEK film is influenced by strain rate and the number of cycles. Specifically, the strength increases with strain rate but decreases as the number of cycles increases. For 2-ply PEKK prepreg, the tensile strength is affected by both the number of cycles and the environmental conditions. The strength diminishes as the number of cycles increases. After a single cycle, the strength remains consistent whether in air or nitrogen, but significantly declines after three cycles in air, suggesting that polymer degradation plays a key role in this reduction. The degree of crystallinity in 2-ply prepreg, as determined by DSC or WAXS, shows no significant changes attributed to melt temperature, environmental conditions, or the number of cycles. In contrast, the degree of crystallinity in neat PEEK film is impacted by exposure to air, the temperature at which crystallization occurs, and the interactions between melt temperature and crystallization temperature as well as between the number of cycles and crystallization

temperature. Despite an unchanged degree of crystallinity, polymer degradation is likely occurring at the fiber interface in 2-ply samples, indicating that degradation can occur without affecting crystallinity measurements.

A combination of wedge peel testing, SEM imaging, image segmentation, and probabilistic machine learning methods were used to assess the effect of AFP processing parameters on mechanical performance and peel strength. Average wedge peel force increased with increased processing temperature, while exhibiting greater variability at higher temperatures. Higher compaction force also led to more variation, while roller head speed showed minimal effect for the selected range in this study. Samples with higher variation tended to crack during testing, with fracture surfaces revealing partial fiber pull-out. The first strip in the AFP pass tended to have low variation in wedge peel force, while the second and third strip yielded much larger variations in wedge peel force. This is likely due to the AFP equipment characteristics, such as the thermal gradient across the roller. In a similar pattern to wedge peel force, the degree of bonding increased with increasing temperature. Conversely, bonding decreased with increasing roller head speed, except for samples tested at 325 °C and 1112 N where opposing forces led to a parabolic relationship. Wedge peel failure surfaces were imaged using SEM to confirm the applicability of image segmentation to determine percent bonding.

A GPR framework was successfully applied to the degradation parameters and correlated with tensile strength. With additional data this framework could be used to achieve a deeper understanding of the mechanics behind thermoplastic degradation in composites.

6 Future Work

One of the limitations in this study was the low DMA compression force used to prepare thin samples. The use of a higher tonnage press could yield thinner mechanical coupons in which

crystals could be observed better during mechanical tests. Videos of these tests could be analyzed using Machine Vision to observe how the crystal structures are stretching and how cracks advance prior to failure. The connection to morphology provides key data that would offer a complete understanding of the material failure behavior and therefore a better view into mechanisms like degradation.

The approach described in this study can be applied to other complex topics involved with thermoplastic composites. For example, with a high-speed camera, the effect of strain rate could be better understood, and the mechanical characteristics of the composite above the glass transition could be explored.

GPR was heavily used throughout this study; however, many other useful machine learning techniques could be leveraged. Generally, other machine learning techniques, such as neural networks or random forests, require more data to provide useful insights. A high-throughput system could generate a large volume of data, offering deeper insights into these material systems. For example, a smart microscope system could be developed by combining PLM with a heating stage. In this system, in-situ microstructural information is continuously fed back into a machine learning model that adjusts and optimizes process parameters to achieve the desired end-state. These smart microscopes can assist engineers and scientists in their work with semi-crystalline thermoplastics. A predictive machine learning model can be developed to take a PLM image of the state of crystallization and predict the final morphology and performance of the material. Furthermore, an inverse predictive machine learning model can be developed to take a crystallinity micrograph as input to predict the set of process parameters required to achieve that morphology state. Ideally, these morphology states should also be tied to mechanical properties, allowing properties to be optimized and based on the microstructure.

Additional work could explore other fiber types, such as fiberglass, or fabrics instead of unidirectional fibers. Considerable effort is being dedicated to developing thermoplastic composite methods, such as automated fiber placement and welding; the approach in this study could investigate these processes. Fiber sizing is not currently prevalent for thermoplastics, but there are promising options such as polyetherimide that could be investigated to see if it improves interfacial shear strength.

Another avenue for future work could involve utilizing exotic processing schemes to explore the creation of new crystal types and determine their advantages for composite structures. Analogous to the development of a time-temperature-transformation diagram for steel, a similar diagram could be generated for the various crystals that form in thermoplastic composites.

Acknowledgements

First and foremost, I would like to thank my wife, Lydia. This undertaking would not have been possible without the constant support from my best friend. I don't know if I would have had the confidence to do this on my own. Making the plunge to start school again in the middle of my career was scary, but not so scary when I had a steadfast partner to make it through.

I had my first child, Claire, when I started classes. I don't remember much from my first class, and I almost quit right there due to the lack of sleep and difficulty of learning to be a parent and researcher at the same time. Despite this we had another child, Calvin, a couple of years later and it definitely got harder. But nothing has been more worth doing than to see my daughter and son grow up. I hope our love of math, science, and learning impart to our children – and I'm excited to see where they go.

I have to especially thank my mother, who has been through so much these last few years. Despite that, she comes up regularly to help watch our children. I don't think any of this is possible without her.

I cannot believe I had the honor to work with my wonderful advisor Dr. Navid Zobeiry. The sheer amount I have learned these past four years is remarkable, and I go forth a much stronger scientist and engineer. I am eternally thankful that Professor Zobeiry took a chance on having me as his first PhD student, and I hope to continue to work with Professor Zobeiry throughout the rest of my career.

I will miss the conversations and interactions with my colleagues in the Zobeiry group, who are all such intensely hard working sweet people. Caleb Schoenholz who started after me and will likely finish before me through sheer will and effort. Thanks for all the conversations and sanity checks as we navigated the PhD process, especially when we were alone in the labs during

the pandemic. Pau Portales, thanks for listening to my poor attempts at Spanish and I hope you're killing it in hockey. Amirali Eskandariyun who is so welcoming and easy to talk with. I hope the rest of your PhD experience goes well and I know you will find success. And of course, Max Fu, who was as crazy as me and had a daughter right when he started the PhD journey. I'll miss the pictures of your family and the sheer amount of love you have for your daughter and her growth.

I also want to especially thank Tatyana Berezyuk, who was the MSE lab manager during the pandemic. Most of the days I was working in the lab in 2020 and 2021, it was just me and Tatyana. Without her I would have had so much trouble getting started with everything shut down. Tatyana is also the best lab manager I've ever interacted with, and I wish her infinite success.

I want to thank Dr. Andrew Jimeniz. While I only got to speak with Andrew a couple of times, he was the exact expert I needed to course correct early in my work. The sheer amount of time I likely saved by talking with Andrew only a couple of times is hard to believe. I only wish I had gotten to know him earlier.

Thanks to my committee members Dr. Marco Salviato, Dr. Eleftheria Roumeli, and Dr. Junlan Wang who made the process a lot less scary and provided wonderful advice at each of my exams. Thanks to Dr. Lilo Pozzo for introducing SAXS and her lab members at the Molecular Engineering Materials Center who helped me figure out SAXS including Dr. Fábio Baum, Abdul Moeez, and Lorenzo Guio. Thanks to the handy Alex Gray for making things work in so many of my experiments.

Thanks to the great people at the Washington Clean Energy Testbeds, the Research Training Testbed, and the Department of Chemistry for all the support in all the characterization techniques I needed the last four years.

Thanks to the master's students who I worked with: Shuangshan Li, Kevin Chen, Seth Nichols, Logan Oster, and Griffin Chase.

I would like to acknowledge financial support by the University of Washington and the State of Washington in the USA, as well as in-kind contributions of Toray Industries, Janicki Industries, Henkel AG & Co. KGaA, Victrex plc, and Daher.

I would like to thank Air Force Research Laboratory (AFRL), and Convergent Manufacturing Technologies US for their financial support. Additionally, I extend my appreciation to Toray Advanced Composites for their material donation.

The author acknowledges the use of facilities and instrumentation supported by the U.S. National Science Foundation through the Major Research Instrumentation (MRI) program (DMR-2116265) and the UW Molecular Engineering Materials Center (MEM-C), a Materials Research Science and Engineering Center (DMR-2308979).

This work benefited from the use of the SasView application, originally developed under NSF award DMR-0520547. SasView contains code developed with funding from the European Union's Horizon 2020 research and innovation programme under the SINE2020 project, grant agreement No 654000.

References

1. Denault, J. & Dumouchel, M. Consolidation Process of PEEK/Carbon Composite for Aerospace Applications. *Adv. Perform. Mater.* **5**, 83–96 (1998).
2. Green, S., Ferfecki, F. J. & Marburger, U. Overmoulding of PEEK Compounds for Composites Aerospace Brackets. *S.A.M.P.E. J.* **54**, 22–29 (2018).
3. Denault, J. & Vu-Khanh, T. Crystallization and Fiber/Matrix Interaction During the Molding of PEEK/Carbon Composites. *Polym. Compos.* **13**, 361–371 (1992).
4. Tierney, J. J. & Gillespie, J. W. Crystallization kinetics behavior of PEEK based composites exposed to high heating and cooling rates. *Compos. Part A Appl. Sci. Manuf.* **35**, 547–558 (2004).
5. Lee, A., Wynn, M., Quigley, L., Salviato, M. & Zobeiry, N. Effect of temperature history during additive manufacturing on crystalline morphology of PEEK. *Adv. Ind. Manuf. Eng.* **4**, 100085 (2022).
6. P. Tsotra *et al.* Thermo-Oxidative Degradation of Peek At High Temperatures. in *ECCM18 - 18th European Conference on Composite Materials* 24–28 (2018).
7. Day, M., Sally, D. & Wiles, D. M. Thermal degradation of poly(aryl-ether-ether-ketone): Experimental evaluation of crosslinking reactions. *J. Appl. Polym. Sci.* **40**, 1615–1625 (1990).
8. Pascual, A., Toma, M., Tsotra, P. & Grob, M. C. On the stability of PEEK for short processing cycles at high temperatures and oxygen-containing atmosphere. *Polym. Degrad. Stab.* **165**, 161–169 (2019).
9. Wang, Y., Chen, B., Evans, K. & Ghita, O. Enhanced Ductility of PEEK thin film with self-assembled fibre-like crystals. *Sci. Rep.* **8**, 1–13 (2018).

10. Zhang, L. *et al.* Interfacial crystallization and mechanical property of isotactic polypropylene based single-polymer composites. *Polymer (Guildf).* **90**, 18–25 (2016).

11. Blundell, D. J. & Osborn, B. N. The morphology of poly(aryl-ether-ether-ketone). *Polymer (Guildf).* **24**, 953–958 (1983).

12. Patki, R., Mezghani, K. & Phillips, P. J. Crystallization Kinetics of Polymers. in *Physical Properties of Polymers Handbook* 625–640 (Springer New York, 2007). doi:10.1007/978-0-387-69002-5_39.

13. Hoffman, J. D. & Lauritzen, J. I. Crystallization of bulk polymers with chain folding: theory of growth of lamellar spherulites. *J. Res. Natl. Bur. Stand. Sect. A Phys. Chem.* **65A**, 297 (1961).

14. Vyazovkin, S., Stone, J. & Sbirrazzuoli, N. Hoffman-Lauritzen parameters for non-isothermal crystallization of poly(ethylene terephthalate) and poly(ethylene oxide) melts. *J. Therm. Anal. Calorim.* **80**, 177–180 (2005).

15. Xu, J., Reiter, G. & Alamo, R. G. Concepts of nucleation in polymer crystallization. *Crystals* vol. 11 (2021).

16. Wang, W., Qi, Z. & Jeronimidis, G. Studies on interface structure and crystal texture of poly(ether-ether-ketone)-carbon fibre composite. *J. Mater. Sci.* **26**, 5915–5920 (1991).

17. Karsli, N. G., Demirkol, S. & Yilmaz, T. Thermal aging and reinforcement type effects on the tribological, thermal, thermomechanical, physical and morphological properties of poly(ether ether ketone) composites. *Compos. Part B Eng.* **88**, 253–263 (2016).

18. Bas, C., Battesti, P. & Albérola, N. D. Crystallization and melting behaviors of poly(aryletheretherketone) (PEEK) on origin of double melting peaks. *J. Appl. Polym. Sci.* **53**, 1745–1757 (1994).

19. Seo, J., Zhang, X., Schaake, R. P., Rhoades, A. M. & Colby, R. H. Dual Nakamura model for primary and secondary crystallization applied to nonisothermal crystallization of poly(ether ether ketone). *Polym. Eng. Sci.* 1–11 (2021) doi:10.1002/pen.25767.

20. Gordnian, K. CRYSTALLIZATION AND THERMO-VISCOELASTIC MODELLING OF POLYMER COMPOSITES. (University of British Columbia, 2017).

21. Kong, Y. & Hay, J. N. Multiple melting behaviour of poly(ethylene terephthalate). *Polymer (Guildf).* **44**, 623–633 (2002).

22. Ismail, Y. S., Richardson, M. O. W. & Olley, R. H. Optimizing impact properties of PP composites by control of spherulitic morphology. *J. Appl. Polym. Sci.* **79**, 1704–1715 (2001).

23. Motz, H. Characterization of PEEK and short-fiber PEEK thermoplastic composites. (Delaware University, 1987).

24. Regis, M., Bellare, A., Pascolini, T. & Bracco, P. Characterization of thermally annealed PEEK and CFR-PEEK composites: Structure-properties relationships. *Polym. Degrad. Stab.* **136**, 121–130 (2017).

25. Shen, X., Hu, W. & Russell, T. P. Measuring the Degree of Crystallinity in Semicrystalline Regioregular Poly(3-hexylthiophene). *Macromolecules* **49**, 4501–4509 (2016).

26. Wynn, M. & Zobeiry, N. A Fast Method for Evaluating Effects of Process Parameters on Morphology of Semi-Crystalline Thermoplastic Composites. in *Proceedings of the American Society for Composites—Thirty-Sixth Technical Conference on Composite Materials.* (2021).

27. Hayes, B. S. & Gammon, L. M. *Optical Microscopy of Fiber-Reinforced Composites*.

(ASM International, 2010).

28. Olley, R. H., Bassett, D. C., Blundell, D. J. & Ts, C. Permanganic etching of PEEK. **27**, 344–348 (1986).

29. Wang, Y., Beard, J. D., Evans, K. E. & Ghita, O. Unusual crystalline morphology of Poly Aryl Ether Ketones (PAEKs). *RSC Adv.* **6**, 3198–3209 (2016).

30. Preparation, T. & Microscopy, T. Thin Section Preparation and Transmitted Light Microscopy for Fiber-Reinforced Composites[1]. in *Metallography and Microstructures* 115–135 (ASM International, 2004). doi:10.31399/asm.hb.v09.a0009076.

31. Saville, B. P. Polarized Light: Qualitative Microscopy. in *Applied Polymer Light Microscopy* 111–149 (Springer Netherlands, 1989). doi:10.1007/978-94-011-7474-9_4.

32. Patel, P. *et al.* Investigation of the thermal decomposition and flammability of PEEK and its carbon and glass-fibre composites. *Polym. Degrad. Stab.* **96**, 12–22 (2011).

33. Day, M., Cooney, J. D. & Wiles, D. M. The thermal degradation of poly(aryl—ether—ether—ketone) (PEEK) as monitored by pyrolysis—GC/MS and TG/MS. *J. Anal. Appl. Pyrolysis* **18**, 163–173 (1990).

34. Day, M., Cooney, J. D. & Wiles, D. M. The thermal stability of poly(aryl-ether–ether-ketone) as assessed by thermogravimetry. *J. Appl. Polym. Sci.* **38**, 323–337 (1989).

35. Day, M., Suprunchuk, T., Cooney, J. D. & Wiles, D. M. Thermal degradation of poly(aryl-ether–ether-ketone) (PEEK): A differential scanning calorimetry study. *J. Appl. Polym. Sci.* **36**, 1097–1106 (1988).

36. White, K. L. *et al.* Rheological and thermal behaviors of commercial poly(aryletherketone)s. *Polym. Eng. Sci.* **53**, 651–661 (2013).

37. Jonas, A. & Legras, R. Thermal stability and crystallization of poly(aryl ether ether

ketone). *Polymer (Guildf).* **32**, 2691–2706 (1991).

38. Courvoisier, E., Bicaba, Y. & Colin, X. Multi-scale and multi-technique analysis of the thermal degradation of poly(ether ether ketone). *Polym. Degrad. Stab.* **151**, 65–79 (2018).

39. Cole, K. C. & Casella, I. G. Fourier transform infra-red spectroscopic study of thermal degradation in poly(ether ether ketone)-carbon composites. *Polymer (Guildf).* **34**, 740–745 (1993).

40. Mylläri, V., Ruoko, T.-P., Vuorinen, J. & Lemmetyinen, H. Characterization of thermally aged polyetheretherketone fibres – mechanical, thermal, rheological and chemical property changes. *Polym. Degrad. Stab.* **120**, 419–426 (2015).

41. Phillips, R., Glauser, T. & Månson, J. E. Thermal stability of PEEK/carbon fiber in air and its influence on consolidation. *Polym. Compos.* **18**, 500–508 (1997).

42. Patel, P. *et al.* Mechanism of thermal decomposition of poly(ether ether ketone) (PEEK) from a review of decomposition studies. *Polym. Degrad. Stab.* **95**, 709–718 (2010).

43. Hay, J. N. & Kemmish, D. J. Thermal decomposition of poly(aryl ether ketones). *Polymer (Guildf).* **28**, 2047–2051 (1987).

44. Schultz, J. M. Microstructural aspects of failure in semicrystalline polymers. *Polym. Eng. Sci.* **24**, 770–785 (1984).

45. Chu, J.-N. & Schultz, J. The influence of microstructure on the failure behaviour of PEEK. *J. Mater. Sci.* **24**, 4538–4544 (1989).

46. Selvanarayanan, H. K. Effects of Thermal Degradation on Carbon Reinforced PEEK Composites. (Delft University of Technology, 2017).

47. Kim, J., Lee, W. Il & Tsai, S. W. Modeling of mechanical property degradation by short-term aging at high temperatures. *Compos. Part B Eng.* **33**, 531–543 (2002).

48. Fujihara, K., Huang, Z.-M., Ramakrishna, S. & Hamada, H. Influence of processing conditions on bending property of continuous carbon fiber reinforced PEEK composites. *Compos. Sci. Technol.* **64**, 2525–2534 (2004).

49. Verma, R. K. *et al.* SAXS studies of lamellar level morphological changes during crystallization and melting in PEEK. *Polymer (Guildf).* **37**, 5357–5365 (1996).

50. Michael, S. SAXSutilities: a graphical user interface for processing and analysis of Small-Angle X-ray Scattering data (1.024). (2021) doi:https://doi.org/10.5281/zenodo.5825707.

51. Mehmet-Alkan, A. A. & Hay, J. N. The crystallinity of poly(ether ether ketone). *Polymer (Guildf).* **33**, 3527–3530 (1992).

52. Fratini, A. V., Cross, E. M., Whitaker, R. B. & Adams, W. W. Refinement of the structure of PEEK fibre in an orthorhombic unit cell. *Polymer (Guildf).* **27**, 861–865 (1986).

53. Falzon, B. G. & Pierce, R. S. Thermosetting Composite Materials in Aerostructures. in *Revolutionizing Aircraft Materials and Processes* 57–86 (2020).

54. Dhinakaran, V., Surendar, K. V., Hasunfur Riyaz, M. S. & Ravichandran, M. Review on study of thermosetting and thermoplastic materials in the automated fiber placement process. *Mater. Today Proc.* **27**, 812–815 (2020).

55. Stokes-Griffin, C. M. & Compston, P. Laser-Assisted Tape Placement of Thermoplastic Composites: The Effect of Process Parameters on Bond Strength. in 133–141 (2014). doi:10.1007/978-3-319-01884-3_13.

56. Stokes-Griffin, C. M. & Compston, P. An inverse model for optimisation of laser heat flux distributions in an automated laser tape placement process for carbon-fibre/PEEK. *Compos. Part A Appl. Sci. Manuf.* **88**, 190–197 (2016).

57. Çelik, O., Peeters, D., Dransfeld, C. & Teuwen, J. Intimate contact development during

laser assisted fiber placement: Microstructure and effect of process parameters. *Compos. Part A Appl. Sci. Manuf.* **134**, 105888 (2020).

58. Tierney, J. & Gillespie, J. W. Modeling of In Situ Strength Development for the Thermoplastic Composite Tow Placement Process. *J. Compos. Mater.* **40**, 1487–1506 (2006).

59. Tumkor, S., Turkmen, N., Chassapis, C. & Manoochehri, S. Modeling of heat transfer in thermoplastic composite tape lay-up manufacturing. *Int. Commun. Heat Mass Transf.* **28**, 49–58 (2001).

60. Bastien, L. J. & Gillespie, J. W. A non-isothermal healing model for strength and toughness of fusion bonded joints of amorphous thermoplastics. *Polym. Eng. Sci.* **31**, 1720–1730 (1991).

61. Yang, F. & Pitchumani, R. Healing of Thermoplastic Polymers at an Interface under Nonisothermal Conditions. *Macromolecules* **35**, 3213–3224 (2002).

62. Narnhofer, M., Schledjewski, R., Mitschang, P. & Perko, L. Simulation of the Tape-Laying Process for Thermoplastic Matrix Composites. *Adv. Polym. Technol.* **32**, (2013).

63. Manohar, K. *et al.* Predicting shim gaps in aircraft assembly with machine learning and sparse sensing. *J. Manuf. Syst.* **48**, 87–95 (2018).

64. Sacco, C., Baz Radwan, A., Anderson, A., Harik, R. & Gregory, E. Machine learning in composites manufacturing: A case study of Automated Fiber Placement inspection. *Compos. Struct.* **250**, 112514 (2020).

65. Zobeiry, N., Reiner, J. & Vaziri, R. Theory-guided machine learning for damage characterization of composites. *Compos. Struct.* **246**, 112407 (2020).

66. Reiner, J., Vaziri, R. & Zobeiry, N. Machine learning assisted characterisation and

simulation of compressive damage in composite laminates. *Compos. Struct.* **273**, 114290 (2021).

67. Freed, Y., Salviato, M. & Zobeiry, N. Implementation of a probabilistic machine learning strategy for failure predictions of adhesively bonded joints using cohesive zone modeling. *Int. J. Adhes. Adhes.* **103226**, (2022).

68. Freed, Y., Zobeiry, N. & Salviato, M. Development of aviation industry-oriented methodology for failure predictions of brittle bonded joints using probabilistic machine learning. *Compos. Struct.* **297**, 115979 (2022).

69. Zobeiry, N. & Humfeld, K. D. A physics-informed machine learning approach for solving heat transfer equation in advanced manufacturing and engineering applications. *Eng. Appl. Artif. Intell.* **101**, 104232 (2021).

70. Kim, M. & Zobeiry, N. Machine Learning for Reduced-order Modeling of Composites Processing. in *SAMPE Virtual Conference* vol. accepted (2021).

71. Kautz, E. *et al.* An image-driven machine learning approach to kinetic modeling of a discontinuous precipitation reaction. *Mater. Charact.* **166**, 110379 (2020).

72. Liotti, E. *et al.* Crystal nucleation in metallic alloys using x-ray radiography and machine learning. *Sci. Adv.* **4**, (2018).

73. Rasmussen, C. E. & Williams, C. K. I. *Gaussian Processes for Machine Learning*. (The MIT Press, 2005). doi:10.7551/mitpress/3206.001.0001.

74. Mitchell, T. M. *Machine Learning*. (McGraw-Hill, 1997).

75. Gramacy, R. B. *Surrogates: Gaussian Process modeling, Design, and Optimization*. (Chapman and Hall/CRC, 2020).

76. Murphy, K. P. *Machine Learning: A Probabilistic Perspective*. (The MIT Press, 2012).

77. Puga, J. L., Krzywinski, M. & Altman, N. Bayesian networks. *Nat. Methods* **12**, 799–800 (2015).

78. Noh, H. Y. & Fagert, J. Big data analysis for civil infrastructure sensing. in *Sensor Technologies for Civil Infrastructures* 639–677 (Elsevier, 2022). doi:10.1016/B978-0-08-102706-6.00007-6.

79. Yoon, B.-J. Hidden Markov Models and their Applications in Biological Sequence Analysis. *Curr. Genomics* **10**, 402–415 (2009).

80. Cotter, A., Narasimhan, H. & Gupta, M. On making stochastic classifiers deterministic. in *NIPS'19: Proceedings of the 33rd International Conference on Neural Information Processing Systems* (Curran Associates Inc., 2019). doi:10.5555/3454287.3455266.

81. Gao, Z. *et al.* Image Analysis for In-line Measurement of Multidimensional Size, Shape, and Polymorphic Transformation of l-Glutamic Acid Using Deep Learning-Based Image Segmentation and Classification. *Cryst. Growth Des.* **18**, 4275–4281 (2018).

82. Wu, Y., Lin, M. & Rohani, S. Particle characterization with on-line imaging and neural network image analysis. *Chem. Eng. Res. Des.* **157**, 114–125 (2020).

83. Ahmad, O. S. Quantification of overlapping polygonal-shaped particles based on a new segmentation method of in situ images during crystallization. *J. Electron. Imaging* **21**, 021115 (2012).

84. Mazzia, V., Salvetti, F. & Chiaberge, M. Efficient-CapsNet: capsule network with self-attention routing. *Sci. Rep.* **11**, 14634 (2021).

85. Doersch, C. Tutorial on Variational Autoencoders. (2016) doi:https://doi.org/10.48550/arXiv.1606.05908.

86. Mercaldo, F., Brunese, L., Martinelli, F., Santone, A. & Cesarelli, M. Generative

Adversarial Networks in Retinal Image Classification. *Appl. Sci.* **13**, 10433 (2023).

87. Dosovitskiy, A. *et al.* An Image is Worth 16x16 Words: Transformers for Image Recognition at Scale. (2020).

88. Medeghini, L., Mignardi, S., De Vito, C. & Conte, A. M. Evaluation of a FTIR data pretreatment method for Principal Component Analysis applied to archaeological ceramics. *Microchem. J.* **125**, 224–229 (2016).

89. Witten, I. H., Frank, E., Hall, M. A. & Pal, C. J. *Data Mining: Practical Machine Learning Tools and Techniques*. (Morgan Kaufmann, 2016).

90. Bainbridge, K., Schoenholz, C. & Zobeiry, N. Investigating the aging of release coating in aerospace composites manufacturing. *Undergrad. Res. MSE* **2**, 7–11 (2021).

91. Liu, H. *et al.* Effect of polyetherimide sizing on surface properties of carbon fiber and interfacial strength of carbon fiber/polyetheretherketone composites. *Polym. Compos.* **42**, 931–943 (2021).

92. Wynn, M. & Zobeiry, N. Investigating the Effect of Temperature History on Crystal Morphology of Thermoplastic Composites Using In Situ Polarized Light Microscopy and Probabilistic Machine Learning. *Polymers (Basel).* **15**, 18 (2022).

93. Kumar, S., Anderson, D. P. & Adams, W. W. Crystallization and morphology of poly(aryl-ether-ether-ketone). *Polymer (Guildf).* **27**, 329–336 (1986).

94. Pedregosa, F. *et al.* Scikit-learn: Machine Learning in Python. *JMLR 12* **12**, 2825–2830 (2011).

95. *Neutrons, X-rays and Light: Scattering Methods Applied to Soft Condensed Matter*. (Elsevier B.V., 2002).

96. Glatter, O. Data evaluation in small angle scattering: calculation of the radial electron

density distribution by means of indirect Fourier transformation. *Acta Phys. Austriaca* **47**, 83–102 (1977).

97. Pérez-Martín, H., Mackenzie, P., Baidak, A., Ó Brádaigh, C. M. & Ray, D. Crystallisation behaviour and morphological studies of PEKK and carbon fibre/PEKK composites. *Compos. Part A Appl. Sci. Manuf.* **159**, 106992 (2022).

98. Toray Cetex® TC1225. *Toray Advanced Composites* https://www.toraytac.com/media/3bd72fac-0406-48e4-bfc4-2ffd2398ac0c/fxj5OQ/TAC/Documents/Data_sheets/Thermoplastic/UD tapes, prepregs and laminates/Toray-Cetex-TC1225_PAEK_PDS.pdf (2023).

99. Stokes-Griffin, C. M., Kollmannsberger, A., Compston, P. & Drechsler, K. The effect of processing temperature on wedge peel strength of CF/PA 6 laminates manufactured in a laser tape placement process. *Compos. Part A Appl. Sci. Manuf.* **121**, 84–91 (2019).

100. Seo, J. *et al.* Isothermal crystallization of poly(ether ether ketone) with different molecular weights over a wide temperature range. *Polym. Cryst.* **2**, (2019).

101. Crist, B. & Schultz, J. M. Polymer spherulites: A critical review. *Prog. Polym. Sci.* **56**, 1–63 (2016).

102. Schoenholz, C. *et al.* A MACHINE LEARNING-BASED PORTABLE INSPECTION METHOD FOR EVALUATION OF TOOL SURFACE CONDITION AND RELEASE COATING IN COMPOSITES MANUFACTURING. in *SAMPE Conference Proceedings* (Society for the Advancement of Material and Process Engineering – North America., 2022).

103. LEGENDRE, P. & LEGENDRE, L. Numerical Ecology. *Dev. Environ. Model.* **20**, (1998).

104. Challa, G., Hermans, P. H. & Weidinger, A. On the Determination of the Crystalline Fraction in Isotactic Polystyrene from X-Uay Diffraction. *Die Makromol. Chemie* **56**, 169–178 (1962).

105. Jonas, A., Legras, R., Scherrenberg, R. & Reynaers, H. PEEK Oligomers: A Model for the Polymer Physical Behavior. 2. Structure and Thermal Behavior of Linear Monodisperse Oligomers. *Macromolecules* **26**, 526–538 (1993).

106. Koberstein, J. T. & Stein, R. S. Small-angle x-ray scattering measurements of diffuse phase-boundary thicknesses in segmented polyurethane elastomers. *J. Polym. Sci. Polym. Phys. Ed.* **21**, 2181–2200 (1983).

107. Jimenez, A. M. Controlling Particle Structures in Polymers through Nanocomposite Processing. (Columbia University, 2020). doi:https://doi.org/10.7916/d8-d06y-g312.

108. Blundell, D. J. On the interpretation of multiple melting peaks in poly(ether ether ketone). *Polymer (Guildf).* **28**, 2248–2251 (1987).

109. Cebe, P., Chung, S. Y. & Hong, S.-D. Effect of thermal history on mechanical properties of polyetheretherketone below the glass transition temperature. *J. Appl. Polym. Sci.* **33**, 487–503 (1987).

110. Cavanaugh, J. E. & Neath, A. A. The Akaike information criterion: Background, derivation, properties, application, interpretation, and refinements. *WIREs Comput. Stat.* **11**, (2019).

111. Lee, W. J. *et al.* Interfacially-grafted single-walled carbon nanotube / poly (vinyl alcohol) composite fibers. *Carbon N. Y.* **146**, 162–171 (2019).

112. Tang, Z. *et al.* Temperature- and strain-rate-dependent tensile failure behavior of short-fiber-reinforced PEEK composites. *Compos. Part B Eng.* **250**, 110455 (2023).

113. APTIV™ FILMS 1000. *Victrex* https://www.victrex.com/en/downloads/datasheets/aptiv-films-1000-series.

114. Solvay PEEK Laminates. https://www.matweb.com/search/datasheet.aspx?matguid=d1bf7f21e7b64fa2a311e440b14bc060.

115. Arganda-Carreras, I. *et al.* Trainable Weka Segmentation: a machine learning tool for microscopy pixel classification. *Bioinformatics* **33**, 2424–2426 (2017).

116. Yuan, M., Galloway, J. A., Hoffman, R. J. & Bhatt, S. Influence of molecular weight on rheological, thermal, and mechanical properties of PEEK. *Polym. Eng. Sci.* **51**, 94–102 (2011).

117. Himawan, C., Starov, V. M. & Stapley, A. G. F. Thermodynamic and kinetic aspects of fat crystallization. *Adv. Colloid Interface Sci.* **122**, 3–33 (2006).

118. Varga, J. & Karger-Kocsis, J. The occurence of transcrystallization or row-nucleated cylindritic crystallization as a result of shearing in a glass-fiber-reinforced polypropylene. *Compos. Sci. Technol.* **48**, 191–198 (1993).

119. Strobl, G. R., Schneider, M. J. & Voigt-Martin, I. G. Model of partial crystallization and melting derived from small-angle X-ray scattering and electron microscopic studies on low-density polyethylene. *J. Polym. Sci. Polym. Phys. Ed.* **18**, 1361–1381 (1980).

120. Beyler, C. L. & Hirschler, M. M. Thermal Decomposition of Polymers. in *SFPE Handbook of Fire Protection Engineering 2* 111–131 (2002).

121. Talbott, M. F., Springer, G. S. & Berglund, L. A. The Effects of Crystallinity on the Mechanical Properties of PEEK Polymer and Graphite Fiber Reinforced PEEK. *J. Compos. Mater.* **21**, 1056–1081 (1987).

122. Duvenaud, D. K. Automatic Model Construction with Gaussian Processes. (University of Cambridge, 2014).